



Norwegian University of
Science and Technology

Optimization of Piles Supporting Monopile-Based Offshore Wind Turbines by Improved Foundation Models

Veronika Næss

Master of Science in Mechanical Engineering

Submission date: January 2018

Supervisor: Amir Kaynia, KT

Co-supervisor: Ana M. Page, NGI

Norwegian University of Science and Technology
Department of Structural Engineering

Preface

This thesis constitutes the final work of the five year Master of Science program at The Norwegian University of Science and Technology (NTNU), in the field of in Mechanical Engineering. The work has been performed at the Department of Structural Engineering at the Faculty of Engineering Science and Technology, during the autumn semester of 2017, extending to January 2018.

It is expected that the reader is familiar with structural engineering, especially regarding the finite element method and structural dynamics.

Oslo, January 28, 2018

A handwritten signature in black ink that reads "Veronika Næss". The signature is written in a cursive style with a horizontal line underneath it.

Veronika Næss

Acknowledgements

I would like to express my genuine gratitude towards my supervisor, Prof. Amir M. Kaynia of the Norwegian Geotechnical Institute (NGI) and Norwegian University of Science and Technology (NTNU), for providing me the opportunity to conduct this work as a contribution to an industry project of such a high level of interest to myself.

A special thanks goes to my Co-supervisor, Ana M. Page, as she's been truly helpful with every aspect of this thesis. She has showed an incredible amount of patience, and provided valuable advice and guidance, that has helped me reach a much higher level than I could ever have imagined. Her excitement and enthusiasm in my work has been a fantastic motivation, and I am so very thankful to have had the joy of working with her.

Additionally, I would like to thank Tor Anders Nygaard and Jacobus B. De Vaal at the Institute for Energy Technology (IFE), for their support in using 3DFloat, and general interest and suggestions to my work.

At NGI, I would like to thank the entire staff at the department of Computational Geomechanics, for providing me with a fantastic work environment. I especially want to acknowledge Khoa D. V. Huynh for his dedication and advice regarding the Abaqus modeling for this thesis. As well, Karin Norén-Cosgriff is acknowledged for providing data on site measurements.

My family has been a great motivation throughout my studies at NTNU, and a thanks goes to them for all the cheers and support they have provided over the last five years.

Abstract

With the focus on renewable energy sources over the last decades, offshore wind has become a popular source of energy harvesting. Among the different foundation concepts, the monopile is, by far, the most favourable for offshore wind applications (Page et al. 2018). However, a great extent of literature have indicated that the industry practice on monopile foundation design for offshore wind turbines (OWTs), fails to accurately predict the pile behaviour. Thus, excessive costs by overly conservative geometrical solutions are seen in the industry, and cost reductions in the reliability of the foundation design has been recognized as crucial for a further development.

This thesis presents a study on the optimization potential of monopile OWT foundations, though using a more reliable *macro-element* foundation model, as an alternative to the industry practise of applying *API p - y curves*. Integrated time-domain simulations in 3DFloat has been used to simulate the load- and displacement response of the OWT, and the optimization potential has been assessed based on fatigue estimates. The focus has been on monopile-based OWTs situated at clay-dominated sites.

By an assessment on the fatigue damage at the mudline, the macro-element model obtained an estimated fatigue life of 89.8% longer than the API p - y model. New geometries were suggested for the macro-element model to achieve similar fatigue damage estimates as the API p - y model, for geometry optimization. This resulted in a potential of steel savings on the monopile of 10 - 17%, by thickness reduction alone.

Furthermore, the thesis includes a comparison with the different foundation models to measured data of an OWT installed in the North Sea. This analysis also includes an alternative p - y model, with curves extracted from finite element analyses (FEA). The macro-element model was seen to accurately predict all measured natural frequencies of the support structure, with a maximum deviation of 0.3%. In contrast, the industry practice of applying API p - y curves, under predicted all of the tower-bending frequencies by more than 10%.

The *FEA p - y model* also provided good estimates on the measured natural frequencies. A fatigue damage assessment comparing the results from the macro-element model to the FEA p - y model was conducted to investigate the effect of soil damping on the fatigue estimates. A longer life expectancy of 29% was obtained for the macro-element model, and it was realized that neglecting soil damping (as the p - y models do), may limit the

optimization potential of the monopile design.

It was concluded that, by use of the macro-element model in foundation design and optimization, large potentials for cost reductions in the industry may be achieved. This was recognized both with regards to potential material savings, as the model predicted significantly less fatigue damage, as well as costs savings due to the greater reliability of the predictions, and consequently lowering risks.

Sammendrag

Med det økende fokuset på fornybar energi over de siste tiår, har offshore vind vokst til å bli en aktuell energikilde. Blant de forskjellige fundamenttypene, domineres industrien av monopelen. Studier har imidlertid vist at dagens praksis for designanalyser av monopelen til bruk i offshore vind mislykkes i å gi gode estimater på responsen av pelen og jorden omkring den. Dette resulterer i store kostnader grunnet overdimensjonerte geometrier. En reduksjon av kostnadene er forstått som avgjørende for den videre utviklingen av havvindsindustrien.

Denne masteroppgaven presenterer et studie på optimaliseringspotensialet til monopelfundament for offshore vindturbiner, ved å ta i bruk en mer pålitelig makro-element modell som et alternativ til API p – y kurver, som er mye brukt i industrien i dag. Integrerte simuleringer i tids-domenet har blitt utført ved bruk av 3Dfloat for å simulere responsen til konstruksjonen, og optimaliseringspotensialet har blitt vurdert ved utmattingsanalyser. Fokuset har vært på offshore vindturbiner plassert hovedsakelig på leiredominert grunn.

Fra utmattingsanalysene ble det observert at den estimerte levetiden til konstruksjonen økte med 89.8% ved å ta i bruk makro-element modellen, sammenlignet med API p – y modellen. I tillegg viste undersøkelser at ved å vurdere nye geometrier foreligger det et potensiale for redusert materialforbruk i monopelen, estimert til 10 – 17%, kun ved å redusere tykkelsen.

Videre, ble fundamentmodellene tatt i bruk på en eksisterende offshore vindturbin i Nord-sjøen, og sammenlignet med måledata fra turbinen. Analysen indikerte at makro-element modellen estimerte egenfrekvensene til konstruksjonen med betydelig større presisjon enn de andre modellene, med et avvik på kun 0.3%. API p – y modellen på sin side, underestimerte alle målte egenfrekvenser til konstruksjonen med over 10%.

En alternativ p – y modell (FEA p -y modell), basert på p – y kurver generert ved elementanalyser, viste også å estimere de målte egenfrekvensene til konstruksjonen med nøyaktighet. En utmattelsesanalyse som sammenlignet resultatene fra makro-element modellen med resultatene fra FEA p – y modellen ble utført for å vurdere viktigheten av å inkludere dempingen fra jorden rundt, i modellformuleringen. Denne analysen resulterte i 29% lenger levetid for makro-element modellen (som inkluderer demping fra fundamentet), sammenlignet med FEA p – y modellen (som antar ingen demping fra fundamentet). Dette illustrerte nødvendigheten av å inkludere dempingen fra den omkringliggende jor-

den, for å kunne utnytte optimaliseringspotensialet.

Det ble konkludert at å bruke makro-element modellen i design av monopel-fundament til offshore vindturbiner vil medføre et betydelig optimaliseringspotensiale. Herunder en kostnadseffektivisering på grunn av muligheten for redusert materialbruk som følge av lavere utmattelsesestimater, samt mer pålitelige estimater og dermed mindre risiko.

Contents

1	Introduction	1
1.1	Background and Motivation	1
1.2	Foundation Concepts	2
1.3	General Terminology	3
1.4	Previous Research	4
1.5	Objectives	6
1.6	Thesis Outline	7
1.7	Software Used	7
2	Ocean Environment	9
2.1	Wind Modeling	11
2.1.1	Wind Characteristics	11
2.1.2	Wind Representation	12
2.1.3	Turbulence	13
2.1.4	Wind Spectrum	14
2.2	Wave Modeling	15
2.2.1	Wave Theories	15
2.2.2	Wave Representation	19
2.2.3	Wave Loads on Structures	19
3	Fatigue	21
3.1	Definition and Concepts	21
3.2	Stress History and Filtering	22
3.2.1	Obtaining the Stress Time History	22

3.2.2	Counting Methods	23
3.3	S - N Curve	25
3.4	Palmgren-Miner Sum	25
4	Foundation Stiffness and Damping	27
4.1	Natural Frequency	27
4.2	Damping	29
4.2.1	Procedure of Damping Estimation	30
5	Soil - Structure Interaction	33
5.1	Soil Mechanics	33
5.1.1	Behaviour	33
5.1.2	Strength	33
5.2	Soil - Structure Interaction Models	34
5.2.1	p – y Curves	35
5.2.2	Macro-Element Model	38
6	Finite Element Modeling	45
6.1	Coordinate System	45
6.2	Initial Modeling	46
6.2.1	Pile Modeling	46
6.2.2	Soil Modeling	49
6.3	Final Modeling	51
6.3.1	Geometry	51
6.3.2	Interface Properties	52
6.3.3	Shell properties	53
6.3.4	Loads	54
6.3.5	Boundary conditions	54
6.3.6	Mesh	54
6.4	Verification of the FE Model	58
7	Introduction to 3DFloat	61

7.1	Structural Model	61
7.2	Loads	63
7.2.1	Hydrodynamic Loads	63
7.2.2	Aerodynamic Loads	63
7.3	Control System	64
7.4	Running Simulation	64
7.5	Post Processing Tools	65
8	Fatigue Analysis and Optimization Assessment	67
8.1	Method	67
8.2	Model Description	69
8.2.1	The API p - y model	69
8.2.2	The macro-element model	69
8.3	Turbine Properties	71
8.4	Soil Profile	71
8.5	Environmental Conditions	71
8.6	Assumptions and Simplifications	73
8.7	Results and Discussion	74
8.7.1	Model Inspections	74
8.7.2	Natural Frequency and Damping	78
8.7.3	Mudline Moments and Load Excitation	80
8.7.4	Fatigue Assessment	84
8.7.5	ULS Assessment	92
8.7.6	Calibration Sensitivity	93
8.8	Summary	94
9	Real Site Analysis	97
9.1	Method	97
9.2	Model Description	98
9.3	Assumptions and Simplifications	99
9.4	Results and Discussion	99

9.4.1	Comparison Between Simulations and Measurements	99
9.4.2	Fatigue Assessment	103
9.5	Summary	110
10	Conclusion	111
10.1	Conclusion	111
10.2	Suggestions for Further Work	113
A	3DFloat Input File	119
B	TurbSim Input File	135
C	MATLAB Script for Calculating Fatigue Damage	137
D	S - N Data for Steel with Cathodic Protection in Seawater	141
E	Natural Frequencies for the Blade Modes of the OWT in the North Sea	143

List of Tables

5.1	API p – y data for short-term static loading of piles in clay.	36
6.1	Pile properties for the initial geometry.	46
6.2	Soil parameters.	50
6.3	Pile properties for the three geometries.	52
6.4	Shell element properties.	54
6.5	Finite element mesh.	56
8.1	Pile properties.	68
8.2	Some properties of the NREL 5 MW wind turbine	71
8.3	Soil parameters for the API p - y formulation.	71
8.4	Environmental load cases.	72
8.5	Environmental parameters for the 50 year extreme events.	72
8.6	1 st simulated tower-bending natural frequencies frequencies.	79
8.7	Expected fatigue life for the initial geometry.	86
8.8	Expected fatigue life for the different geometries.	91
8.9	Possible steel savings of the monopile.	91
8.10	ULS loads.	92
8.11	Expected Fatigue life for the different calibrations of the macro-element.	93
9.1	Comparison between the measured and the simulated natural frequencies for the first two tower modes.	101
9.2	Measured vs. simulated tower-bending frequencies.	101
9.3	Expected fatigue life.	109

E.1 Comparison between the measured and the simulated natural frequencies
for the first blade modes 143

List of Figures

1.1	Common foundation types for bottom-mounted OWTs.	2
1.2	General terminology used in this study for a monopile OWT.	3
1.3	Coordinate system used throughout this thesis.	4
2.1	Environmental impacts on an offshore wind turbine.	9
2.2	Conversion between frequency- and time-domain by Fourier transform. . .	10
2.3	Horizontal wind-speed spectrum.	12
2.4	True wind profile.	14
2.5	Wave description.	15
2.6	Ranges of validity for various wave theories.	16
2.7	Example of components for Stokes 5 th order wave theory.	18
2.8	Stretching and extrapolation of velocity profile.	18
3.1	Example of a fatigue cycle in pure tension.	22
3.2	Flowchart for calculating fatigue damage using S-N curves and Palmgren-Miner sum.	22
3.3	Moment on a cylindrical cross-section.	23
3.4	Illustration of the Rainflow counting method.	24
4.1	Typical frequency spectra of environmental and mechanical loading on a three-bladed OWT.	28
4.2	Example of a hysteretic loop	30
4.3	Damping estimation through logarithmic.	31
5.1	Mohr-Coulomb yield criteria.	34

5.2	Illustration of a set of distributed springs along a pile, with corresponding $p - y$ curves.	35
5.3	Shape of a typical API $p - y$ curve for laterally loaded piles in clay.	36
5.4	Stress around a laterally loaded pile.	37
5.5	$p - y$ path vs kinematic hardening path.	38
5.6	Illustration of a yield surface including vectors of plastic flow.	39
5.7	Illustration of different hardening laws.	41
5.8	Yield surfaces used by the macro-element.	42
5.9	Illustration of the behaviour of the macro-element.	43
6.1	Coordinate system for the Abaqus model.	46
6.2	Analytical solution vs. FE model using shell elements.	47
6.3	Symmetry boundary conditions.	48
6.4	Response comparison of symmetric and full model.	48
6.5	Soil profile of the idealized clay model.	49
6.6	Comparison of the lateral displacement and the bending moment due to different sizes of soil volume.	51
6.7	Visualization of the contact formulation used.	53
6.8	Comparison of the lateral displacement and the bending moment for different mesh element sizes.	56
6.9	Global mesh of the Abaqus model.	57
6.10	Deformation of the soil.	58
6.11	Comparison of Abaqus and PLAXIS results.	59
6.12	Moment - displacement curves at pile head.	59
7.1	Element coordinate system in 3DFloat.	62
7.2	Global coordinate system definition in 3DFloat	62
7.3	Illustration of TurbSim wind field	64
8.1	Illustrations of the two models.	70
8.2	S - N curve F3 for steel in seawater with cathodic protection.	73
8.3	Wind speeds for load case 6.	75
8.4	Wave elevation for load case 6.	75

8.5	JONSWAP spectrum for load case 6.	76
8.6	Rotor speeds for various LCs.	76
8.7	Paraview plots in the xz-plane.	77
8.8	Paraview plot of the OWT.	77
8.9	Tower top displacements from free vibration test with initial displacement of 0.2m.	78
8.10	Visualizations of the 1 st tower-bending natural frequencies	79
8.11	Load - displacement curve at the mudline	80
8.12	Mudline fore-aft bending moments.	81
8.13	PSDs of the mudline fore-aft bending moments.	82
8.14	JONSWAP spectrum of load case 6, the fundamental frequency of the two models.	83
8.15	Campbell diagram.	84
8.16	Positions on the cross-section investigated for fatigue damage.	85
8.17	Mudline moments at different positions on the pile cross-section.	85
8.18	Normalized fatigue damage at the mudline for the initial geometry.	86
8.19	Maximum obtained moments at the mudline.	87
8.20	Mudline moments of load cases 5 and 12 for the API p - y model.	88
8.21	Comparison of the pile response from Abaqus model to the two p - y formulations.	89
8.22	Normalized fatigue damage below the mudline.	90
8.23	Normalized fatigue damage at the mudline for the different geometries.	91
8.24	Stress along pile under ULS loads.	93
8.25	Normalized fatigue damage at the mudline for the different calibrations of the macro-element.	94
9.1	Comparison of the results from FEA to the two p - y formulations.	98
9.2	Moment - displacement curve at the mudline.	100
9.3	PSD of the measured accelerations at site versus simulated natural frequencies from the macro-element model.	100
9.4	PSD of the measured accelerations in the fore-aft direction, and the corresponding fundamental frequencies of the three models.	102

9.5	Simulated mudline moments.	103
9.6	Captions of environmental spectra for load case 15.	104
9.7	PSD of the mudline fore-aft bending moments.	105
9.8	Mudline moments from free vibration test.	106
9.9	Mudline moments and displacements.	106
9.10	Damping ratios for various moment amplitudes at the mudline.	107
9.11	Normalized fatigue damage at the mudline.	108
9.12	Deviation from the obtained fatigue damage for the FEA p - y model to the macro-element model.	109
D.1	S - N data for steel with cathodic protection in seawater	141

Nomenclature

Acronyms

ABL	Atmospheric Boundary Layer
API	American Petroleum Institute
BC	Boundary Condition
BEM	Blade-Element/Momentum
BLF	Buckling Load Factor
CAE	Computer Aided Engineering
DFF	Design Fatigue Factor
DFT	Discrete Fourier Transform
DLC	Design Load Case
dll	Dynamic-Link-Library
DNV	Det Norske Veritas
DOF	Degree Of Freedom
FE	Finite Element
FEA	Finite Element Analyses
FEM	Finite Element Method
FFT	Fast Fourier Transform
GWEC	Global Wind Energy Council
HAWT	Horizontal Axis Wind Turbine
IEC	International Electrotechnical Commission

IFE	Institute for Energy Technology
ISSC	International Ship and offshore Structures Congress
JONSWAP	Joint North Sea Wave Project
LC	Load Case
MDOF	Multi-Degree-Of-Freedom
MSL	Mean Sea Level
NGI	Norwegian Geotechnical Institute
NMBU	Norwegian University of Life Science
NREL	National Renewable Energy Laboratory
NTNU	Norwegian University of Science and Technology
OWT	Offshore Wind Turbine
P-M	Pierson-Moskowitz
PSD	Power Spectral Density
REDWIN	REDucing cost in offshore WIND by integrated structural design
SDOF	Single-Degree-Of-Freedom
SSI	Soil - Structure Interaction
SWL	Still Water Level
ULS	Ultimate Limit State

Greek letters

α	Power Law coefficient	[-]
$\Delta\sigma$	Stress range	[Pa]
Δt	Time interval	[s]
δ	Element size	[m]
η	Sea surface elevation	[m]
γ	Peak-enhancement factor	[-]

γ'	Submerged soil unit weight	[kN/m ³]
κ	von Karman's constant	[-]
λ	Wave length	[m]
ν	Poisson ratio of pile	[-]
ν_s	Poisson ratio of soil	[-]
ω	Angular frequency	[rad/s]
ω_0	Fixed-base natural frequency	[rad/s]
ω_{eq}	Equivalent natural frequency	[rad/s]
ω_r	Rocking natural frequency	[rad/s]
ω_u	Translational natural frequency	[rad/s]
ϕ	Friction angle	[deg]
ρ_a	Density of air	[kg/m ³]
ρ_w	Density of water	[kg/m ³]
σ	Normal stress	[kPa]
σ_a	Stress amplitude	[Pa]
σ_m	Mean stress	[Pa]
σ_U	Standard deviation of mean wind speed	[m/s]
σ_{max}	Maximum stress	[Pa]
σ_{min}	Minimum stress	[Pa]
τ_{max}	Shear strength of soil	[kPa]
ε_{50}	Strain at 50% the maximum deviator stress	[-]
ε_{vol}	volumetric strain	[-]
ρ	Spectral width parameter	[-]
ξ	Logarithmic decrement	[-]
ζ_{soil}	Soil damping ratio	[-]
ζ_{struct}	Structural damping ratio	[-]

ζ_{tot}	Total damping ratio	[-]
---------------	---------------------	-----

Lowercase letters

\mathbf{t}	Load vector	[N],[Nm]
--------------	-------------	----------

\mathbf{v}	Displacement vector	[m],[rad]
--------------	---------------------	-----------

\mathbf{v}^e	Elastic displacement vector	[m],[rad]
----------------	-----------------------------	-----------

\mathbf{v}^p	Plastic displacement vector	[m],[rad]
----------------	-----------------------------	-----------

$\log \bar{a}$	Intercept of $\log N$ axis by S-N curve	[-]
----------------	---	-----

c	Cohesion	[kPa]
-----	----------	-------

d	Water depth from still water level	[m]
-----	------------------------------------	-----

dF	Hydrodynamic load	[N/m]
------	-------------------	-------

dF_D	Hydrodynamic drag load	[N/m]
--------	------------------------	-------

dF_M	Hydrodynamic inertial load	[N/m]
--------	----------------------------	-------

f	Frequency	[Hz]
-----	-----------	------

f_p	Spectral peak frequency	[Hz]
-------	-------------------------	------

g	Acceleration of gravity	[m/s ²]
-----	-------------------------	---------------------

h	Height above ground of zero wind speed	[m]
-----	--	-----

k	Thickness exponent	[m]
-----	--------------------	-----

m	Negative slope on the $\log N$ - $\log \Delta \sigma$ plot	[-]
-----	--	-----

n_i	Number of cycles occurring of stress range i	[cycles]
-------	--	----------

p	Soil reaction	[kN/m]
-----	---------------	--------

p_u	Ultimate bearing capacity of soil	[kN/m]
-------	-----------------------------------	--------

s_u	Undrained shear strength of soil	[kPa]
-------	----------------------------------	-------

t	Thickness	[m]
-----	-----------	-----

t_{ref}	Reference thickness	[m]
-----------	---------------------	-----

y	Lateral displacement of soil	[m]
-----	------------------------------	-----

z_0	Surface roughness	[m]
z_{ref}	Reference height above surface	[m]

Uppercase letters

$[C]$	Damping matrix	[Ns/m],[Ns/rad],[Nsm/m],[Nsm/rad]
$[K]$	Stiffness matrix	[N/m],[N/rad],[Nm/m],[Nm/rad]
$[M]$	Mass matrix	[kg]
A_C	Wave crest height	[m]
A_T	Wave trough depth	[m]
C_D	Hydrodynamic drag coefficient	[-]
C_M	Hydrodynamic inertia coefficient	[-]
D	Outer diameter of pile	[m]
$D_{f,tot}$	Total fatigue damage	[year ⁻¹]
D_f	Fatigue damage from a stress history	[year ⁻¹]
E	Young's modulus	[Pa]
G	Shear modulus	[Pa]
H	Wave height	[m]
H_s	Significant wave height	[m]
H_x	Horizontal load in x-direction	[N]
I_p	Polar moment of inertia	[m ⁴]
I_u	Turbulence intensity in the direction of the mean wind speed	[%]
J	Empirical constant	[-]
K_b	Bulk modulus	[Pa]
L_k	Integral length scale	[m]
L_{pile}	Length of the pile	[m]
M_y	Moment about the y-axis	[Nm]

N	Number of cycles to failure	[-]
N_i	Number of cycles to failure in stress range i	[cycles]
P_i	Probability of occurrence of stress history i	[-]
$S_{JONSWAP}$	JONSWAP spectrum	[(m ² /Hz)]
S_{Kaimal}	Kaimal spectrum	[(m/s) ² /Hz]
T	Wave period	[s]
T_p	Spectral peak period	[s]
U	Mean wind speed at height z above ground	[m/s]
U_c	Current velocity	[m/s]
U_{ref}	Mean wind speed at reference height	[m/s]
W^P	Plastic work	[J]
1P	Rotation frequency of wind turbine rotor	[Hz]
3P	Blade passing frequency for three-bladed wind turbine	[Hz]

Chapter 1

Introduction

1.1 Background and Motivation

As concerns about global warming, energy security and a potential fossil fuel depletion increased towards the end of the 20th century, world politicians started agreeing on a necessary shift towards more renewable energy sources (Manwell et al. 2010). In 1997, the Kyoto protocol was signed, demanding several countries to reduce their greenhouse gas emission. Recent focus, such as the Paris Agreement (signed in 2015), indicate the current political interest in taking action against climate change. Further investment in the renewable energy industry is therefore to be expected for the years to come (GWEC 2015).

In the light of the focus on renewables, offshore wind has grown to become a significant source for energy harvesting. The key benefit of utilizing offshore locations for wind energy harvesting is the better wind quality over the oceans. The smoother surface of the sea compared to land result in stronger and less turbulent winds. Hence, ensuring a greater and more reliable power production, as well as reducing the fatigue loading on the turbine generator. However, wind turbines for offshore applications demand a higher cost and complexity of installment, maintenance and structural design, due to a more extreme environment and limited accessibility (Esteban et al. 2011). Despite this, there is currently a large investment in offshore wind technology. According to the Global Wind Energy Council (GWEC) (2015), offshore wind accounted for almost a quarter of the total wind power installations in the EU in 2015. This was more than double the annual addition of offshore installations from the year before.

Developers have increased the efficiency of offshore wind turbines (OWTs) by applying larger diameter rotors, and installing wind farms further from the coast, where the wind speeds are higher. This has resulted in turbines with greater outputs, and consequently an increased cost-efficiency of offshore wind energy (Haiderali and Madabhusi 2012).

However, up to 20% of the capital costs of OWTs correlate to their support structures (Aasen et al. 2017), yet geotechnical and foundation issues in design are commonly solved by overly conservative approaches. More accurate modeling of soil-structure interaction (SSI), in particular concerning design predictions of foundation stiffness and damping, is believed to achieve large potentials for cost reductions in the foundation design. The capital costs of OWTs are closely related to material usage, and, according to Kallehave et al. (2015), reductions of steel tonnage in the range of 10-25% are not unreasonable. To reach this optimization potential, more accurate models of the soil response, assessment of damping and accurate fatigue damage calculations are essential.

The REDWIN project (*REDucing cost in offshore WIND by integrated structural and geotechnical design*) is a research project lead by the Norwegian Geotechnical Institute (NGI), which aims to reduce the cost of offshore wind energy by improving the soil-foundation models used in the design of bottom-mounted OWTs. As part of this project, a new foundation model for monopile foundations has been developed. This thesis contributes to the project by investigating the pile optimization potential of applying this model in fatigue assessments, as compared to the common industry practice of using API p - y curves.

1.2 Foundation Concepts

Several foundation concepts exist for OWT application, and upon selection of foundation type, evaluations on soil conditions, water depth and economics are essential. Some typical foundation types for bottom-mounted OWTs are illustrated in Figure 1.1.

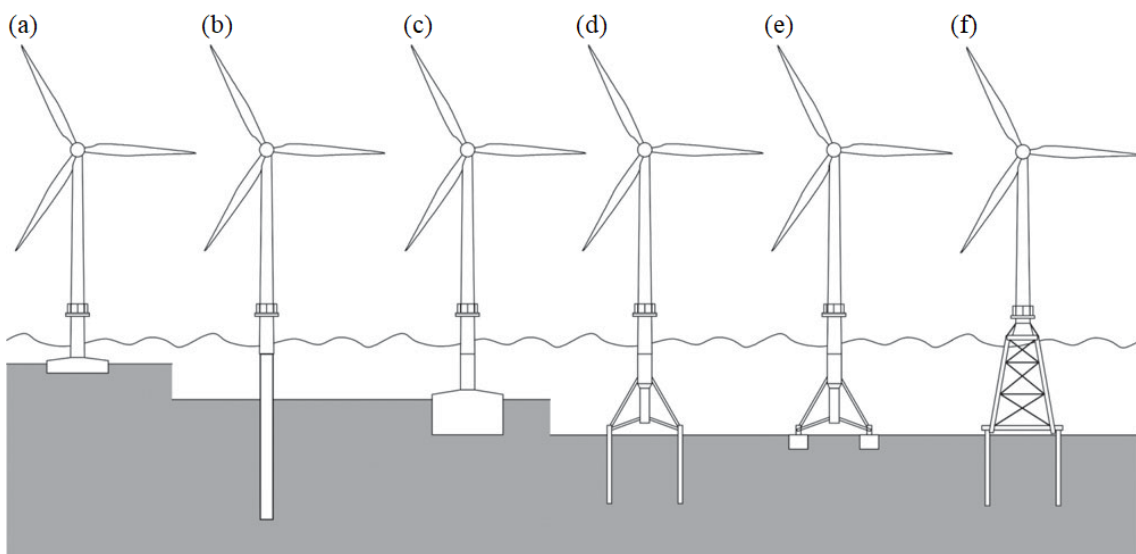


Figure 1.1: Common foundation types for bottom-mounted OWTs. a) Gravity based foundation, b) Monopile foundation c) Caisson foundation, d) Multipile foundation, e) Multi caisson foundation and f) Jacket foundation (Kallehave et al. 2015).

The *monopile* foundation is a large diameter cylindrical steel tube, driven into the seabed, and is by far the most commonly applied foundation type, accounting for about 75% of all installed capacity (Page et al. 2018). According to Kallehave et al. (2015), monopiles are currently installed at water depths up to 35m, and with new optimized models, monopiles could be economically applicable for water depths of 40m. Hence, it is expected that, even with installments at deeper waters, monopiles will continue to be the popular choice.

1.3 General Terminology

A simple illustration of the general terminology used in this thesis is given in Figure 1.2.

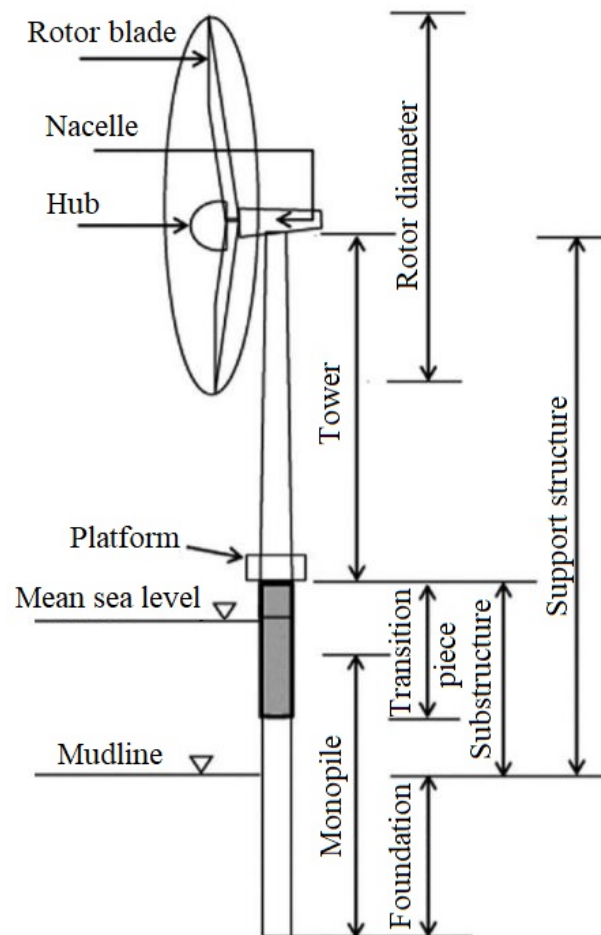


Figure 1.2: General terminology used in this thesis for a monopile OWT (Arshad and O’Kelly 2016).

The focus of this thesis has been on horizontal axis wind turbines (HAWTs). The HAWTs use lift to obtain the rotating effect that generates power. There exists both two- and three-bladed HAWTs, the three-bladed ones being the most commonly used. As Figure 1.2 illustrates, the HAWTs consist of a hub, rotor and a nacelle that connects the rotor to the

tower. The substructure of the turbine extends from some meters above the mean sea level (MSL) (or still water level (SWL)) to the mudline, where the foundation is defined as the part extending beneath the mudline. There is a transition piece connecting the monopile to the tower.

Figure 1.3 illustrates the coordinate system used throughout this thesis, with the commonly applied terminology for directional motion. Analogous terminology for sway and surge are side-to-side and fore-aft, respectively.

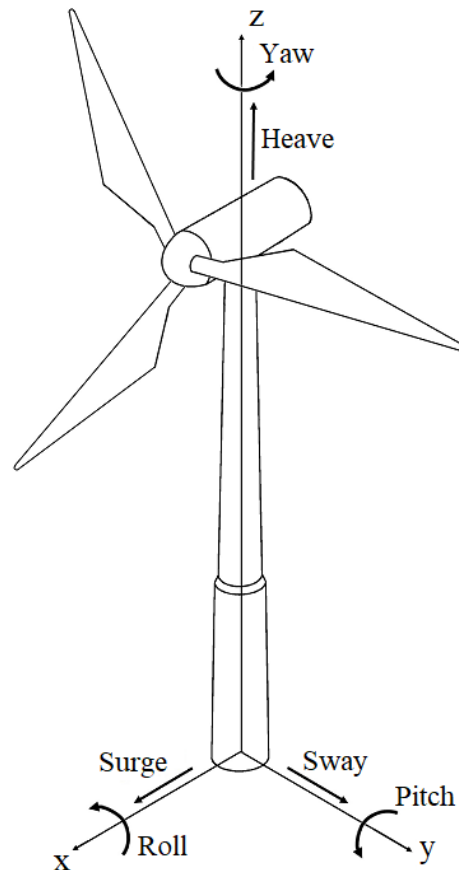


Figure 1.3: Coordinate system used throughout this thesis.

HAWTs can either be faced upwind (hub faced towards the wind) or downwind (hub faced from the wind), where the most common configuration is upwind.

1.4 Previous Research

The API p - y method has shown to be successful in design applications of piles with a large length to diameter ratio, designed to withstand axial loads, as used in the oil and gas industry (Arshad and O'Kelly 2016). However, their usefulness for large diameter piles under lateral loading has shown limitations, and their validity to monopile foundation

design for offshore wind applications, has been questioned. Many studies on foundation modeling for monopile OWT design has therefore been conducted.

Mardfekri et al. (2013) has conducted studies comparing finite element (FE) results to those obtained from the p - y method, for various diameter piles. The study applied the p - y formulations as described by Reese et al. (1975) and Reese et al. (1974) for stiff clay and sand respectively. For the 1 meter diameter pile at the clay site, the p - y method and the FE method showed deviations of only 1% of the mudline displacements. However, with larger diameter piles, the inaccuracy of the p - y method increased. For the pile with a diameter of 4 meters, the p - y method obtained mudline displacements that were 50% larger than those obtained from the FE model. In contrast, the 4 meter diameter pile situated in sand, only obtained deviations of the mudline displacements of 5% between the two methods of modeling.

Byrne et al. (2015) found the method based on API and DNV p - y curves to significantly under predict the ultimate capacity and stiffness of large diameter monopiles in clay. In correspondence with Mardfekri et al. (2013), they also found the predicted stiffness at sand-dominated sites to be more accurate.

Kallehave et al. (2015) have performed fatigue calculations and compared the measured fundamental frequency of OWTs to their estimated design frequency. They found the estimated frequencies to, in general, be under predicted. By a reassessment of a structure's natural frequency and wave loads based on measurements, they found a total increase in the expected fatigue life of the particular OWT by 88%. Based on this, they obtained a realized value of potential steel savings, at the studied wind farm, in the range of 20 - 25%.

Aasen et al. (2017) compared different soil-foundation models to investigate how stiffness and damping influence the fatigue damage on a monopile-based OWT. Their study indicated that damping alone had a significant effect on the total fatigue damage on the structure. A comparison of two models with similar fundamental frequency, showed that the estimated fatigue damage was reduced by 13% when including foundation damping with a factor of 0.3%. Additionally, they found the softest model, although not the API p - y model, to result in the largest accumulated fatigue damage.

As part of his Master's thesis, Aasen (2016) studied the fatigue damage sensitivity to foundation modeling at various positions on a monopile-based OWT. His studies indicated that, among the positions investigated, the positions most sensitive to foundation modeling, was the tower root and at the mudline. Between the two, the structure obtained the largest estimates on fatigue damage at the mudline.

As the literature has indicated large limitations of the p - y method, there is an obvious need for better foundation models to ensure future development in the offshore wind industry. Many improved model formulations have been attempted. These have aimed to

improve the modeling of foundation damping (Beuckelaers 2015), or on improvements of the stiffness response (Byrne et al. 2015). The *macro-element model* studied in this thesis, however, has shown to provide simultaneous accurate modeling of both the foundation stiffness- and damping (Page et al. 2018). A broader description of this model will be presented in Chapter 5.

Keeping in mind the indicated limitations of the industry practice by applying API p - y curves, this thesis will assess the optimization potential of applying a more accurate foundation model in fatigue calculations. The optimization potential will be assessed, mainly with regards to fatigue damage at the mudline, as Aasen's (2016) studies has highlighted this position's sensitivity to foundation modeling and magnitude of fatigue damage estimates. Additionally, a short study on the fatigue damage along the foundation will be performed, as this has been given little attention in previous research. The thesis consider clay-dominated sites, as a lower accuracy of the API p - y model has typically been observed in literature for sites dominated by clays.

1.5 Objectives

The motivation for this study bases on the observed limitations in the industry practice of using API p - y curves in monopile-based OWT design, and the need for better foundation models to exploit the possibilities of cost reductions in offshore wind. The main objectives are:

- To assess the accuracy of different foundation models by comparisons with measured data from an installed monopile-based OWT in the North Sea.
- To investigate the optimization potential of monopile OWT foundations, with regards to fatigue estimates, through using a more reliable foundation model as an alternative to today's industry practice.

To achieve this, the following tasks needed to be performed:

- Establishing a FE model of the pile foundation and surrounding soil, that accounts for the soil-structure interaction, for model calibration.
- Obtaining the API p - y curves corresponding to the selected soil profiles, as well as extracting FEA p - y curves from finite element analyses.
- To build inputs to 3DFloat that includes the different foundation models, and perform time-domain integrated analyses.

1.6 Thesis Outline

The theory is presented in Chapters 2 through 5.

Chapter 2 provides a presentation of the ocean environment, focusing on wind- and wave loads on OWTs, as well as spectral representations of wind- and wave statistics.

Chapter 3 presents the fundamental concepts of fatigue, and how to apply this to OWT design.

Chapter 4 covers some of the main design concerns of monopile foundations, relating to the foundation flexibility and damping.

Chapter 5 presents basic theory on soil mechanics, and proceeds to describe the two soil-structure interaction models studied in this thesis.

A description of the modeling and validation of the finite element model created for this thesis, is provided in *Chapter 6*.

Furthermore, *Chapter 7* provides a brief introduction to the computational tool 3DFloat, that has been used for time-domain integrated simulations.

Chapter 8 presents an analysis on fatigue assessments and optimization potential of a monopile-based OWT situated at an idealized clay site.

In *Chapter 9*, a real site analysis is presented, assessing the accuracy of the different foundation models, as well as assessing the sensitivity to foundation modeling with regards to fatigue calculations.

Finally, *Chapter 10* will shortly summarize and conclude the main findings of the thesis, and provide recommendations for further work.

1.7 Software Used

The following computer programs were used in this thesis:

- Abaqus, a software for finite element analyses (FEA) and computer aided engineering (CAE), SIMULIA
- 3DFloat, an aero-servo-hydro-elastic CAE tool for calculating the dynamic response of offshore wind turbines, IFE and NMBU
- MATLAB, a general purpose mathematical modeling program, Math Works Inc.

Chapter 2

Ocean Environment

The design of OWTs is highly dependent on site-specific metocean conditions, and an appropriate description of the ocean environment is therefore crucial (Chakrabarti 2005). Figure 2.1 illustrates the environmental impacts OWTs may be exposed to.

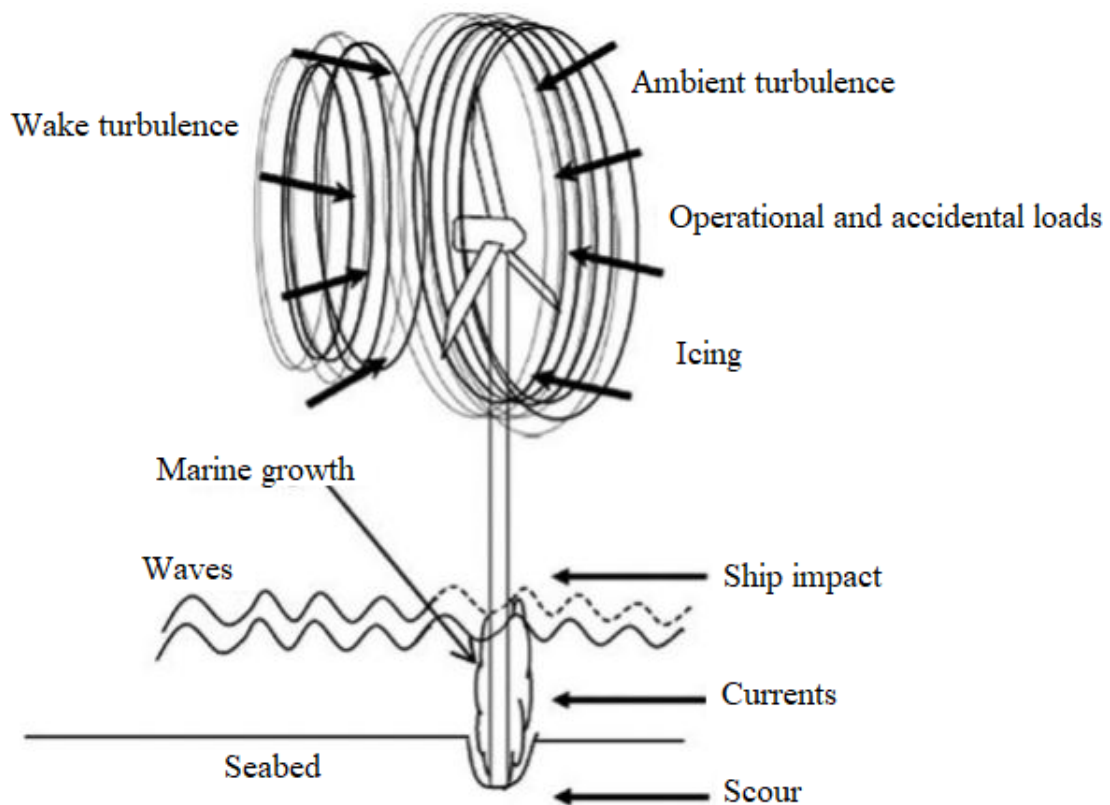


Figure 2.1: Environmental impacts on an offshore wind turbine (Arshad and O’Kelly 2016).

The most significant environmental loading on OWTs are the wind and wave loads. These are stochastic (or random) processes, and consequently, cannot be reproduced or predicted in detail. However, if the joint probability distribution of a stochastic process is invariant

of time, the process is said to be *stationary*. This entails that the averages, means, standard deviations, variances and mean squares are independent of time all together. Furthermore, a stochastic process is ergodic if, in addition to being stationary, the statistical properties of the process are completely represented by a single, sufficiently long, sample of the process (Newland 2005). Wind and wave histories are, with good accuracy, assumed to be stationary ergodic random processes, which is an essential assumption for statistical representations of wind and wave conditions.

The equation of motion for a multi-degree-of-freedom (MDOF) system is, in the time-domain, given by

$$[M]\{\ddot{u}(t)\} + [C]\{\dot{u}(t)\} + [K]\{u(t)\} = \{F\}(t) \quad (2.1)$$

where $\{F\}(t)$ is a vector containing the external loads, $[M]$, $[C]$ and $[K]$ are the mass, damping and stiffness matrices, respectively, and $\{u(t)\}$ is the displacement vector, where the velocity vector is given as its time derivative, $\{\dot{u}(t)\}$, and the acceleration vector is given as its double time derivative, $\{\ddot{u}(t)\}$. Hence, as the wind and wave loads (represented in $\{F(t)\}$) are random processes, the response of an OWT structure (described in $u(t)$, $\dot{u}(t)$ and $\ddot{u}(t)$), will be random as well.

Fourier Transform and Power Spectral Density

In OWT analyses, data is usually processed in the time-domain. However, wave and wind loading are often described by statistical formulations in the frequency domain. Such formulations are known as *power spectral densities* (PSDs), and describes the energy distribution along the frequency axis (Newland 2005). The *Fourier transform* converts a random signal from the time-domain to the frequency domain, and reverse by its inverse, as illustrated in Figure 2.2.

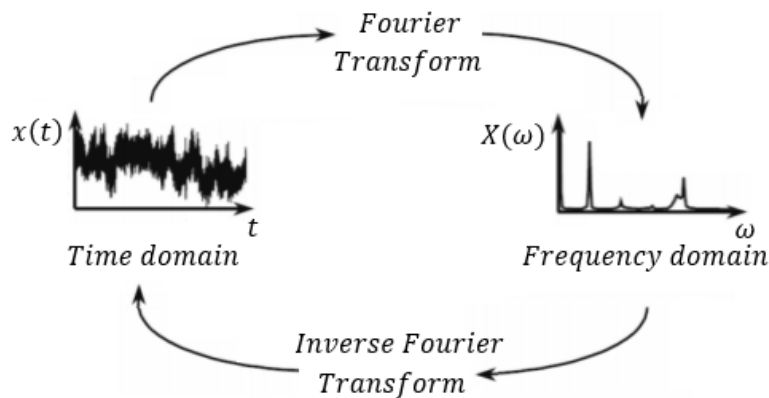


Figure 2.2: Conversion between frequency- and time-domain by Fourier transform.

The Fourier transform and its inverse is given by Newland (2005) as

$$X(\omega) = \frac{1}{2\pi} \int_{-\infty}^{\infty} x(t)e^{-i\omega t} dt \quad (2.2)$$

$$x(t) = \int_{-\infty}^{\infty} X(\omega)e^{i\omega t} d\omega \quad (2.3)$$

For a discrete signal, $x_r(t)$, values are measured at a constant time interval $\Delta t = T/N_t$, where T is the total sample length, and N_t is the total number of time steps. The *discrete Fourier transform* (DFT) is, by Newland (2005), given as

$$X_k(f) = \frac{1}{T} \sum_{r=0}^{N_t-1} x_r e^{-i2\pi k r / N_t} \quad (2.4)$$

The DFT can be found from the the *fast Fourier transform* (FFT) algorithm (Newland 2005). Furthermore, the PSD is related to the DFT by

$$S_x(f) = \lim_{T \rightarrow \infty} \frac{1}{T} E[|X_k(f)|^2] \quad (2.5)$$

where $E[|X_k(f)|^2]$ is the mean value of $|X_k(f)|^2$.

Real measured signals contain much noise, and some sort of averaging is needed to make the signal less noisy. The *Welch's method* may be used for this purpose. The method divides the original signal into different segments, or *windows*, and averages the spectra of these. The consequence is less narrow peaks in the PSD, as the signals to which the FFT is applied is shortened. However the accuracy of the PSD increases.

2.1 Wind Modeling

Understanding the characteristics of wind is very important for safe and serviceable design. This section will present the basic characteristics of wind, as well as common ways to model it.

2.1.1 Wind Characteristics

Winds are caused by the variable temperature gradient of the atmosphere due to the sun's heating the earth's surface. As the wind is constantly changing in speed and direction, the main characteristics of wind is the mean wind speed, U , and the fluctuations about this mean (u, v, w) in the x-, y- and z-directions (Cao 2013).

Wind speed varies randomly in time. The time varying character of the wind can be measured and represented in form of a wind spectrum, covering large frequency ranges.

Such a spectrum, by Isaac Van der Hoven (1956), is presented in Figure 2.3.

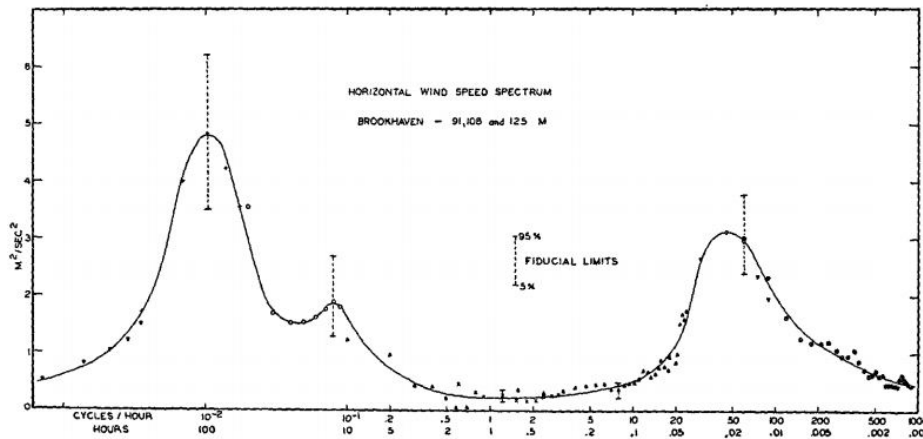


Figure 2.3: Horizontal wind-speed spectrum (Hoven 1956).

The spectrum represents the turbulence-energy spectrum at different frequency ranges. Consequently, the peaks represent frequencies of which there are large amounts of wind-speed fluctuations. The peak furthest to the left corresponds to a period of 4 days, and represents wind-speed fluctuations due to migratory pressure systems, whereas the peak furthest to the right corresponds to mechanical and convective types of wind-speed fluctuations, caused by e.g. topographical effects (Hoven 1956; Cao 2013). The *spectral gap* describes the low-energy part of the spectrum, ranging from periods around 10 minutes to 1 hour, indicating little fluctuation of the wind speed in this frequency range. Over this period, stationary conditions with constant mean wind and standard deviation, σ_U , can be assumed with good accuracy (DNV 2010). Det Norske Veritas (DNV) (2010) suggests using periods of 10 minutes when estimating the mean wind speeds for offshore applications.

Wind speed also varies with height above the ground or sea surface. Consequently a reference height must be specified, at which the mean wind speed will be determined. For wind turbines, the mean wind speed at the hub height should be used as reference (DNV 2014).

2.1.2 Wind Representation

The region close to the earth's surface, where frictional forces from the earth still affects the wind, is known as the *atmospheric boundary layer* (ABL). In this region, the mean wind will vary with altitude, with a rate of change known as *wind shear*. At a certain altitude, the wind shear will vanish, and the wind reaches its undisturbed value (Cao 2013). There exist several models for representing the mean wind profile in the ABL, the two most commonly used being the power law, and the logarithmic profile.

Power Law

The power law describes the wind profile through Equation 2.6 (Cao 2013)

$$U(z) = U_{ref} \left(\frac{z-h}{z_{ref}} \right)^\alpha \quad (2.6)$$

where $U(z)$ is the mean wind speed at height z , U_{ref} is the reference mean wind speed at reference height z_{ref} , h is the height above ground at which zero wind speed is achieved (for offshore sites, $h = 0$) and α is the power law coefficient.

Logarithmic Profile

The logarithmic profile is expressed in Equation 2.7 (Cao 2013)

$$U(z) = \frac{u^*}{\kappa} \ln \left(\frac{z-h}{z_0} \right) \quad (2.7)$$

where z_0 is the surface roughness and $\kappa = 0.4$ is the von Karman's constant. The friction velocity, $u^* = \sqrt{\tau/\rho_a}$ have been introduced, with τ being the surface shear stress and ρ_a the air density.

The surface roughness usually varies between 0.0001m at open ocean to 0.003m in coastal areas, and may be solved implicitly from the following equation (DNV 2014)

$$z_0 = \frac{C_a}{g} \left(\frac{\kappa U}{\ln(z/z_0)} \right)^2 \quad (2.8)$$

where g is the acceleration of gravity and C_a is Charnock's constant.

2.1.3 Turbulence

The mean wind speed profiles described above represents the wind speed as a steady flow of air that is only varying with altitude. The actual wind speed, however, is very irregular and deviates from the mean wind profile in both speed and direction, as a result of turbulence (Tempel et al. 2010). This is illustrated in Figure 2.4.

Turbulence is dependent on height, wind speed and surface roughness. In general, the turbulence intensity is lower offshore, and is decreasing with higher wind speeds (Karimirad and Moan 2012).

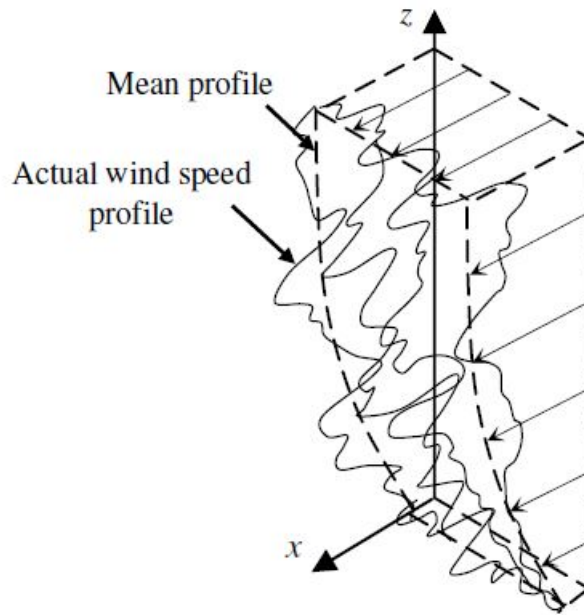


Figure 2.4: True wind profile (Tempel et al. 2010).

A measure of the turbulence is given by its intensity, I_u, I_v and I_w in the x-, y- and z-direction, respectively. The turbulence intensity is a function of the standard deviation in the fluctuating direction, and the mean wind speed. The turbulence intensity component in the mean wind direction is, in general, more significant than the other two, and is given by Equation 2.9 (Cao 2013).

$$I_u = \frac{\sigma_u}{U} \quad (2.9)$$

2.1.4 Wind Spectrum

The wind climate can be represented by a power spectrum, expressing the frequency distribution of the wind speed (DNV 2014). There exists several models of expressing the spectral density of the wind field, including the *von Kármán spectrum*, the *Kaimal spectrum*, the *Davenport spectrum*, etc. These spectra are used in wind generating software, such as TurbSim (see Chapter 7). In general, they agree in the high frequency range, yet they may vary significantly in the low frequency range (DNV 2010). According to Det Norske Veritas (2014), the Kaimal spectrum should be used, unless data indicate otherwise. The expression for the Kaimal spectrum is given by Equation 2.10 (DNV 2014)

$$S_{Kaimal}(f) = \sigma_U^2 \frac{4L_k/U}{(1 + 6fL_k/U)^{5/3}} \quad (2.10)$$

where f is the frequency and the integral length, L_k , is given as

$$L_k = \begin{cases} 5.67z & \text{for } z < 60\text{m} \\ 340.2\text{m} & \text{for } z \geq 60\text{m} \end{cases} \quad (2.11)$$

where z denotes the height above the ground or water surface.

2.2 Wave Modeling

The two most important features contributing to the sea elevation are wind waves and swell. Wind waves are ripples in the water surface caused by local surface winds, generally with short periods. In contrast, swell are long-period waves traveling far from their origin (Chakrabarti 2005), and is in no way related to the local winds (DNV 2010). This section will give a description of different wave theories, and how to model the sea state.

2.2.1 Wave Theories

Ocean waves are irregular and random in nature and are therefore difficult to describe. However, larger waves in a random wave series may be assumed to take a regular shape, allowing for a deterministic description of the wave kinematics (Chakrabarti 2005). Regular waves are propagating with permanent shape, having a distinct wave length λ , wave period T and wave height H . Figure 2.5 illustrates a regular wave and its characteristics.

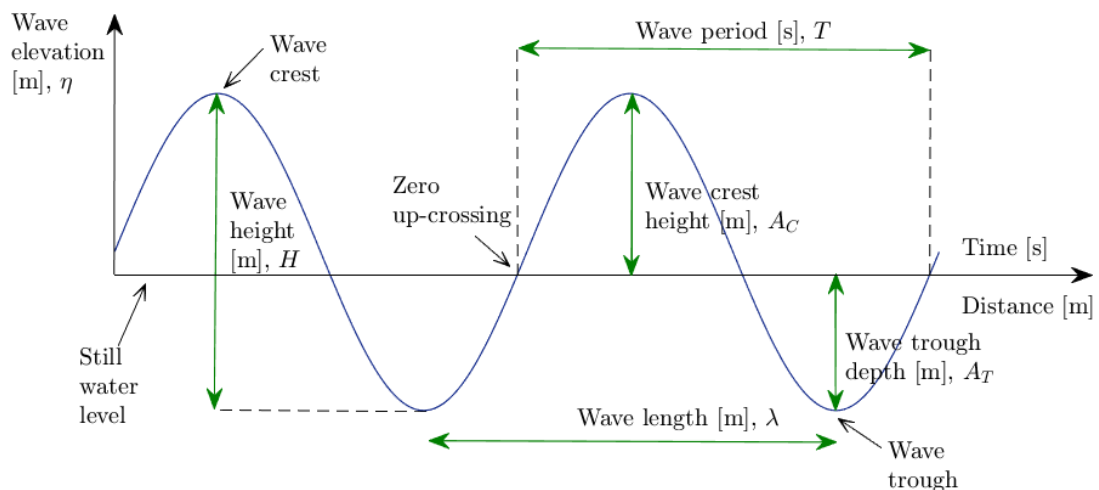


Figure 2.5: Wave description.

The surface elevation, η , describes the distance between the wave surface and the still water level (SWL). The wave crest height, A_C , and the wave trough depth, A_T , represents

the distance from the SWL to the wave crest and the wave trough respectively. The wave height is the vertical distance from trough to crest, and the wave period is defined as the time between two successive zero-upcrossings.

For all wave theories, the ocean floor is assumed horizontal and flat (DNV 2010). Some commonly applied wave theories will be described in the following, where their applicability ranges are presented in Figure 2.6.

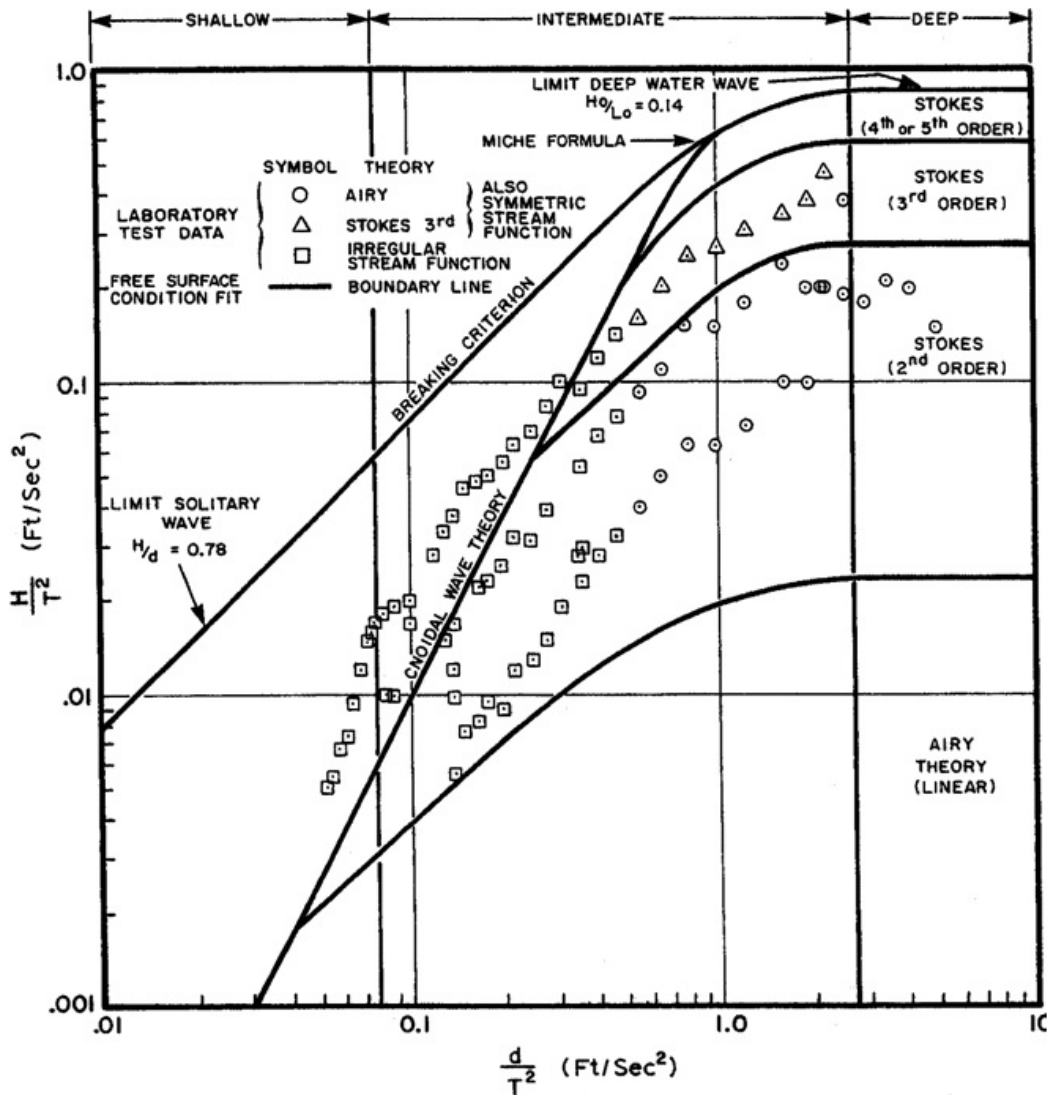


Figure 2.6: Ranges of validity for various wave theories (DNV 2014).

Airy Wave Theory

The simplest wave theory is the *Airy wave theory* (also known as linear wave theory). The Airy wave theory models the wave propagation as a simple harmonic function varying between wave crest and wave trough. The general expression for the wave propagation in Airy wave theory is, according to Det Norske Veritas (2014), given by

$$\eta(x,y,t) = \frac{H}{2} \cos\Theta \quad (2.12)$$

where, $\Theta = k(x\cos\beta + y\sin\beta) - \omega t$, is the wave phase, $k = 2\pi/\lambda$, is the wave number and β , describes the direction of wave propagation. The model describes the elevation of the wave both in time and space, such that it can give the instantaneous surface elevation at any position (x,y) . The theory is often sufficient for offshore applications, especially in deep waters, but also in shallower areas where the wave height is much smaller than both the wave length and the water depth (DNV 2014).

Higher Order Wave Theories

At a certain ratio between the wave height on the wave length or on the water depth, the Airy wave theory becomes inapplicable. In those cases, higher order wave theories must be applied, such as *Stokes' wave theories*, *stream function theory*, *solitary wave theory*, etc.

The higher order regular wave theories describe a wave propagation which is symmetric front-to-back, but asymmetric crest-to-trough. In predictions of wave forces for fatigue assessments, Det Norske Veritas (2014) recommends the use of Stokes 5th order theory when water depths exceed 30m, and the use of higher order stream function theory for water depths of less than 15m.

Stokes' Wave Theories

In general, Stokes' wave theories are based upon combining several components of harmonic functions of different frequencies, where the order of the theory indicates how many components that are included. The first component is equal to the shape given by Airy wave theory, whereas the following components will all be of higher frequency and lower amplitude than the prior. By summing the components, the resulting description becomes a wave profile with a steeper crest and a shallower trough, as Figure 2.7 indicate for 5th order Stokes' wave theory (Chakrabarti 2005).

Stream Function Theory

The stream function theory is purely numerical, and the validity of the model is broader than the wave theories already mentioned. The general solution for the stream function theory is, according to Det Norske Veritas (2014), given by

$$\Psi(x,z) = cz + \sum_{n=1}^N X(n) \sinh(nk)(z+h) \cos(nkx) \quad (2.13)$$

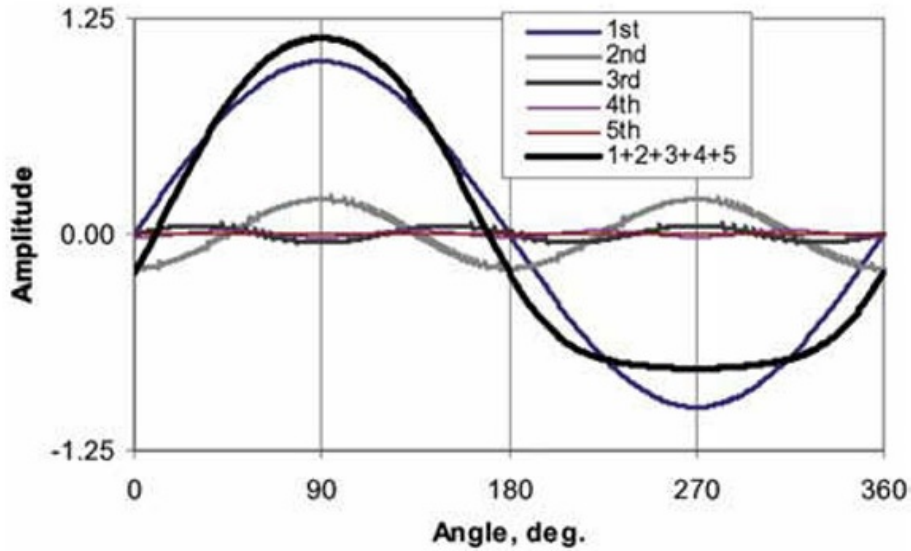


Figure 2.7: Example of components for Stokes 5th order wave theory (Chakrabarti 2005).

Wave Stretching and Extrapolation

The stream function theory provides wave kinematics up to the free surface elevation. However, this do not apply to Airy waves and Stokes waves, as they only account for wave kinematics up to the still water level. Thus, by implementing stretching formulas or extrapolation, as illustrated in Figure 2.8, predictions of fluid velocity and acceleration between the crest and the SWL can be estimated for these wave theories.

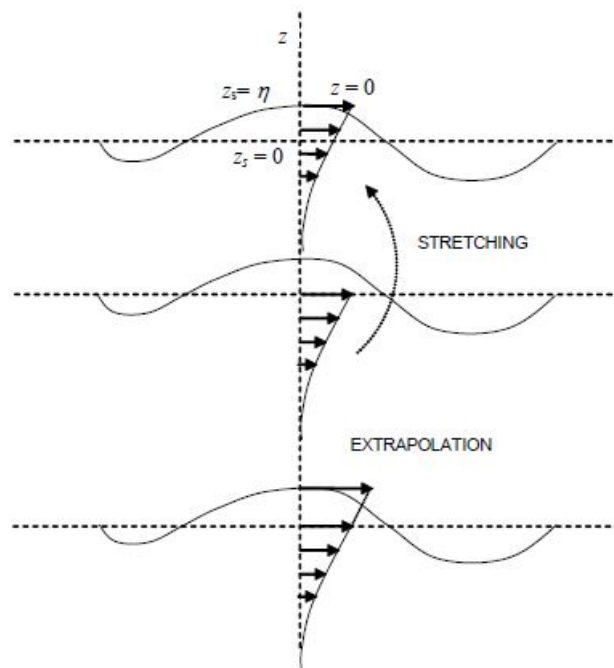


Figure 2.8: Stretching and extrapolation of velocity profile (DNV 2010).

2.2.2 Wave Representation

The wave climate is described by the significant wave height, H_s , and the spectral peak period, T_p . The short-term sea state is assumed a stationary random process, for time periods normally between 3 or 6 hours (DNV 2014). In this period, H_s and T_p can, due to stationary conditions, be assumed constant. The wave height, H , and the wave period, T , will, in the short-term stationary sea state, follow probability distributions based on H_s and H_s, T_p and H , respectively (DNV 2014). The short-term sea state may be represented by a wave spectrum that is dependent upon the values of H_s and T_p , expressing the energy content of the sea elevation and its frequency distribution (Chakrabarti 2005).

Wave Spectrum

There are several different spectra representing the sea elevation process, the most common being the *Pierson-Moskowitz* (P-M) spectrum, the *Bretschneider* spectrum, the *International Ship and Offshore Structures Congress* (ISSC) spectrum and the *Joint North Sea Wave Project* (JONSWAP) spectrum (Chakrabarti 2005). Det Norske Veritas (2014) states that the JONSWAP spectrum should be used unless data indicate otherwise. The JONSWAP spectrum is given by Equation 2.14 (DNV 2014)

$$S_{JONSWAP}(f) = \frac{5}{16} \frac{H_s^2 f_p^4}{\pi^4} f^{-5} \exp\left(-\frac{5}{4} \left(\frac{f}{f_p}\right)^{-4}\right) \gamma \exp\left(-0.5 \left(\frac{f-f_p}{\rho f_p}\right)^2\right) \quad (2.14)$$

where f is the wave frequency (in Hz), f_p is the spectral peak frequency, ρ is the spectral width parameter and γ is the peak-enhancement factor defined as

$$\gamma = \begin{cases} 5 & \text{for } \frac{T_p}{\sqrt{H_s}} \leq 3.6 \\ \exp(5.75 - 1.15 \frac{T_p}{\sqrt{H_s}}) & \text{for } 3.6 < \frac{T_p}{\sqrt{H_s}} \leq 5 \\ 1 & \text{for } 5 < \frac{T_p}{\sqrt{H_s}} \end{cases} \quad (2.15)$$

For fully developed sea state ($\gamma = 1$), i.e. a sea state where the wind has transferred all of its energy to the waves, the JONSWAP spectral formulation reduces to the P-M spectrum. In other words, the JONSWAP spectrum is an extension to the P-M spectrum, accounting for developing sea states that are dependent on the fetch (DNV 2010).

2.2.3 Wave Loads on Structures

The wave particle kinematics can be used to calculate the hydrodynamic loads on a structure. For slender structures, Morison's equation can be applied for calculating the wave

loads (DNV 2014). However, as slenderness is a function of wave length and pile diameter, some monopiles are reaching the limit of the validity of the equation (Arshad and O’Kelly 2016). In those cases, some diffraction terms may be necessary.

The wave loads are, by Morison’s equation, given as the sum of drag and inertia loads on a vertical element dz of the structure, and is, in general, represented as in Equation 2.16 (DNV 2014).

$$dF = dF_D + dF_M \quad (2.16)$$

$$\text{where } \begin{cases} dF_D = C_D \frac{1}{2} \rho_w D |\dot{x}| \dot{x} dz \\ dF_M(x, z, t) = C_M \frac{\rho_w \pi D^2}{4} \ddot{x} dz \end{cases} \quad (2.17)$$

with dF_D and dF_M being the hydrodynamic drag and inertia loads respectively, ρ_w is the density of the water, \dot{x} and \ddot{x} is the water particles’ wave induced velocity and acceleration, respectively, and D is the outer diameter of the cylinder section. z is originated at the SWL, with a positive direction upwards. C_D and C_M are respectively the hydrodynamic drag and inertia coefficients, and are functions of the Reynolds number, the Keulegan-Carpenter number and the relative roughness.

When including the loads due to currents, the velocity term in the hydrodynamic drag load in the general form of Morison equation must be modified to

$$dF_D = C_D \frac{1}{2} \rho D |(\dot{x} + U_c)| (\dot{x} + U_c) dz \quad (2.18)$$

where U_c is the total current velocity (DNV 2014).

The horizontal force on the structure is found by integrating Morison’s equation from the seabed, $z = -d$, to the wave elevation, $\eta(t)$.

Chapter 3

Fatigue

OWTs are highly dynamic systems, whose support structures are exposed to millions of load cycles, of varying amplitude, throughout their design lives (Brennan and Tavares 2014). Thus, OWTs are very prone to high-cycle fatigue damage, often making fatigue a limiting factor in the design of the structures (Schafhirt et al. 2016). This chapter will present the basic concept of fatigue, and the method commonly used for fatigue damage calculations on OWTs.

3.1 Definition and Concepts

In material science, *fatigue* describes gradual degradation of a material over time due to constantly changing stresses. This cyclic loading will therefore promote premature failure in parts that would otherwise withstand these loads in a static case. Thus, fracture can occur at stresses much lower than the ultimate tensile strength or the yield stress limit of the material.

Above a certain stress threshold, microscopic cracks will start to form. With each cycle of sufficiently high stress range, these cracks will continue to grow, until the material experiences a sudden brittle fracture (Maleque and Salit 2014). Figure 3.1 presents a fatigue cycle, and its main components.

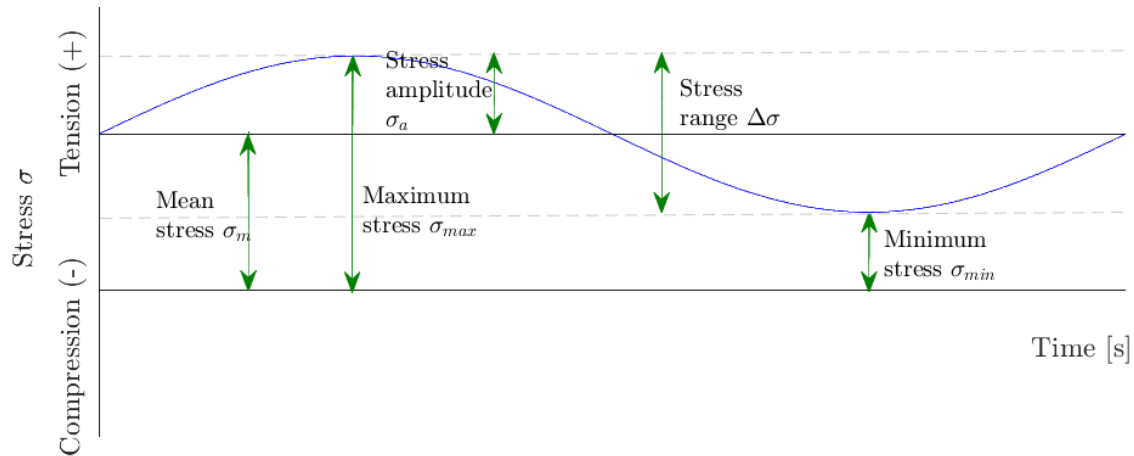


Figure 3.1: Example of a fatigue cycle in pure tension.

A common practice for calculating the fatigue damage on OWTs, based on S - N data, is presented by DNV GL (2016), and is summarized by the flowchart in Figure 3.2.

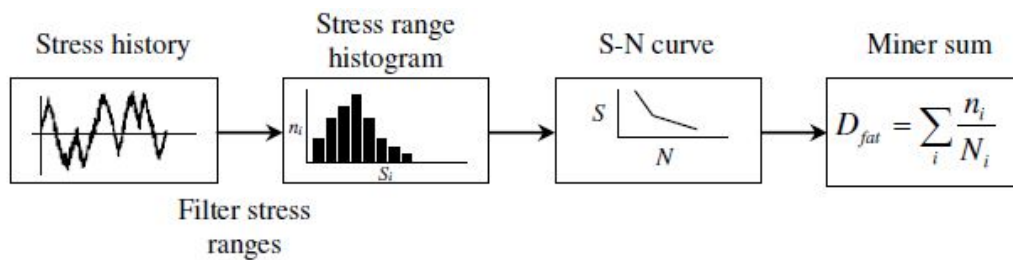


Figure 3.2: Flowchart for calculating fatigue damage using S-N curves and Palmgren-Miner sum (Tempel et al. 2010).

3.2 Stress History and Filtering

As the stress range, $\Delta\sigma$, is the decisive factor to the magnitude of the fatigue damage, fatigue calculations should be performed at the positions of the highest moments amplitudes. These are assumed to occur at the mudline for monopile support structures for OWT (Schafhirt et al. 2016), and fatigue calculations are therefore often performed at that location. Additionally, welds are extra sensitive to fatigue loads, and attention should be paid to the fatigue damage at the positions of the welds (Kallehave et al. 2015).

3.2.1 Obtaining the Stress Time History

The nominal local axial stress is found from data on the cross-sectional area, A_{cs} , the axial force, N_x , and the moments M_x and M_y about the x- and y-axis respectively, by use of Equation 3.1.

$$\sigma_x = \frac{N_x}{A_{cs}} + \frac{M_y}{I_y}x + \frac{M_x}{I_x}y \quad (3.1)$$

For a cylindrical pile, $x = r \cos \theta$ and $y = r \sin \theta$, as Figure 3.3 indicates.

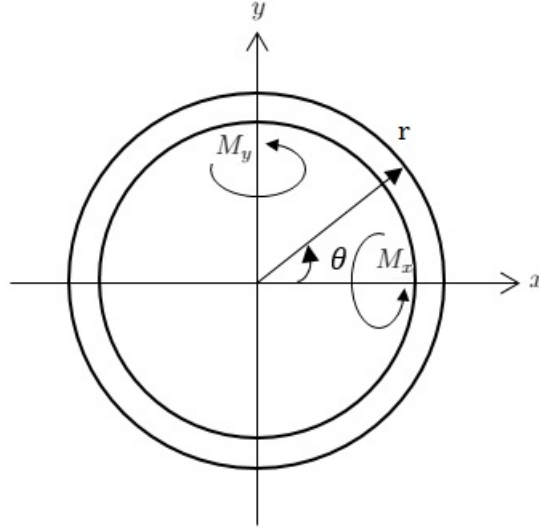


Figure 3.3: Moment on a cylindrical cross-section.

The contribution from the axial force will be significantly lower than from the bending moments, and can therefore be neglected. Furthermore, assuming that the loads are unidirectional in the x-direction, simplifies Equation 3.1 to

$$\sigma_x = \frac{M_y}{I_y}x \quad (3.2)$$

where the moment of inertia for a hollow cylinder, $I_y = I_x = I_p$, is expressed as

$$I_p = \frac{\pi(r^4 - (r-t)^4)}{4} \quad (3.3)$$

Here r is the outer radius, and t is the wall thickness of the pile.

3.2.2 Counting Methods

The stress cycles in a stress history can be identified and filtered through counting methods. There are various methods for filtering the stress ranges, both in the frequency- and in the time-domain. However, time-domain methods are preferred for wind turbines (Sanchez et al. 2015). The most common counting methods in the time-domain includes the peak counting method and rainflow counting, the latter being the most commonly

used for fatigue calculations of wind turbines (Sanchez et al. 2015), and will therefore be described in the following.

Rainflow Counting

In general, rainflow counting is a process that converts a random signal to a count of constant amplitude cycles. It measures ranges of the half-cycles in the signal, and have demonstrated to account for all peaks more accurately than other counting algorithms (Marsh et al. 2016). To visualize the principle behind rainflow counting, turn the stress history in Figure 3.4 by 90 degrees and imagine that the dotted lines represents water flowing down from the peaks.

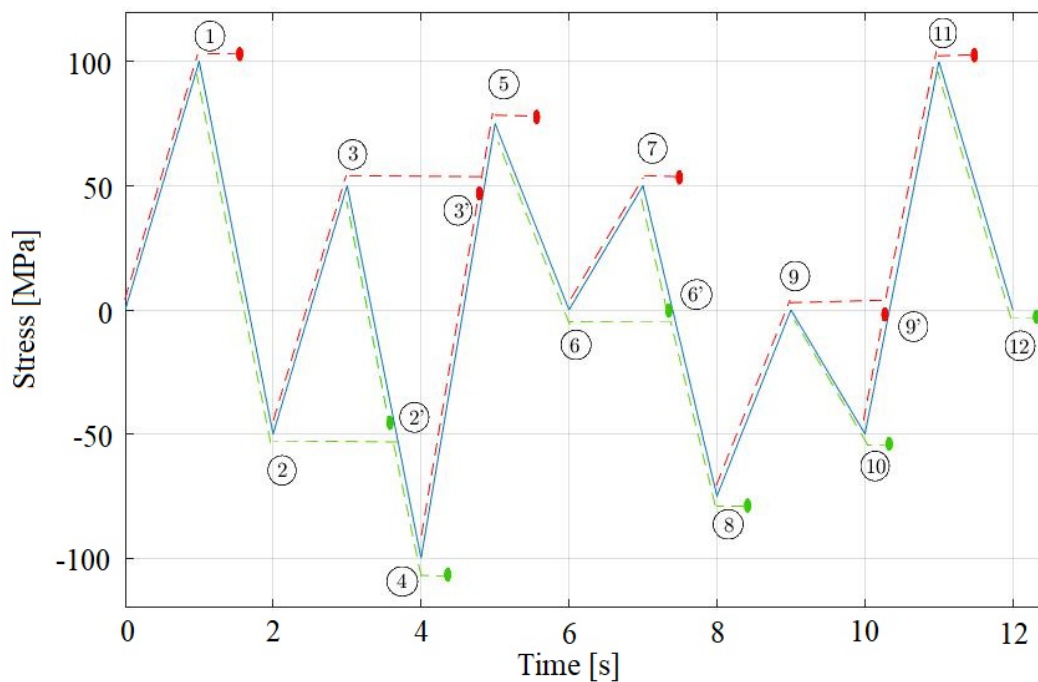


Figure 3.4: Illustration of the Rainflow counting method.

The flow terminates when it reaches the end of the signal (11, 12), when the magnitude of the next peak or valley is lower than the prior (1, 4, 5, 7, 8, 10) or when it merges with a flow that started at another peak or valley (2', 3', 6', 9'). Each terminated flow represents a half cycle of stress ranging from the value at the beginning of the flow to the value at termination. Then, half-cycles of the same magnitude (but opposite sense) are paired to represent a complete cycle of constant amplitude.

3.3 S - N Curve

The S - N curve describes a material's resistance to fatigue and gives the number of cycles to failure, N , versus the stress range, $\Delta\sigma$, with a 97.7 % of survival. The S - N curve is expressed by Equation 3.4 (DNVGL 2016).

$$\log N = \log \bar{a} - m \log \left(\Delta\sigma \left(\frac{t}{t_{ref}} \right)^k \right) \quad (3.4)$$

Here m is the negative slope on the S - N curve, $\log \bar{a}$ is the intercept of the $\log N$ axis, t is the thickness of the member, t_{ref} is the reference thickness and k is the thickness exponent. For members of thickness less than the reference thickness, t is set equal to t_{ref} .

3.4 Palmgren-Miner Sum

The fatigue damage, D_f , from a stress history, can be calculated according to the Palmgren-Miner sum, given by Equation 3.5 (DNVGL 2016).

$$D_f = \sum_{i=1}^l \frac{n_i}{N_i} \quad (3.5)$$

Here l is the total number of stress ranges counted, n_i is the number of cycles occurring of stress range i and N_i is the number of cycles of stress range i that the structure can endure before fracture. When $D_f \geq 1$, fatigue failure will occur.

The total fatigue damage, $D_{f,tot}$ is calculated from the fatigue damage of each occurring stress history and the corresponding probability of occurrence. Thus, the total fatigue damage becomes

$$D_{f,tot} = \sum_{i=1}^j D_{f,i} P_i \quad (3.6)$$

where $D_{f,i}$ is the cumulative fatigue damage from stress history i and P_i is the probability for stress history i to occur. j represents the total number of stress histories.

The design fatigue damage is obtained by multiplying the predicted total fatigue damage, $D_{f,tot}$, by a *design fatigue factor* (DFF) (DNVGL 2016).

Finally, the fatigue lifetime is given as the inverse of the fatigue damage.

Chapter 4

Foundation Stiffness and Damping

The foundation modeling affects the fundamental frequency of the support structure and contributes to the global damping. A realistic model for the foundation response is therefore essential for better fatigue life assessments (Beuckelaers 2015). To avoid resonance effects, it is important that the foundation modeling accurately predicts the fundamental frequency of the structure. Additionally, the damping contribute to energy dissipation, and is therefore important to account for to achieve a better optimization potential. Natural frequency and damping are therefore two very important design considerations of monopile-based OWTs, and will therefore be described in this chapter.

4.1 Natural Frequency

The dynamic response of OWTs differs in some important aspects from other offshore constructions with similar substructures. In addition to the environmental loads from wind and waves, OWTs are also exposed to mechanical loads from the turbine itself. Mass and aerodynamic imbalance of the operating rotor cause vibrations at the hub level, with a load frequency equal to the rotational frequency of the rotor, 1P. As OWTs operate at various rotational speeds, 1P corresponds to a frequency band, ranging from the cut-in to the rated frequency of the rotor. When the rotor is operating, the tower experience vibrations at the blade-passing frequency (2P or 3P for two- or three-bladed turbines respectively), caused by the blade shadowing effect on the tower. The magnitude of 2P and 3P equals two and three times the rotational frequency, 1P, respectively (László Arany et al. 2014).

In designing an OWT structure, it is important to ensure that its fundamental frequency do not coincide with the excitation frequencies of the environmental and mechanical loads, to limit resonance effects on the structure (Zaaijer 2006). Figure 4.1 illustrates typical power spectral density (PSD) plots of the relevant excitation frequencies of the loads on OWTs. Here, 1P and 3P, correspond to the NREL 5 MW turbine, with a cut-in speed of

6.9 rpm (0.115 Hz), and a rated speed of 12.1 rpm (0.202 Hz) (Jason Jonkman and Musial 2010). Note that the different spectra are fitted to the same plot in Figure 4.1 without accounting for unit differences. The plot is purely for demonstrating, and the spectral magnitudes are not relevant.

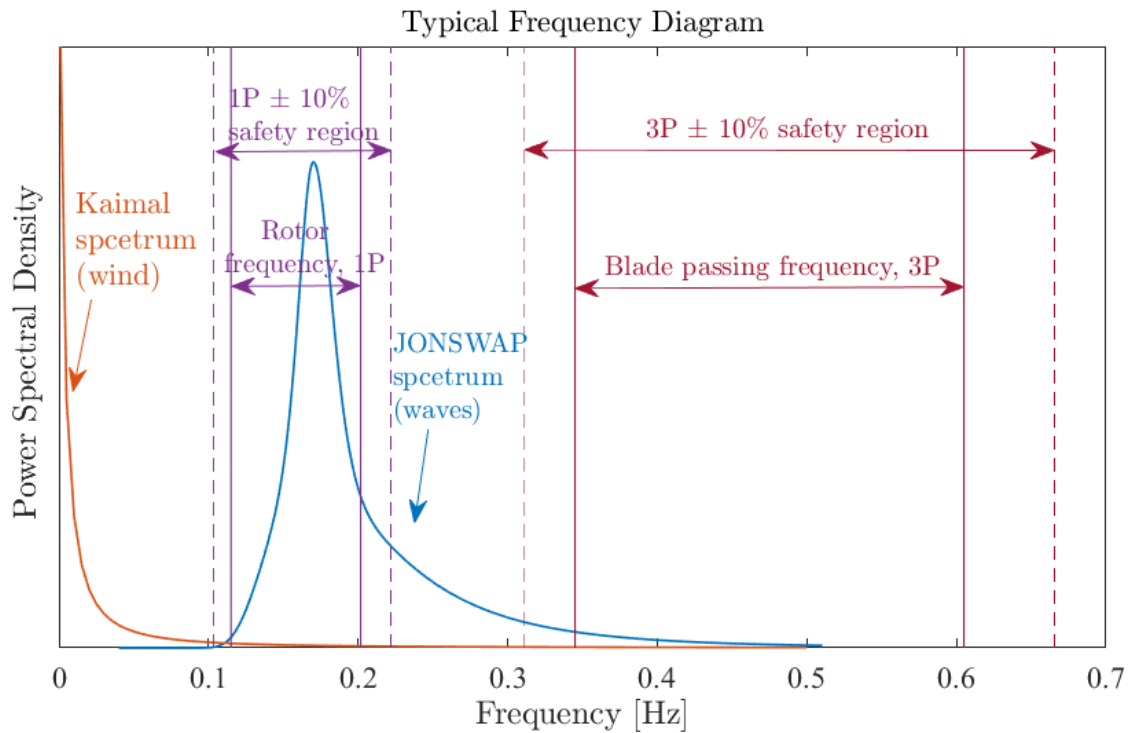


Figure 4.1: Typical frequency spectra of environmental and mechanical loading on a three-bladed OWT. The 1P and 3P frequencies correspond to the NREL 5MW turbine.

DNV suggests wind turbine structures to be designed such that their first tower-bending frequencies lies outside of the frequency range of 1P and 3P, within a safety region of $\pm 10\%$ (DNV/Risø 2002), as indicated in Figure 4.1. This leaves 3 design possibilities:

1. *soft-soft* design. The fundamental frequency of the structure lies below the lower limit of the 1P frequency range. This design is difficult to obtain for grounded structures, as the structures would be very flexible (László Arany et al. 2014).
2. *soft-stiff* design. For this design, the fundamental frequency of the OWT structure lies between the upper limit of the 1P range and the lower limit of the 3P range. This is the most common design for monopile OWTs today (Arshad and O’Kelly 2016).
3. *stiff-stiff* design. The fundamental frequency of the structure lies above the upper limit of the 3P range. This is possibly the “safest” design choice from a dynamic point of view. However, this design would involve greater material, transportational and installational costs (László Arany et al. 2014).

A soft-stiff design is by far the most common for monopile OWTs today, and as the industry focus greatly on cost reductions, it is safe to assume that the soft-stiff design will remain the most favoured design for future applications (László Arany et al. 2014). From Figure 4.1, it becomes clear that to satisfy this design, the first natural frequencies has to be fitted in a very narrow band. Accurate predictions of a structure's fundamental frequency is therefore highly important in predicting the lifetime of the structure.

4.2 Damping

The main sources of damping on OWTs are: aerodynamic damping, soil damping, hydrodynamic damping and structural damping. Additionally, some turbines have installed tuned mass dampers (Carswell et al. 2015). Damping dissipates energy from the system, thus reducing the amplification of the loads, and consequently the fatigue damage on the structure.

The most significant source of damping on OWTs, in the fore-aft direction, during power production, is aerodynamic damping. As the blades respond to the relative wind speed from the tower-top motion, the aerodynamic forces on the structure decreases. The effects of aerodynamic damping is, however, negligible in the side-to-side direction, or in the fore-aft direction of a parked turbine. In those cases other sources of damping will dominate (Carswell et al. 2015).

Many soil-structure interaction models fail to describe soil damping, and the effect of neglecting it in fatigue calculations will be investigated in this thesis. Soil damping will therefore briefly be described in the following.

Soil Damping

Compared to other types of damping, soil damping is the least studied, and the one that shows the biggest difference between theoretical and measured results (Carswell et al. 2015). Although not providing any recommended practice, Det Norske Veritas require soil-damping to be considered in the design phase of OWTs (DNV 2014).

There are two types of soil damping; *radiation damping* and *hysteretic damping*. Radiation damping describes dissipation of energy through the radiation of waves spreading through the soil, and is negligible for frequencies below 1Hz (Andersen 2010). The largest amplifications for monopile-based OWTs occur at the structures' fundamental frequency, which, unless designed by a stiff - stiff design, lies well below 1Hz. Radiation damping can therefore, with good accuracy, be disregarded in the assessment of monopile-based OWTs.

Hysteretic damping occurs during cyclic loading, and represents the energy dissipated

through plastic deformations. The magnitude of the energy dissipation is dependent on the strain level in the soil as Figure 4.2 illustrates. During loading, the soil exhibits a non-linear behaviour, resulting in a non-linear foundation response (0-1). Upon unloading, the soil initially behaves elastic, resulting in a stiffer pile response prior to the unloading (1-2). As the load on the soil is reversed to larger magnitudes, plastic deformations starts occurring in the reversed direction (2-3). Upon reloading (3-5), a similar behaviour is obtained. As the structure is loaded and unloaded, the load-displacement curve, thus, form a *hysteretic loop*. The area under the hysteretic loop (1-2-3-4-1) correspond to the dissipated energy of the deformation cycle (Aasen et al. 2017).

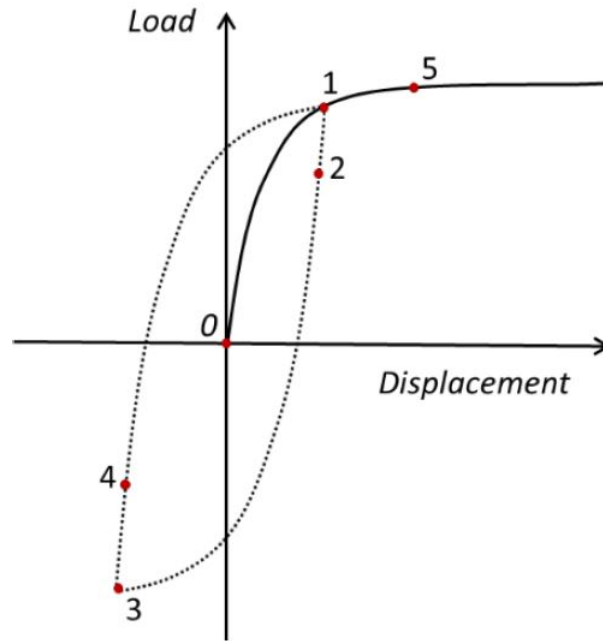


Figure 4.2: Example of hysteretic a loop in the foundation's load - displacement response (Aasen et al. 2017).

4.2.1 Procedure of Damping Estimation

The total damping contribution of the first bending mode of a monopile-based OWT, can be obtained from the logarithmic decrement of the structure under free vibration, given by Damgaard et al. (2012) as

$$\xi = \frac{1}{n} \ln \frac{A_0}{A_n} \quad (4.1)$$

where A_0 and A_n corresponds to the amplitude of two successive peaks, separated by the time interval nT_p , where T_p is the period between two peaks and n is the number of peaks between A_0 and A_n . This is illustrated in Figure 4.3.

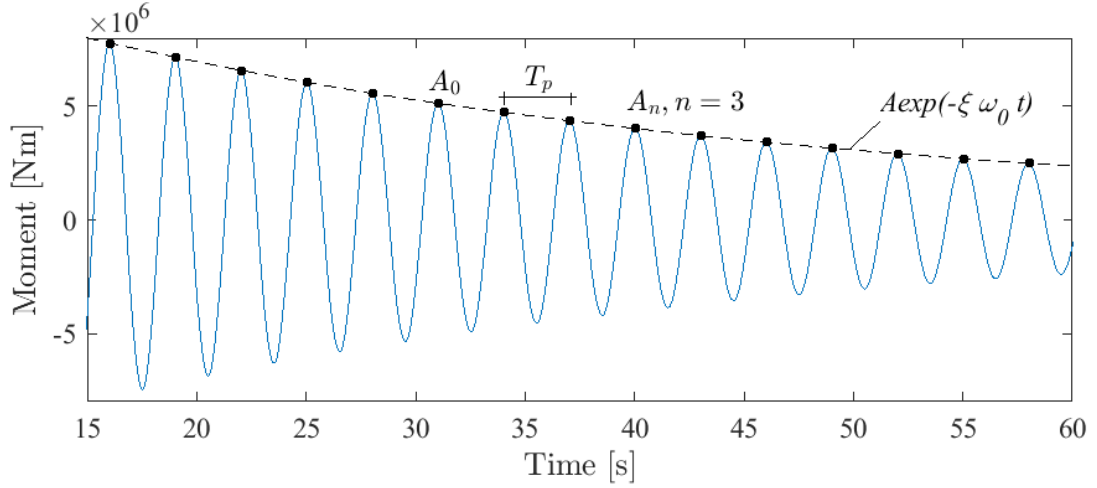


Figure 4.3: Damping estimation through logarithmic decrement of the moment amplitudes under free vibration.

Furthermore, the damping ratio of the first mode can be estimated in terms of the logarithmic decrement from Equation 4.2 (Damgaard et al. 2012).

$$\zeta_{tot} = \frac{1}{\sqrt{1 + \left(\frac{2\pi}{\xi}\right)^2}} \quad (4.2)$$

The structural contribution to each modal damping ratio can be estimated through *Rayleigh damping*. In that sense, the structural damping ratio of mode m is given by Equation 4.3 (Alipour and Zareian 2008)

$$\zeta_{m,struct} = \frac{\alpha}{2} \frac{1}{\omega_m} + \frac{\beta}{2} \omega_m \quad (4.3)$$

where the damping coefficients α and β , are scalars that can be determined from specific modal damping ratios to the i -th and j -th mode according to Equation 4.4 (Alipour and Zareian 2008).

$$\frac{1}{2} \begin{bmatrix} \frac{1}{\omega_i} & \omega_i \\ \frac{1}{\omega_j} & \omega_j \end{bmatrix} \begin{Bmatrix} \alpha \\ \beta \end{Bmatrix} = \begin{Bmatrix} \zeta_{i,struct} \\ \zeta_{j,struct} \end{Bmatrix} \quad (4.4)$$

The contribution of the soil damping on the total damping ratio for a bottom-mounted OWT can be estimated by a subtraction of the remaining contributions, as in Equation 4.5 (Shirzadeh et al. 2013):

$$\zeta_{soil} = \zeta_{tot} - \zeta_{struct} - \zeta_{aero} - \zeta_{hydro} - \zeta_{mass.damp} \quad (4.5)$$

Chapter 5

Soil - Structure Interaction

The accuracy of dynamic analyses of OWTs highly depends on how realistic the model of the entire OWT is. A shortcoming in modeling monopile OWT foundations relates to their flexibility and the ability to correctly represent the dynamic response, due to soil-structure interaction (SSI). To understand SSI, a basic understanding of how soil react to loading is necessary. This chapter will therefore give a brief explanation of some basic soil mechanics and then proceed to describe SSI related to the two foundation models studied in this thesis.

5.1 Soil Mechanics

5.1.1 Behaviour

In contrast to materials that can, with good accuracy, be assumed linear-elastic-perfectly-plastic (such as steel), soils often behaves strongly non-linear, due to the development of plastic deformations. Consequently, upon loading and unloading, soils exhibit irreversible plastic deformations, even at low stress levels (Verruijt 2006). Soil behaviour upon loading is highly dependent on the initial stress state, which is commonly not uniform, and varies from different sites.

When soils are compressed, the forces between the soil particles increase, thus leading to an increased stiffness and strength of the soil. In contrast, soils under shear becomes softer (Verruijt 2011).

5.1.2 Strength

The *strength* of the soil is the limit to which the soil no longer can transfer stresses. A commonly applied expression of a soil's shear strength, τ_{max} , is given by the *Mohr-*

Coulomb criterion as in Equation 5.1 (Verruijt 2006).

$$\tau_{max} = c + \sigma \tan \phi \quad (5.1)$$

Here c is the cohesion, ϕ is the friction angle and σ is the normal stress. Figure 5.1 illustrates the relation, where the half-circles correspond to stress circles of the principal stresses. The material fails when one circle touches the yield surface (straight line), corresponding to the stress level at which the material yield.

For untrained analyses of clay, it is commonly assumed that $\phi = 0$ and the cohesion becomes equal to the *undrained shear strength* of the soil, s_u (*PLAXIS Material Models Manual* 2017).

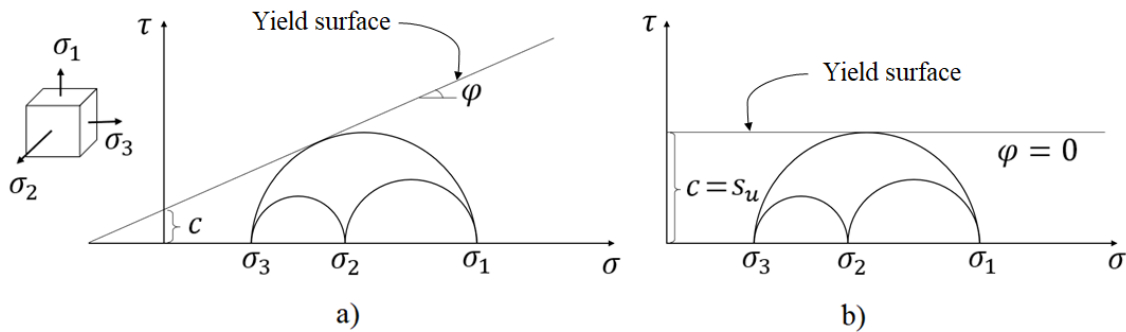


Figure 5.1: Mohr-Coulomb yield criteria for a) drained and b) undrained conditions.

5.2 Soil - Structure Interaction Models

Soil-structure interaction (SSI) refers to the process where the dynamic response of a structure is influenced by the surrounding soil, and opposite. Often, SSI is neglected from OWT design, and a fixed-base is assumed at the mudline. Consequently, it is assumed that the soil is infinitely stiff and strong. However, when accounting for SSI, the natural frequencies of the structure will be lower than for the fixed-base assumption at the mudline, as the SSI provides more flexibility to the system and it becomes softer. The equivalent natural frequency for a Single Degree of Freedom (SDOF) system, when accounting for SSI, becomes as given in Equation 5.2 (Kramer 1996)

$$\frac{1}{\omega_{eq}^2} = \frac{1}{\omega_0^2} + \frac{1}{\omega_u^2} + \frac{1}{\omega_r^2} \quad (5.2)$$

where ω_0 is the fixed-base natural frequency, and ω_u and ω_r are the foundation's translational and rocking natural frequencies, respectively.

Several different ways of modeling the SSI of laterally loaded piles in OWT application

has been suggested, both by elastic and non-linear models. Among the non-linear models, the $p - y$ method is the most commonly applied (Mardfekri et al. 2013). This thesis compares the conventional soil modeling with $p - y$ curves, to a newly developed macro-element model based on finite element (FE) data. This section will therefore focus on giving a brief description of the two models in discussion.

5.2.1 $p - y$ Curves

The industry practice today for predicting the response of laterally loaded piles in offshore applications, is through the use of $p - y$ curves (Byrne et al. 2015). The $p - y$ method defines a non-linear, depth dependent, relationship between the lateral displacement, y , and the soil reaction, p . The pile is typically modeled as an elastic beam, whereas the soil reaction is described by non-linear horizontal springs distributed along the depth of the pile. Each spring has specific properties defined from the $p - y$ curves (Mardfekri et al. 2013) Figure 5.2 provides a visualization of the concept.

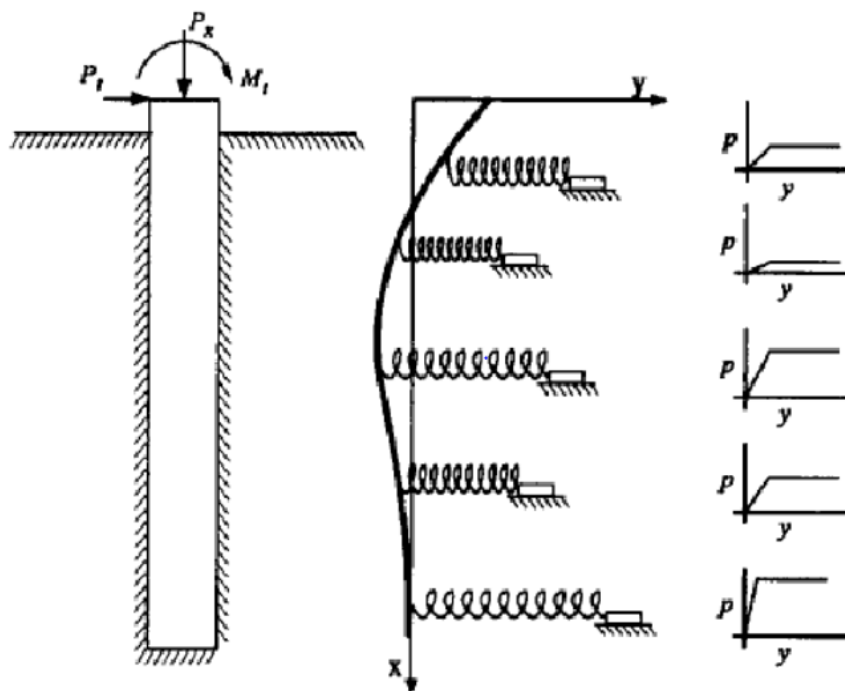


Figure 5.2: Illustration of a set of distributed springs along the pile, with corresponding $p - y$ curves (Perumalsamy et al. 2015).

The first general formulation of $p - y$ curves were developed by Matlock (1970) for soft clay, and later by Reese et al. (1974) and Reese et al. (1975) for sand and stiff clay, respectively. These curves were calibrated based on field tests on small-diameter piles with a large length to diameter ratio, and have showed to be applicable, with good accuracy, for estimations on the slender piles used in the oil and gas industry (Arshad and O'Kelly

2016).

API p – y Curves

The *American Petroleum Institute* (API) recommends in its guidelines p – y curves, which depend upon soil parameters and depth. The API soft clay p – y curves are discretised versions of the p – y curves provided by Matlock (1970). For clay, the ultimate unit bearing capacity, $p_u D$, is given by API (2011) as

$$p_u D = \begin{cases} 3s_u D + \gamma' z D + J s_u z & \text{for } z < z_R \\ 9s_u D & \text{for } z \geq z_R \end{cases} \quad (5.3)$$

where

$$z_R = \frac{6D}{\gamma' D / s_u + J} \quad (5.4)$$

Here s_u is the undrained shear strength, D is the outer diameter of the pile, z is the depth below mudline, γ' is the submerged soil unit weight and J is an empirical constant determined by field tests. Tabulated values for p/p_u and y/y_c , where $y_c = 2.5\epsilon_{50}D$ and ϵ_{50} describes the strain at 50% the maximum deviator stress, define the points on the curve. These values are provided in Table 5.1. Between the points, linear interpolation defines the curve. Figure 5.3 plots the characteristic shape of the API p – y curve for clay.

Table 5.1: API p – y data for short-term static loading of piles in clay.

p/p_u	0.00	0.23	0.33	0.50	0.72	1.00	1.00
y/y_c	0.0	0.1	0.3	1.0	3.0	8.0	∞

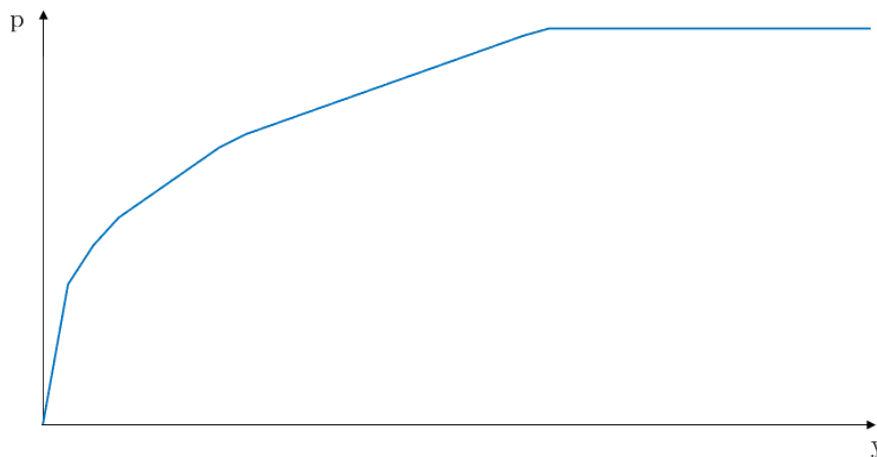


Figure 5.3: Shape of a typical API p – y curve for laterally loaded piles in clay.

Similarly, API has provided $p - y$ relations for laterally loaded piles in sand. The reader is referred to ISO19901-4:2003 by API (2011) for a detailed description on this. For information on other suggested $p - y$ curves for soft and stiff clay, the reader is referred to Matlock (1970) and Reese et al. (1975), respectively.

Extracting Curves from FEA

Alternatively to the semi-empirical formulae proposed by API, $p - y$ curves can be extracted from finite element analyses. This is expected to give a more accurate description of the pile response, however, it demands more work (Mardfekri et al. 2013).

The soil reaction, p , can be found from integrating the stresses acting around the circumference of the pile (Wang and Lymon C. Reese 1993), as illustrated in Figure 5.4.

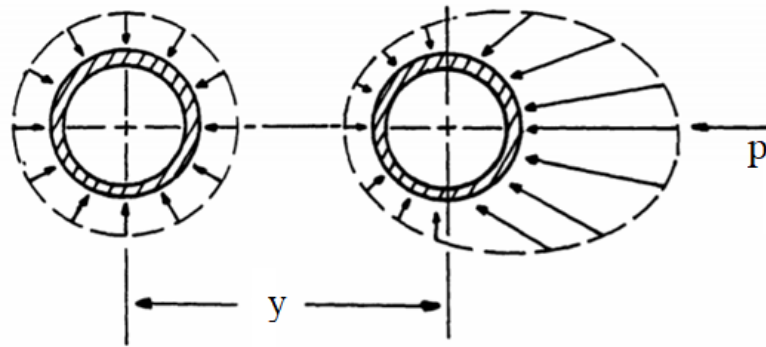


Figure 5.4: Stress around a laterally loaded pile (Wang and Lymon C. Reese 1993).

Alternatively, estimates to the in the $p - y$ formulation can be found through a relation to the bending moment along the pile length, by Equations 5.5 and 5.6.

$$p = \frac{d^2}{dz^2} M \quad (5.5)$$

$$y = \int \int \frac{M}{E_p I_p} dz dz \quad (5.6)$$

Limitations of $p - y$ Curves

$p - y$ curves are in general modeled as non-linear elastic. This entails that they follow the same load - displacement path in loading and unloading, as illustrated in Figure 5.5. Hence, they cannot reproduce the soil damping when applied in foundation modeling (Beuckelaers 2015).

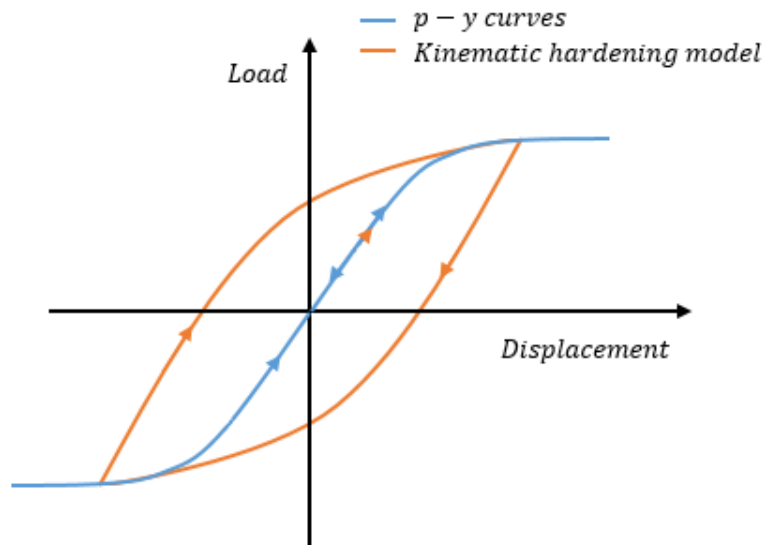


Figure 5.5: $p - y$ path vs kinematic hardening path.

In contrast, as seen by the figure, a model that is applying a kinematic hardening formulation will be able to account for foundation damping.

5.2.2 Macro-Element Model

The second foundation model studied in this thesis was developed by PhD candidate Ana M. Page at NTNU/NGI as part of the REDWIN project. The brief description of the model provided in this section is based on her documentation. The reader is referred to (Page et al. 2018) for a more detailed description of the model.

The model bases on a *macro-element* approach, replacing the entire pile-soil foundation system by a single element at the seabed. The macro-element describes the response of the foundation and the surrounding soil through a relation between forces and displacements at this point, determined by numerical analyses. The model builds upon elasto-plastic theory, and to understand the concepts behind the model formulation, the three main components to plasticity theory; *yield criterion*, *flow rule* and *hardening rule*, will be explained in a general sense. It is noted that the displacement increment can be obtained from superposition of an elastic component and a plastic component as given by Equation 5.7.

$$d\mathbf{v} = d\mathbf{v}^e + d\mathbf{v}^p \quad (5.7)$$

Yield Criterion

A body under loading will initially be deformed elastically, and the displacements will be reversible. With an increasing load level, the body will eventually reach a limit where irreversible (plastic) deformations starts occurring. This limit is known as the yield limit. The yield function, f , describes when a material yields, and the yield criterion, $f = 0$, defines a surface in the stress space that encloses the elastic region (Hopperstad and Brøvik 2015). There are three possible scenarios for the yield function:

- $f < 0$ The load level is in the elastic domain. Only elastic deformations will occur.
- $f = 0$ The load level is at the yield surface. Elasto-plastic deformations will occur.
- $f > 0$ Inadmissible.

This is illustrated in Figure 5.6 in the stress space.

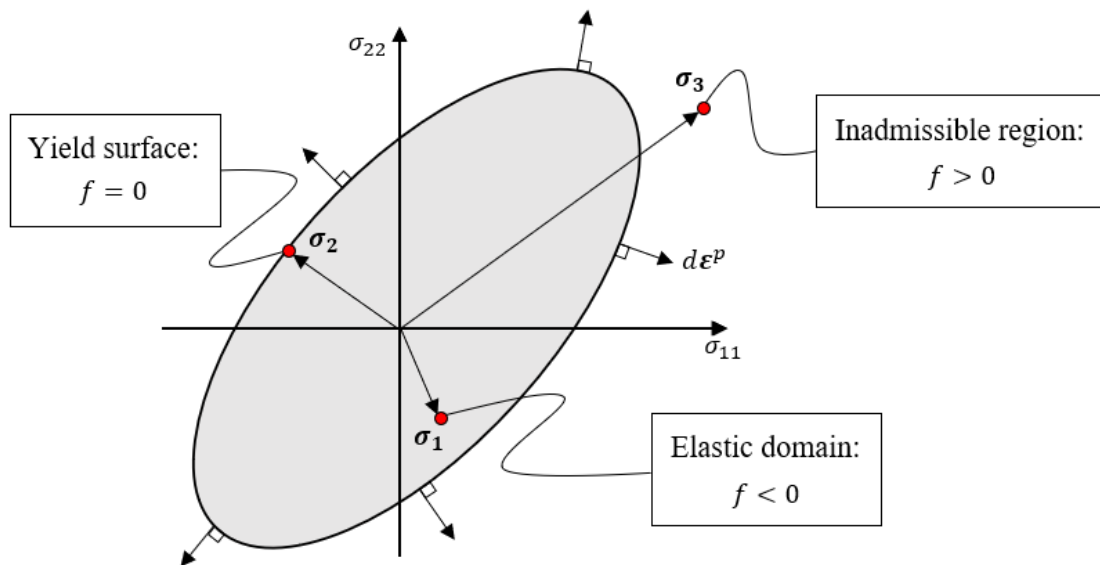


Figure 5.6: Illustration of a yield surface including vectors of plastic flow. The figure is a modified version of one provided by Hopperstad and Børvik (2015).

Flow Rule

The direction and magnitude of plastic flow is described by the flow rule, which in general is given by Equation 5.8 (Hopperstad and Brøvik 2015).

$$d\boldsymbol{\varepsilon}^p = d\lambda \frac{\partial g}{\partial \boldsymbol{\sigma}} \quad (5.8)$$

Or in terms of displacements as

$$d\mathbf{v}^p = d\lambda \frac{\partial g}{\partial \mathbf{t}} \quad (5.9)$$

where \mathbf{t} is the load vector and $g \geq 0$ is the plastic potential function. The direction of the plastic displacement increment vector is always outward normal to g . The plastic multiplier, $d\lambda$, is a non-negative scalar that defines the size of the plastic displacement increment.

By assuming that the plastic potential function, g , is defined by the yield function, f , we adapt the *associated flow rule* given by

$$d\mathbf{v}^p = d\lambda \frac{\partial f}{\partial \mathbf{t}} \quad (5.10)$$

The associated flow rule implies that the plastic displacement increment vector, $d\mathbf{v}^p$, at any point, is directed outward normal to the yield surface at this point. Consequently, the shape of the yield surface not only determines the stress state of yielding, but also the direction of plastic flow (Hopperstad and Brøvik 2015).

Hardening rule

In addition to being dependent on the load level, the yield function also depends on the work-hardening of the material. The two most common hardening rules are *isotropic hardening* and *kinematic hardening*. In isotropic hardening, plastic deformation will result in an increase of the elastic region in the stress space, as illustrated in Figure 5.7a. The yield surface keeps its shape, while the size increases. In kinematic hardening, the elastic domain is rigidly translated in the stress space, as Figure 5.7b shows. The yield surface keeps its shape and size, and the surface is rigidly translated in the stress space.

In describing work-hardening under cyclic loading, kinematic hardening is the most accurate as it accounts for the *Bauschinger effect*. The Bauschinger effect describes directional hardening, where the strength increases more in the direction of plastic loading, as can be seen from Figure 5.7b. If a material is loaded until a stress magnitude σ_A , then reloaded to yielding in the reverse direction, σ_B , we typically obtain that $|\sigma_B| < |\sigma_A|$ (Hopperstad and Brøvik 2015).

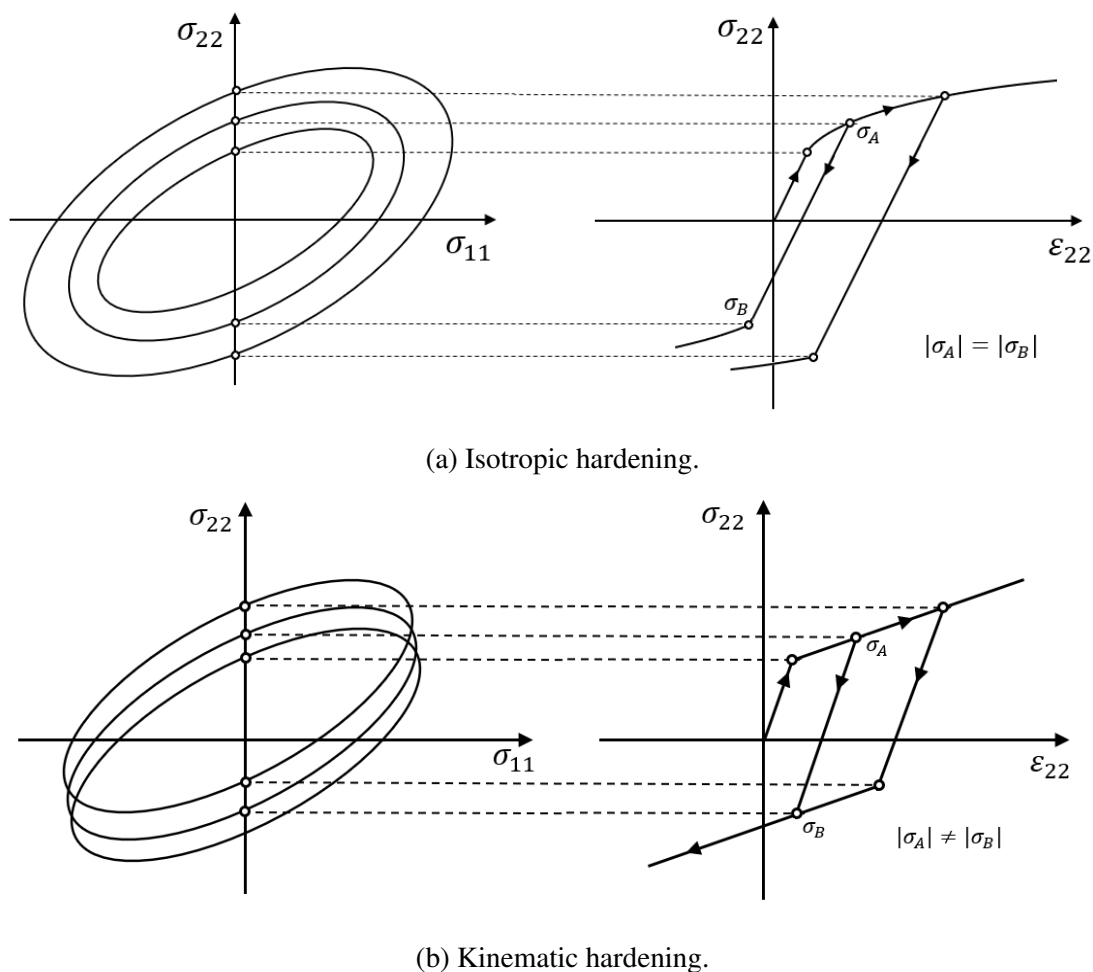


Figure 5.7: Illustration of different hardening laws. The figures are a modified versions of ones provided by Hopperstad and Børvik(2015)

The macro-element model uses a multi-surface plasticity formulation. This implies that the model utilizes several yield surfaces $f_i = f(\mathbf{t}, \boldsymbol{\alpha}_i)$, where \mathbf{t} describes the loading state and $\boldsymbol{\alpha}_i$ describes the position of the centre of the ellipse defining surface i , as indicated in the load space in Figure 5.8.

The formulation of the yield surfaces in the loading space is adopted from the observation that contours of constant plastic work takes an elliptical shape in the loading space. The plastic work is given by

$$W^p = \int_0^{u^p} H du^p + \int_0^{\theta^p} M d\theta^p \quad (5.11)$$

where H and M relates to the horizontal load and bending moment, respectively. The inner surface corresponds to the yield surface of the material, and the response will be purely elastic when the load level is within this range. The outer surface corresponds to the failure surface of the material, whereupon a higher load level will lead to failure. The remaining surfaces are loading surfaces of constant plastic work.

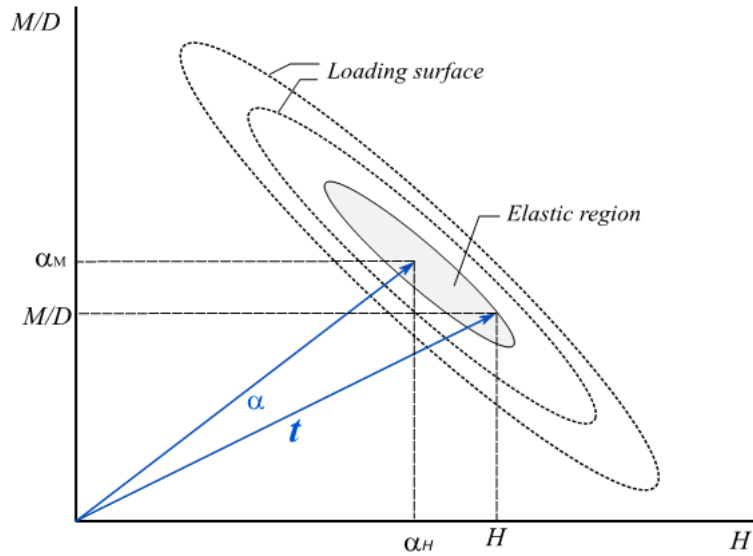


Figure 5.8: Yield surfaces used by the macro-element (Page et al. 2018).

The total direction of the plastic deformation increment is defined by a summation of the flow rule for each surface, i , as Equation 5.12 indicate.

$$d\mathbf{v}^p = \sum_{i=1}^j d\mathbf{v}_i^p = \sum_{i=1}^j d\lambda_i \frac{\partial f_i}{\partial \mathbf{t}} \quad (5.12)$$

The translations of the surfaces in the load space are described by a purely kinematic hardening rule, where $d\boldsymbol{\alpha}_i$ defines the translation.

A visualization of the macro-element's behaviour is provided in Figure 5.9. As it is loaded from O to A, the load path remain within the innermost surface, and only elastic displacements occur. At position A, the yield criterion of the innermost surface is violated, and $f_1 = 0$ is obtained. As $f > 0$ is inadmissible, the load path from A to B, will drag the surfaces, and plastic displacements will occur. In further loading and unloading, similar behaviour occurs, and a piecewise linear load-displacement response is obtained.

Calibration of the Macro-Element

Two inputs are required for the calibration of the macro-element model.

1. The coefficients for the elastic stiffness matrix. This input predicts the elastic response of the model.
2. Non-linear load - displacement curves. These curves defines the yield surfaces' shape and size as well as the hardening law.

The inputs can be obtained from finite element analyses (Page et al. 2018).

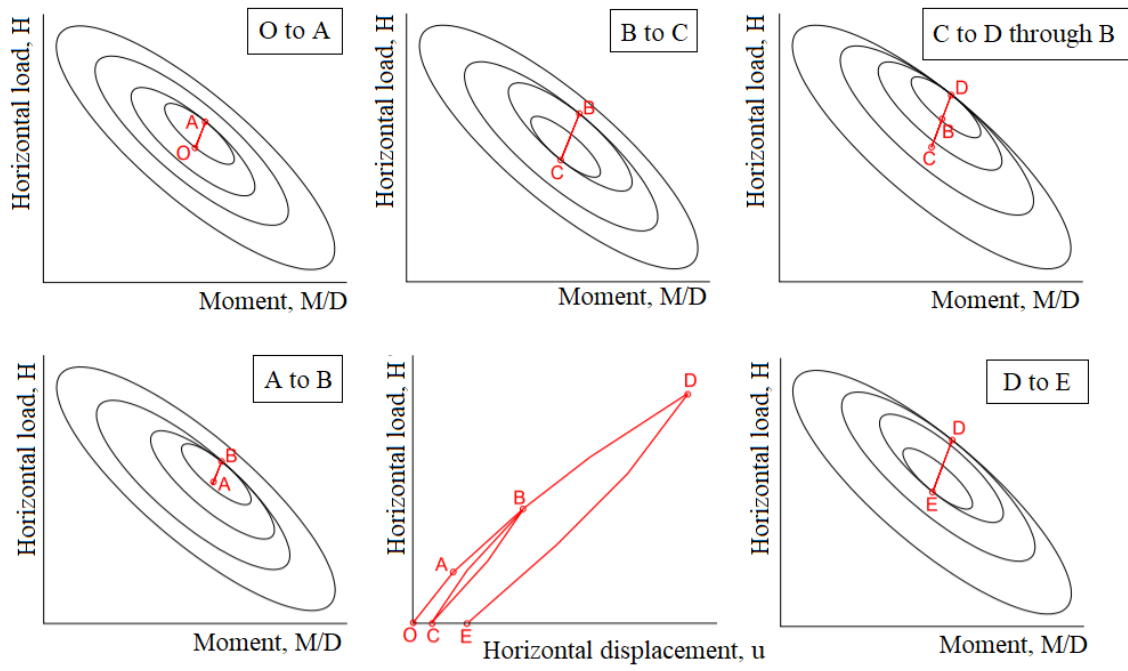


Figure 5.9: Illustration of the behaviour of the macro-element (Page et al. 2018).

Chapter 6

Finite Element Modeling

A reliable approach in modeling SSI, particularly when accounting for the non-linear behaviour for the soil and the interface between the pile and the soil, is through the finite element method (FEM) (Mardfekri et al. 2013). In this study, a FE model was used to calibrate the macro-element, as well as to obtain FEA $p - y$ curves to be applied in the fatigue calculations. Various FE programs exist, however the selected program for this study was Abaqus/CAE for modeling and post-processing, and Abaqus/Standard for running the analyses. Abaqus includes the possibility to apply a geostatic step, accounting for the initial stress state of the soil, thus increasing the reliability of the model (Mardfekri et al. 2013). This chapter describes the Abaqus model and its verification.

6.1 Coordinate System

The global coordinate system for the Abaqus model had its origin at the mudline, in the cross-sectional center of the pile. In consistency with the coordinate system used in 3DFloat (see Chapter 7), the axes were such that the loading was applied in the x -direction, with the y -axis perpendicular to the x -axis, and the z -axis pointing positively upwards. Figure 6.1 indicates the coordinate system for the Abaqus model.

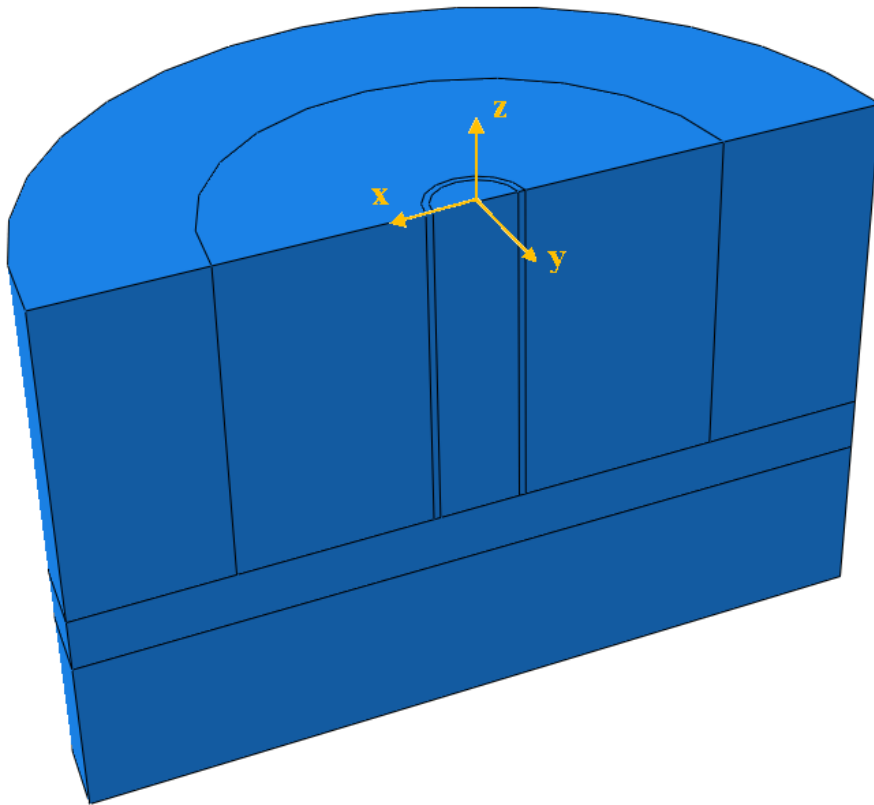


Figure 6.1: Coordinate system for the Abaqus model.

6.2 Initial Modeling

6.2.1 Pile Modeling

Before modeling the whole problem of the pile submerged in soil, an initial modeling of the monopile alone was performed, to verify its modeling. The pile was modeled as a cantilevered cylinder, with an applied unit load at the free end. The geometrical and mechanical properties of the pile are listed in Table 6.1.

Table 6.1: Pile properties for the initial geometry.

Mechanical properties		Geometrical properties		
Young's modulus (GPa)	Poisson ratio (-)	Diameter (m)	Thickness (m)	Length (m)
210	0.3	6	0.06	24

Choice of Pile Element Type

Using shell elements as compared to solid elements is beneficial, as they may result in less computational costs due to the lower number of degrees of freedom (DOFs). However, their usefulness is limited to really thin members, and their validity to this problem was therefore investigated. A comparison of the analytical load response of a cantilevered cylinder was compared to the FE model using shell elements, for verification. The resulting moments and displacements are shown in Figure 6.2.

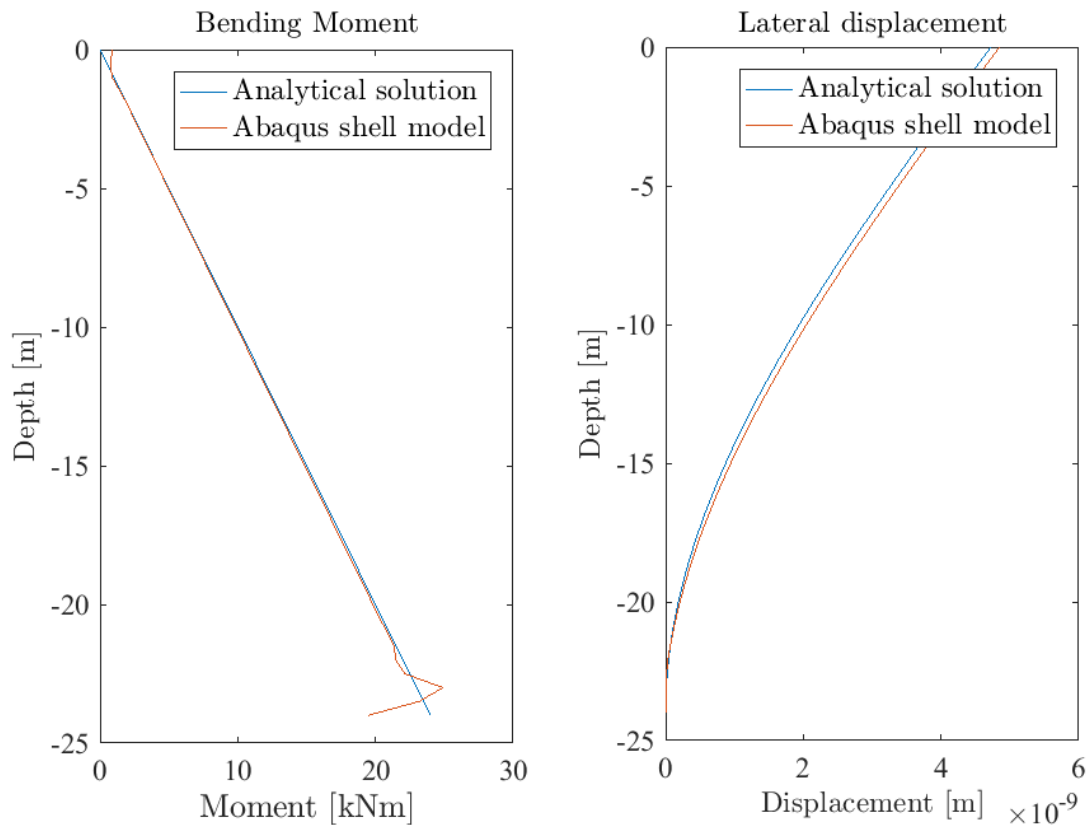


Figure 6.2: Analytical solution vs. FE model using shell elements.

The FE results differ somewhat from the analytical solution, however this difference is insignificantly small, and is expected to reduce with a finer mesh. As the figure indicate, shell elements are useful for the geometry of this problem.

Symmetry

Since the geometry and loads are symmetric, it is possible to model half of the geometry and the loads, and for computational savings, it is beneficial to utilize the symmetry of the problem. The model was therefore simplified to only consist of half the cylinder. Symmetry boundary conditions (BCs) were applied to the cylinder, as illustrated in Figure 6.3.

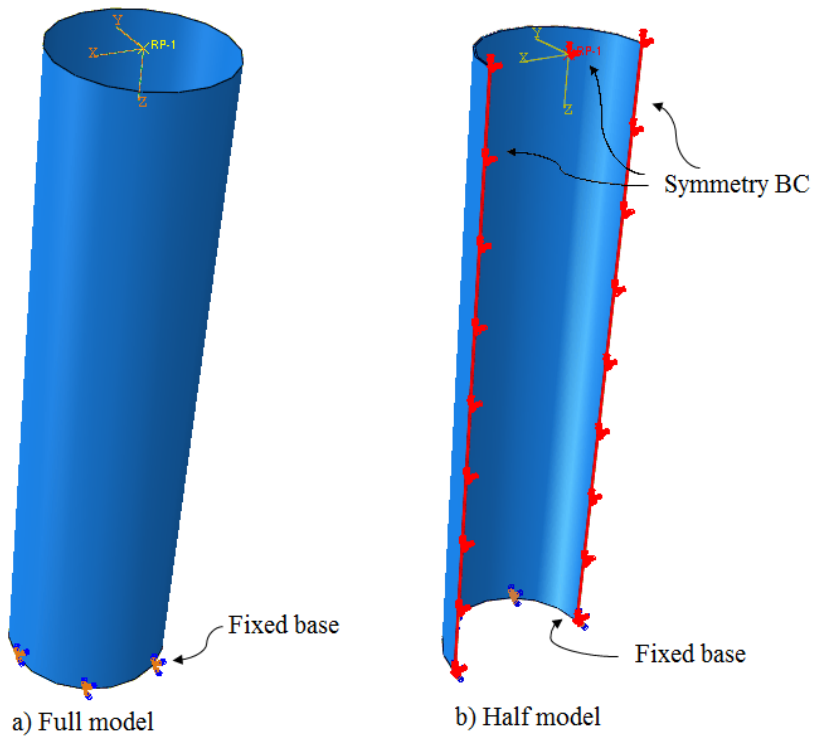


Figure 6.3: Symmetry boundary conditions.

The usefulness of the symmetry assumption was verified by comparing the the resulting moments and displacements from the full- and half model. Figure 6.4 plots the response of the two different ways of modeling.

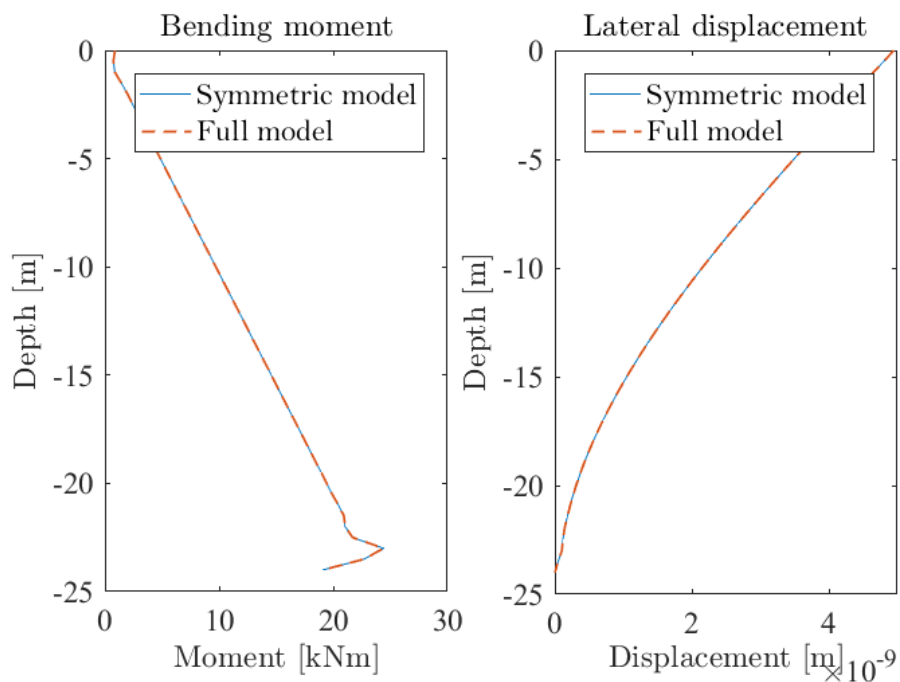


Figure 6.4: Response comparison of symmetric and full model.

The figure confirms that the symmetry boundary conditions is applied correctly, as the results are identical.

6.2.2 Soil Modeling

Choice of Soil Volume

The soil profile used in the Abaqus model was an idealized clay profile selected to give a foundation response similar to the well tested OC3 monopile Phase II (which is based on a sand profile). For more details about the OC3 monopile, the user is referred to Jonkman and Musial (2010).

The idealized clay profile was defined with with a linear increasing value for the undrained shear strength, s_u , and shear modulus, G_{max} , as illustrated in Figure 6.5.

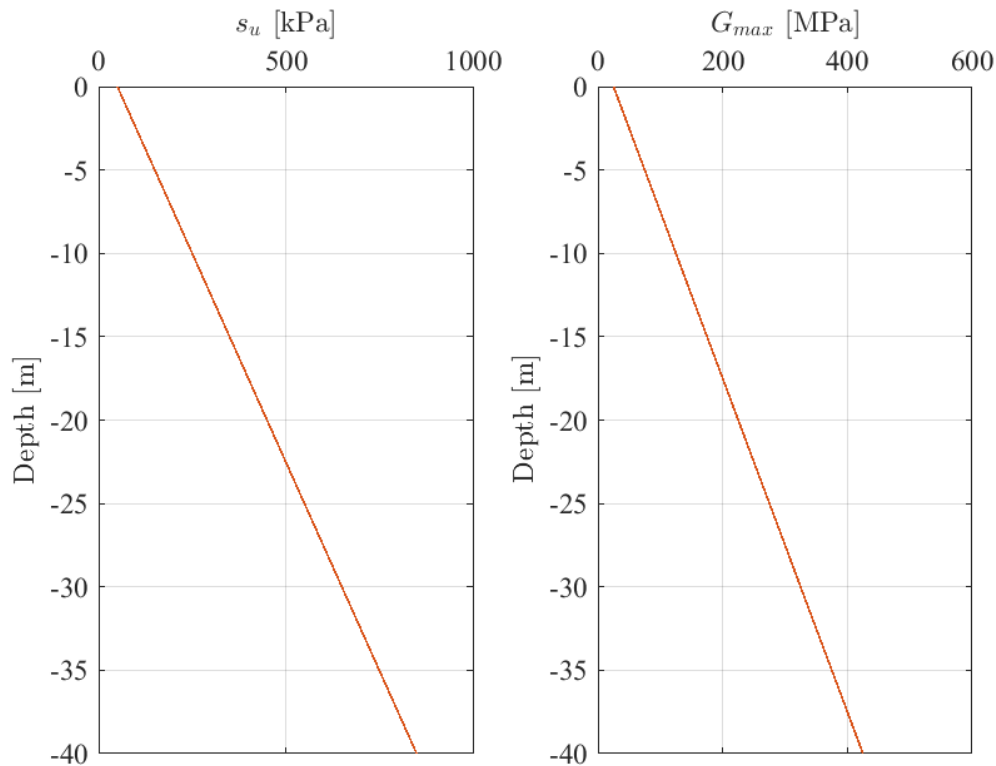


Figure 6.5: Soil profile of the idealized clay model.

To ensure that there was no artificial boundary effects, the size of the soil volume was verified. The soil was initially modeled with a Mohr-Coulomb formulation, as this demanded less computational effort. The variation of s_u and G_{max} with depth was obtained from defining a linearly increasing analytical field with depth, and the values for s_u and G_{max} were specified on this field. The soil parameters applied in the Mohr-Coulomb material formulation in Abaqus is listed in Table 6.2.

Table 6.2: Soil parameters.

γ' (kN/m ³)	$s_{u,top}$ (kN/m ²)	$ds_u dz$ (kN/m ³)	ν_s (-)	G_{max}/s_u (-)	ϕ (deg)	ψ (deg)
10	50	20	0.495	500	0	0

where the parameters refer to:

γ' :	submerged unit weight of the soil
$s_{u,top}$:	undrained shear strength at the mudline
$ds_u dz$:	change of undrained shear strength with depth
ν_s :	Poisson ratio of the soil
G_{max}/s_u :	shear modulus
ϕ :	friction angle
ψ :	dilation angle

and the Young's modulus was obtained form the relation

$$E = 2G(1 + \nu) \quad (6.1)$$

The soil was modeled as a half-cylinder to allow for the use of brick elements, and the pile was embedded in the soil volume by the contact formulation as will be described in Section 6.3.2. The amount of soil volume needed to avoid artificial boundary effects was investigated by selecting various diameters for the soil cylinder. Figure 6.6 plots the comparison of the pile response between using a soil diameter of 10D and 20D, where D represents the outer diameter of the pile. As the figure indicate, it was sufficient to model the soil-cylinder with a diameter of 10D.

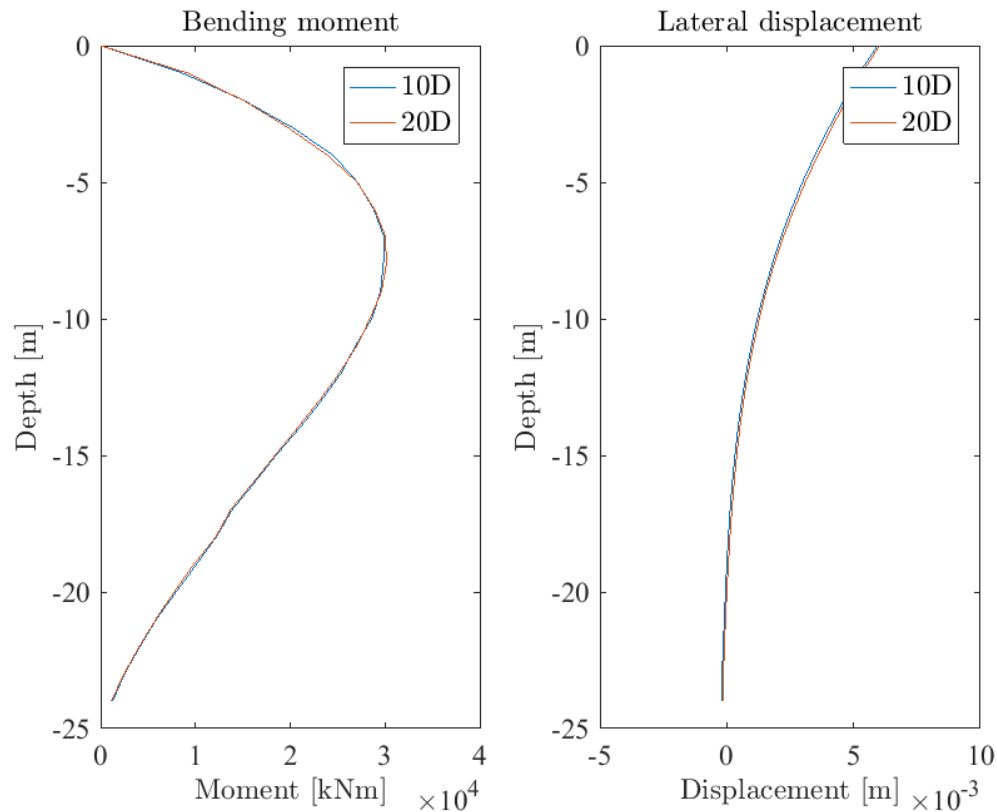


Figure 6.6: Comparison of the lateral displacement and the bending moment due to different sizes of soil volume.

6.3 Final Modeling

6.3.1 Geometry

Soil Model

In the final model, the soil was modeled as a continuum with solid elements. The material formulation, corresponding to the soil profile described in Section 6.2.2, was given through a NGI-ADP model by a UMAT user subroutine. For details on the NGI-ADP, the reader is referred to Grimstad et al. (2012).

The dimensions of the soil was a half-cylinder with diameter $10D$ and length $\frac{5}{3}L_{pile}$.

Pile Model

The pile was modeled as a hollow cylinder with shell elements embedded in the soil. Different geometries were studied, and the various pile properties used are listed in Table 6.3.

Table 6.3: Pile properties for the three geometries.

	Mechanical properties		Geometrical properties		
	Young's modulus (GPa)	Poisson ratio (-)	Diameter (m)	Thickness (m)	Length (m)
Geometry 1	210	0.3	6	0.060	24
Geometry 2	210	0.3	6	0.054	24
Geometry 3	201	0.3	6	0.050	24

6.3.2 Interface Properties

Contact problems often show difficulties in converging, usually because of errors in defining correct interface properties and the mesh at the contact surfaces. When modeling shell elements in contact, there are two common approaches of defining the interface. These were both tested in this study, and will be described briefly in the following.

Contact Formulation

In the contact formulation, the pile and soil are created as two separate parts, where the soil is modeled with an adapted cut for the pile to fit into. The interface between the soil and the pile is defined by contact properties in both the normal and tangential directions to the contact surfaces. The pile is typically selected as the master surface, and the soil as the slave surface. It is important to ensure that the slave surface has the finest mesh to avoid penetration by the master surface. The benefits of this method is the possibility to define the interface properties directly in the contact definition. However, when modeling a monopile embedded in the soil, the number of contacting nodes are huge, causing difficulties in defining a mesh that provides accurate results, which was also observed in this study. The model had large difficulties in converging when applying the NGI-ADP soil model, and the results looked questionable. The accuracy of the obtained solutions was therefore uncertain, and the way of modeling was not selected in the final model.

Skin Formulation

The second method tested in this study was to model the pile as a skin property in an interior face in the soil. This way of modeling limits the errors due to contacting nodes, as the skin share nodes and mesh with the surrounding geometry. By that, as observed in this study, convergence is easier to obtain. The key limitation to this model is, however, that it does not allow for specified interface properties, and the soil-pile interface will

be defined by a "glued" formulation with a rough tangential behaviour, not allowing for separation of the soil and pile. If a less frictional behaviour is desired, this issue can be solved by creating a thin soil cell, connecting the pile and the remaining soil, that is assigned material properties defined by e.g. a Mohr-Coulumb model.

In the final FE model, the skin formulation was used, with a Mohr-Coulumb interface as shown in Figure 6.7.

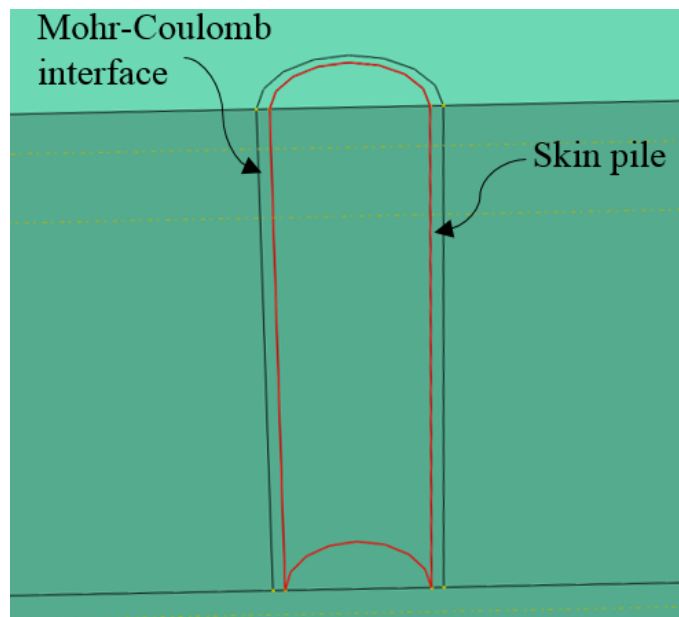


Figure 6.7: Visualization of the contact formulation used.

6.3.3 Shell properties

When applying user defined material behaviour by a UMAT user subroutine, shell properties usually have to be specified manually. The Abaqus user manual (2014) recommends using a thickness modulus of twice the value of the initial in-plane shear modulus, and shear stiffnesses given as $K_{11} = \frac{5}{6}G_{13}t$, $K_{22} = \frac{5}{6}G_{23}t$ and $K_{12} = 0$. The pile material used was assumed isotropic, such that:

$$G_{13} = G_{23} = \frac{E}{2(1+\nu)} \quad (6.2)$$

The specified shell properties are listed in Table 6.4 for the applied geometries.

Table 6.4: Shell element properties.

	Thickness modulus (GPa)	Transverse shear stiffness (GPa)		
		K11	K12	K22
Geometry 1	161.528	4.038	0	4.038
Geometry 2	161.528	3.634	0	3.634
Geometry 3	161.528	3.365	0	3.365

6.3.4 Loads

The loading on the pile included a horizontal load in the x-direction, as well as a moment about the y-axis. Loads in other directions were not considered. Due to the weight of the soil above it, the soil will be under some initial stresses. This is accounted for in Abaqus through a geostatic step, applying geostatic body forces to the entire soil volume.

All point loads were applied at the pile head, in a reference point on the symmetry axis. The pile head was constrained to follow the motion of the reference point through a rigid body constraint. The following steps were applied (in this order):

1. *Initial step.* This step apply the boundary conditions and predefined fields for the Mohr-Coulomb interface and the geostatic load.
2. *Geostatic step.* This step ensured an initial state of geostatic equilibrium.
3. *Loading step.* This step loaded the pile.

6.3.5 Boundary conditions

The bottom of the soil layer was constrained for translation in the x-, y- and z-directions. Additionally, the outer circumference of the soil cylinder was constrained for x- and y-translation. Symmetry constraints about the y-axis (no translation in the y-direction, no rotations about the x- and z-axes) was applied at the symmetry plane and in the reference point.

6.3.6 Mesh

Soil mesh

The soil was modeled isotropic with a Poisson ratio of $\nu_s = 0.495$. Thus, the soil material was close to being incompressible. For an incompressible material the bulk modulus, given by Hopperstad and Børvik (2015) as

$$K_b = \frac{E}{3(1-2\nu)} \quad (6.3)$$

becomes very large compared to the material's shear modulus. K_b is defined as the volumetric (hydrostatic) stress over the volumetric strain. That is:

$$K_b = -\frac{p}{\epsilon_{vol}} \rightarrow \epsilon_{vol} = -\frac{p}{K_b} \quad (6.4)$$

Thus, as $\nu \rightarrow 0.5$, $K_b \rightarrow \infty$ and consequently $\epsilon_{vol} \rightarrow 0$. In a finite element mesh this can result in volume strain locking, and the solution may exhibit a overly stiff behaviour and numerical difficulties.

Abaqus/CAE User's Guide (2013) suggest the use of hybrid elements when dealing with materials with a Poisson ratio larger than 0.49 to avoid the occurrence of volume strain locking.

In contact problems, a second-order mesh is preferred, as they have a better convergence rate, and first-order elements may experience volume strain locking even in the hybrid formulation, for incompressible or nearly incompressible materials (*Abaqus/CAE User's Guide* 2013).

Rectangular elements are preferred as they provide better accuracy and convergence. Therefore, the geometry of the soil was modeled to allow for the use of brick elements. However, the accuracy of square elements is limited to them remaining in an approximately rectangular shape, and attention must be paid to ensure this. Reduced integration elements are preferred to avoid shear locking in bending problems.

On the basis of the recommendations from Abaqus/CAE User's Guide (2013), the soil was modeled with C3D20RH elements. These are 20-node solid brick elements with reduced integration and a hybrid formulation.

Pile mesh

The pile had to be meshed to fit the nodes defined by the soil mesh, as the skin formulation share nodes with the contacting geometry. The soil was meshed with brick elements, thus limiting the pile mesh to rectangular elements. The pile mesh consisted of S4R elements, which are 4-node rectangular shell elements with reduced integration.

Global mesh

The mesh was refined until a sufficient mesh size was obtained. The area around the pile was especially important to refine to avoid over-constrained elements. Figure 6.8 provides the pile response for a model with various element sizes, δ , around the pile. Based on these observations the mesh was chosen to have a size of $\delta = 1$ around the pile, and in the Mohr-Coulomb interface.

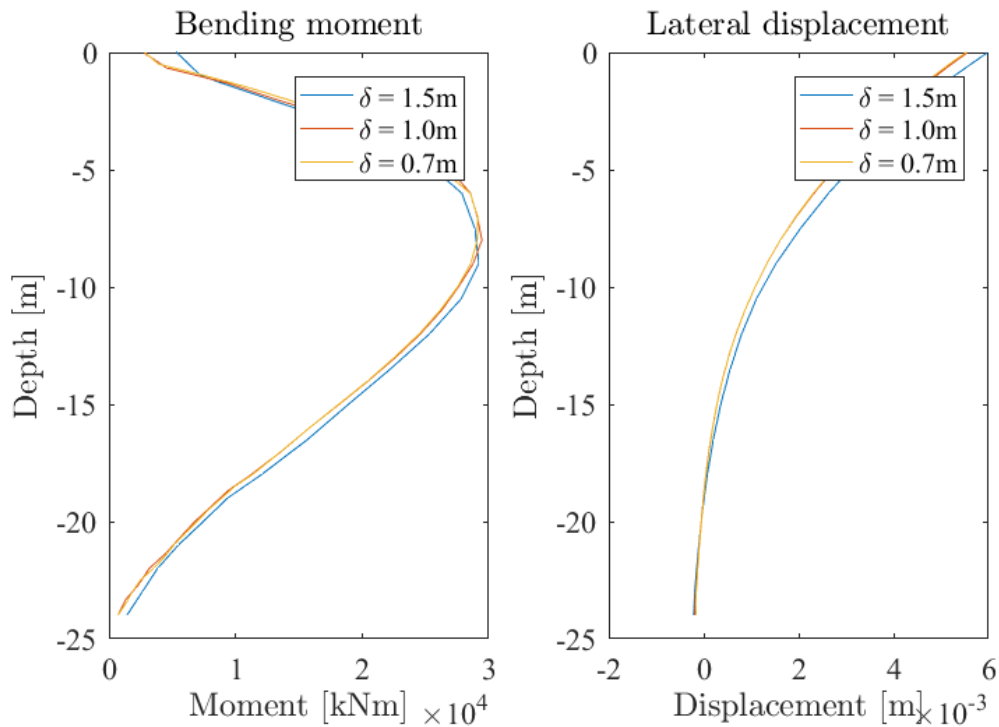


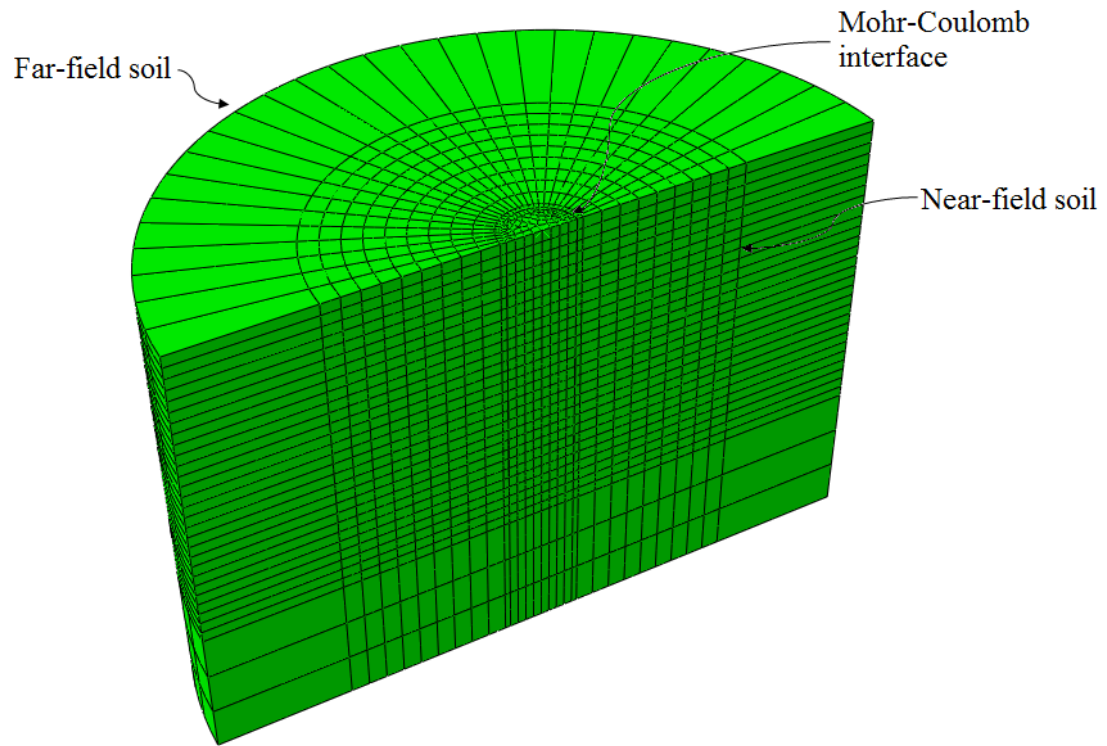
Figure 6.8: Comparison of the lateral displacement and the bending moment for different mesh element sizes.

Displacements of the soil was noticed in distances of about $3D$ from the pile center, as indicated in Figure 6.10. This area, identified as the *near-field soil*, was refined a more than the *far-field soil*, to avoid over-constraints.

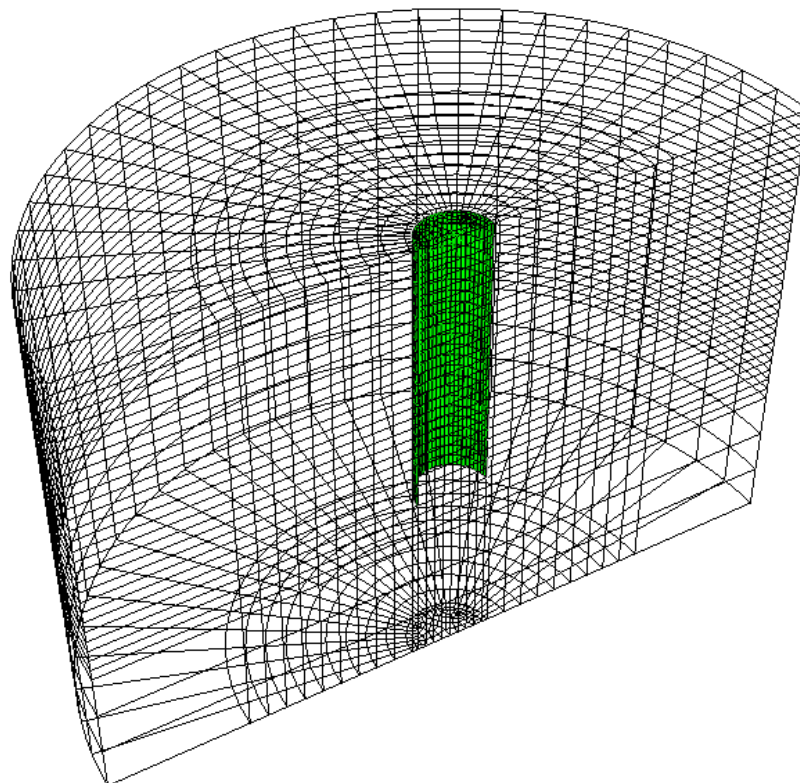
The final mesh discretisation is listed in Table 6.5. Figure 6.9a illustrates the final mesh of the model, and the pile is highlighted in Figure 6.9b.

Table 6.5: Finite element mesh.

	Element type	Number of elements	Average element size
Far-field soil	C3D20RH	1840	4
Near-field soil	C3D20RH	9268	2
MC-interface	C3D20RH	672	1
Pile	S4R	672	1



(a) Global mesh.



(b) Global mesh with the pile highlighted.

Figure 6.9: Global mesh of the Abaqus model.

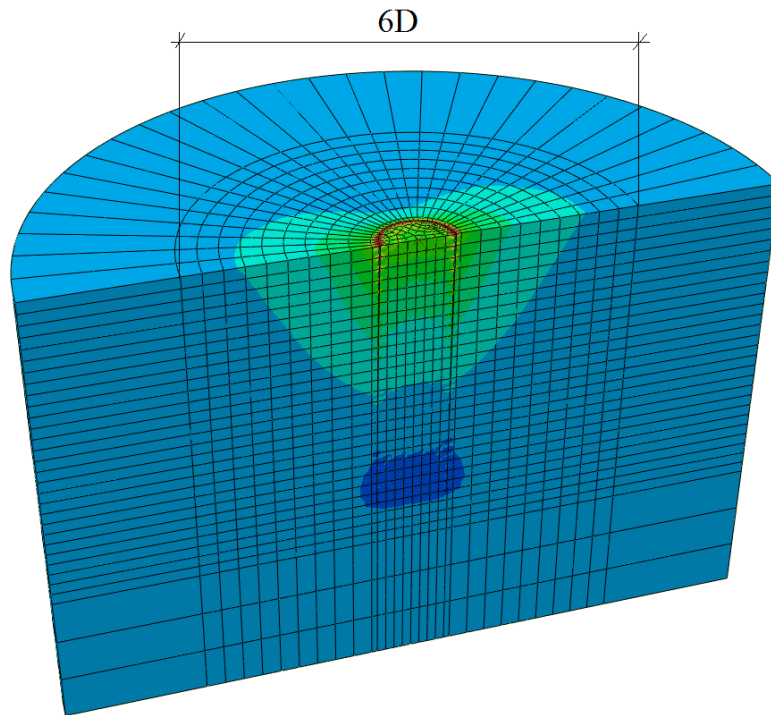


Figure 6.10: Deformation of the soil.

6.4 Verification of the FE Model

The FE model was verified against results from an equivalent model in the FE program, PLAXIS, developed by PhD candidate Ana M. Page at NTNU/NGI. The two models showed some deviations as Figure 6.11 indicate for the moment distribution and lateral displacements.

The PLAXIS model was, in general, stiffer than the Abaqus model. For a load situation of $M_y = 0, H_x = 10.2\text{MN}$, as the Figure 6.11 illustrates the results from, the PLAXIS model obtained a maximum moment that was 8.4% larger than the Abaqus model, and less pile head displacement by 14.5%. However the position of the maximum moment remained the same for both models.

The variations between the two models may be explained by the different ways of modeling the pile. Figure 6.12 plots the moment - displacement curves at the mudline for the two models, including separate curves for the elastic- and plastic components of the displacements. From the figure, it becomes evident that the differences between the two models are mainly in the elastic part. Hence, we can assume that the soil is modeled similarly between the two models, and that the deviations are occurring because of the stiffness of the pile, which is modeled as an elastic material in both models. The PLAXIS model assumes a solid volume for the pile and the soil inside the pile with an equivalent stiffness. The Abaqus model apply shell elements for the pile and define the pile material

with the actual stiffness properties.

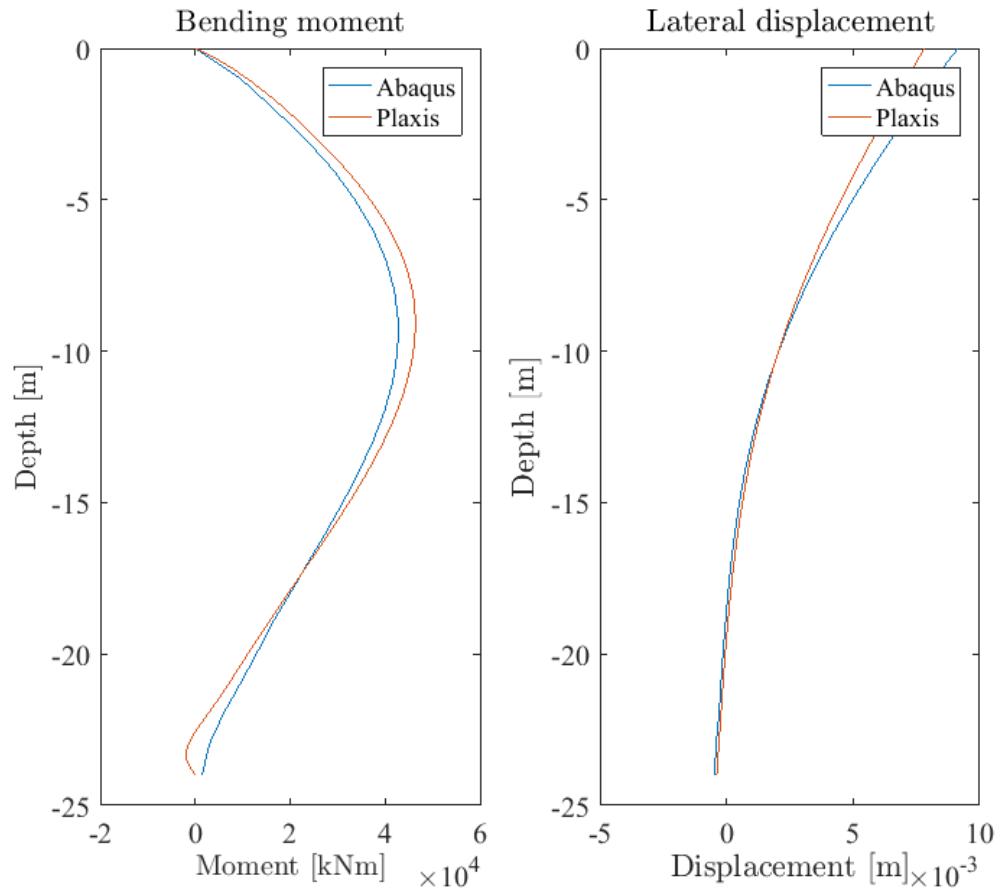


Figure 6.11: Comparison of Abaqus and PLAXIS results with a horizontal load at the pile head of 10.2MN.

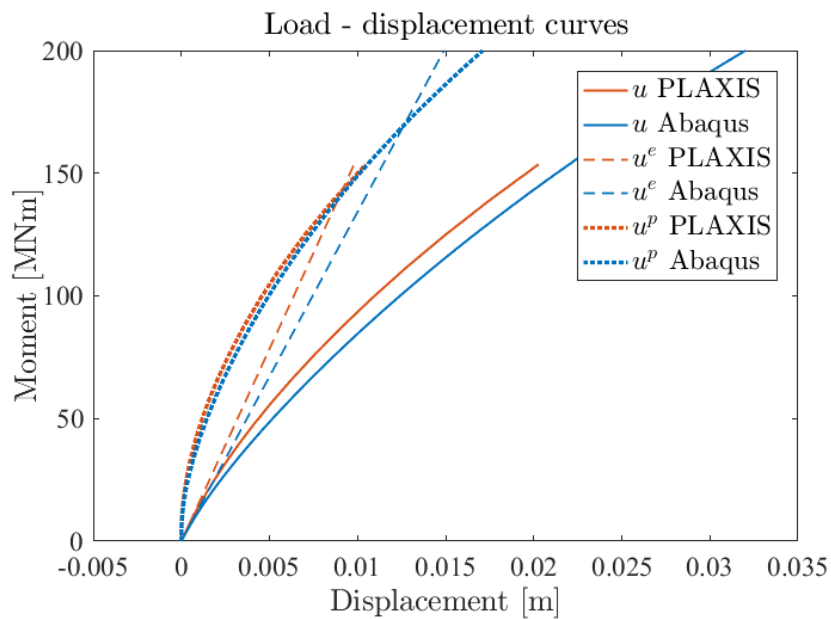


Figure 6.12: Moment - displacement curves at pile head.

Chapter 7

Introduction to 3DFloat

For further advancement and optimization of offshore wind technology, reliable *computer-aided engineering* (CAE) tools are essential for accurate predictions on the dynamic response of the structure. 3DFloat is an aero-servo-hydro-elastic tool for calculating the dynamic response of offshore wind turbines, developed by Institute for Energy Technology (IFE) and Norwegian University of Life Science (NMBU). For the purpose of this thesis, 3DFloat has been applied for performing time-domain simulations of monopile-based OWTs.

The software couples structural dynamics, hydrodynamic- and aerodynamic loads, as well as control- and electrical system dynamics, in time-domain simulations. The code is written in the programming language Fortran90. The input file allows the user to define environmental conditions as well as defining the full structure and control system (*3D Float User Manual* n.d.). The outputs are provided based on a set of user specified sensors, writing desired data to text files.

7.1 Structural Model

The program uses a FE representation of the structure, with two noded Euler-Bernoulli beam elements. Each element has 12 degrees of freedom (3 rotational and 3 translational per node). The element's local coordinate system has its origin at the element midpoint, which is where the local displacements are calculated, as indicated in Figure 7.1 (*3D Float User Manual* n.d.).

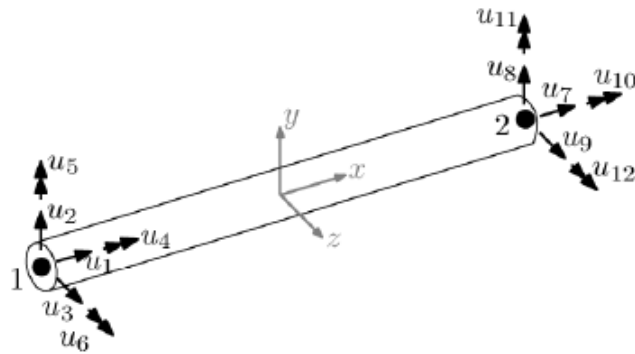


Figure 7.1: Element coordinate system in 3DFloat (*3D Float User Manual* n.d.).

The global coordinate system is such that the x-axis is positive in the direct downwind direction, the y-axis is positive in the direction pointing directly to the left when looking downwind, and the z-axis follow the tower of the OWT with a positive direction pointing upwards (towards the rotor). The global reference frame has its origin located at the SWL. Figure 7.2 shows the global coordinate system in 3DFloat.

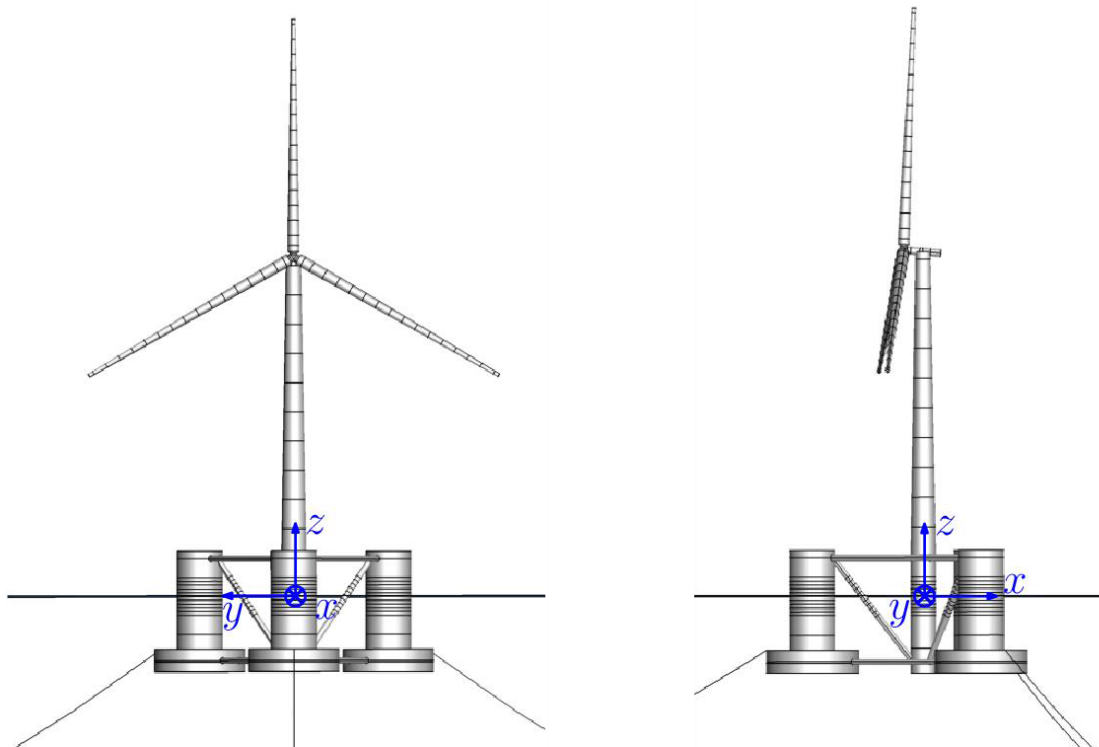


Figure 7.2: Global coordinate system definition in 3DFloat (*3D Float User Manual* n.d.).

In the input file, the turbine is defined from specifying values for the nacelle, generator, blades, tower, platform, foundation, etc.

7.2 Loads

The environmental loads on the structure are gravity loads, wave loads, wind loads, buoyancy loads and current loads, and are applied as distributed forces on the system. These are evaluated at Gauss points on the elements, and lumped to the nodes through a Galerkin formulation. Additionally, point loads or displacements can be applied directly at the nodes, and the rotor aerodynamic loads are computed by unsteady blade-element/momentum theory (BEM) (*3D Float User Manual* n.d.).

7.2.1 Hydrodynamic Loads

The wave kinematics can be represented as both regular (through either Airy-theory or stream function theories up to 12) and irregular (through superposition of Airy wavelets). To assure wave kinematics up to the wave surface for Airy waves, 3DFloat apply both Wheeler stretching and wave extrapolation formulas. The loads from the waves and currents are calculated by the relative form of Morison's equation. The buoyancy loads are calculated from the pressure field obtained from the wave kinematics model.

7.2.2 Aerodynamic Loads

The wind loads are formulated as non-linear drag terms on the tower, and on the blades, lift- and drag tables are used. The wind can both be represented as constant or as turbulent. To include turbulence, a turbulence box is applied and dragged over the turbine during the simulation. This can be generated from programs such as TurbSim.

TurbSim

TurbSim is a stochastic, full-field, turbulent-wind simulator, used to generate wind fields. The software simulates the time-series of three-dimensional wind speed vectors in a two-dimensional vertical, rectangular fixed grid, as illustrated in Figure 7.3 (B. J. Jonkman and Kilcher 2012).

The input required includes specifying grid dimensions, the reference height for the mean wind speed, as well as analysis time specifications and seed time. Additionally, the environmental wind conditions is defined through specifying which mean wind profile to use (power law, logarithmic, etc.), and on selecting a turbulence spectra (Kaimal, von Kármán, etc.). The mean wind speed at reference height should be given in magnitude, and the turbulence intensity can either be given in percentage or by standard categories defined by the *International Electrotechnical Commission* (IEC). More advanced settings related to coherence, surface roughness, shear velocity etc. can be specified, or a default setting

can be used.

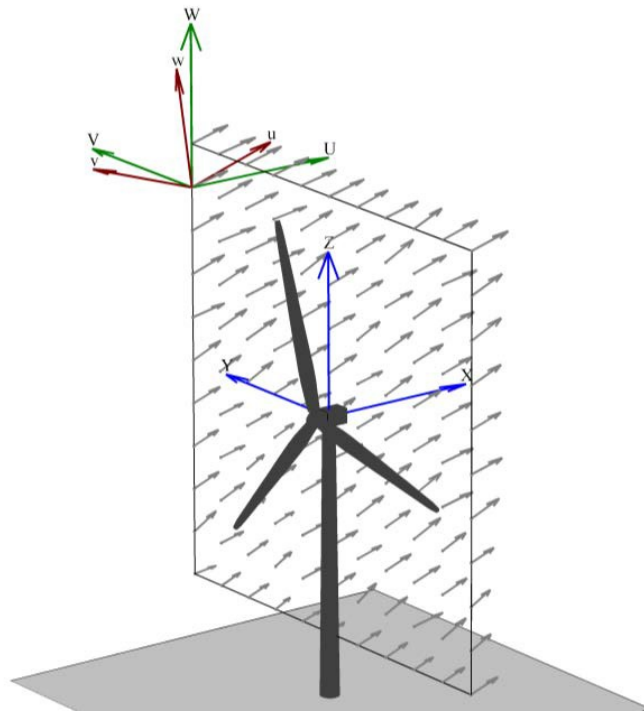


Figure 7.3: Illustration of TurbSim wind field (B. J. Jonkman and Kilcher 2012).

The output file from TurbSim is included as a input to 3DFloat, and read directly by the software upon running the simulation.

7.3 Control System

The rotor operates at various speeds, and the control system ensures that the rotational speed is as desired for various wind speeds. Below the rated wind speed the blades are at a fixed pitch angle, whereas above the rated wind speed, PI control of the pitch angle, controls the rotational speed of the rotor. This implies that for the control system ensures the correct rotational speed for operational conditions. However, idle conditions have to be ensured by manually pitching of the blades to -90 degrees.

7.4 Running Simulation

The simulations are carried using either the implicit Newmark scheme or the generalized- α method. In addition to standard time-domain simulations, eigen analyses can be performed to obtain the eigen frequencies and corresponding mode shapes of the system.

7.5 Post Processing Tools

Some post processing scripts in python are provided with the program, allowing for simple ways to analyze the outputs from 3DFloat. The scripts that has been of largest usefulness to this thesis are the following:

- *plotmodes.py*. This script plots the mode shapes corresponding to the natural frequencies obtained from the eigen analysis.
- *sensors.py*. This script plots the different sensors and provides a quick check of the environmental and mechanical conditions. Examples of plots are rotor speed, blade pitch, wind- and wave speed, etc.
- *tec2par.py*. This script converts the Tecplot data to a format that is readable by the OpenSource graphical processing tool, ParaView. This is useful to check that the modeling is done correctly.

Chapter 8

Fatigue Analysis and Optimization Assessment

This analysis compares the estimated fatigue design life of a monopile-based OWT, by applying the newly developed macro-element foundation model, to the industry practice of applying API p - y curves, and investigates the optimization potential. The OWT studied is a modified version of the OC3 Phase II turbine, at an idealized clay site. The reader is referred to Jonkman and Musial (2010) for a description of this turbine.

8.1 Method

Simulating Data

Integrated time-domain simulations in 3DFlot were performed to obtain the load- and displacement response of the OWT. The simulated time-series were of 730 seconds, whereupon the first 130 seconds were ignored, to account for start-up. Hence, the simulations consisted of a useful 600 seconds (10 minute simulations), as suggested by DNV (2010). For load cases 2 - 4 (see Table 8.4), start up took longer due to the slow winds, and consequently, simulations of 830s were performed for these load cases (whereupon the first 230s were ignored).

A structural model of the OC3 Phase II turbine in 3DFlot, was provided by Jacobus B. De Vaal and Tor Anders Nygaard at IFE. Modifications of this model was made to represent the OWT studied in this analysis, and to include the two foundation models. Both models assumed a structural damping ratio of 1% for their first natural frequency. The 3DFlot input file of load case 6 for the macro-element model is presented in Appendix A, to provide an example. Comments have been made on how to implement the p - y curves for the API p - y model.

The wind conditions in the 3DFloat inputs were described through defining a reference mean wind speed at hub height, and including a turbulence box, generated with TurbSim. The Power Law was used in describing the wind shear, and the turbulence was described through Kaimal spectra. To provide an example, Appendix B includes the TurbSim input file for load case 6. The waves were described by irregular wave models, with statistics represented by JONSWAP spectra.

The FE model described in Chapter 6, was used to calibrate the macro-element for the 3DFloat simulations. This calibration was done for various geometries of the pile. According to Kallehave et al. (2015), the pile length is typically governed by the overturning capacity or the maximum allowable tilt, the diameter is typically governed by requirements on the fundamental frequency of the structure, and the thickness is typically governed by the fatigue loads or shell buckling. As this study focus on optimization of monopile OWT foundations, with regards to fatigue loads, the geometrical parameter varied was therefore the thickness. The various geometries that the macro-element was calibrated for, are listed in Table 8.1.

Table 8.1: Pile properties.

	Mechanical properties		Geometrical properties		
	Young's modulus (GPa)	Poisson ratio (-)	Diameter (m)	Thickness (m)	Length (m)
Geometry 1	210	0.3	6	0.060	24
Geometry 2	210	0.3	6	0.054	24
Geometry 3	201	0.3	6	0.050	24

Processing of Simulated Data

The load- and displacement response of the monopile foundation, extending below the mudline, was found using a finite element program in MATLAB. This program was developed by the author, prior to the initiation of the Master's thesis work, as a contribution to the REDWIN project. Some additional modifications of the program has been made for this thesis. The program describes the soil by distributed springs along the length of the pile, each with a specific p - y curve, describing the soil response at that depth. The load- and displacement response of the pile are calculated from applied forces and moments at the pile head and the response from the soil springs. In this analysis, the 3DFloat outputs of the loads and moments at the mudline were read by the MATLAB program to calculate the resulting response of the pile foundation, for each time step. The outputs from the MATLAB program were then used in fatigue calculations at various positions along the pile foundation.

In accordance with IEC standard 61400-3 (2009), the fatigue analysis was performed based on statistical data of a normal sea state and normal turbulence model, where the environmental conditions were described by the joint probability distribution of H_s , T_p , I_u and U_{ref} . The process of calculating the fatigue damage followed the recommended practice based on S - N data, presented by DNV GL (2016), as described in Chapter 3. The calculations were done through a MATLAB script, which is included in Appendix C. This script apply the rainflow counting algorithm through functions obtained from MathWorks' file exchange.

As a reduction in the thickness of the pile also affect the resistance to failure, such as by buckling or yield, an ultimate limit state (ULS) assessment was performed for the three suggested geometries, by comparing the obtained stresses from Abaqus simulations, to the yield limit of the steel. As suggested by DNV (2014), the ULS assessment was based on environmental extreme values with a 50 year return period, and considered design load case (DLC) 6.1a from the IEC standard (2009). A misalignment of 45 degrees was applied between the rotor and the mean wind direction.

An assessment on the macro-element's sensitivity to calibrations from different FE programs, was performed by comparing the estimated fatigue damage at the mudline, obtained by the Abaqus calibration of the model, to an equivalent model in the FE program PLAXIS. The PLAXIS calibration was provided by PhD candidate Ana M. Page at NTNU/NGI.

8.2 Model Description

This analysis compares two different foundation models, which will be described in this section.

8.2.1 The API p - y model

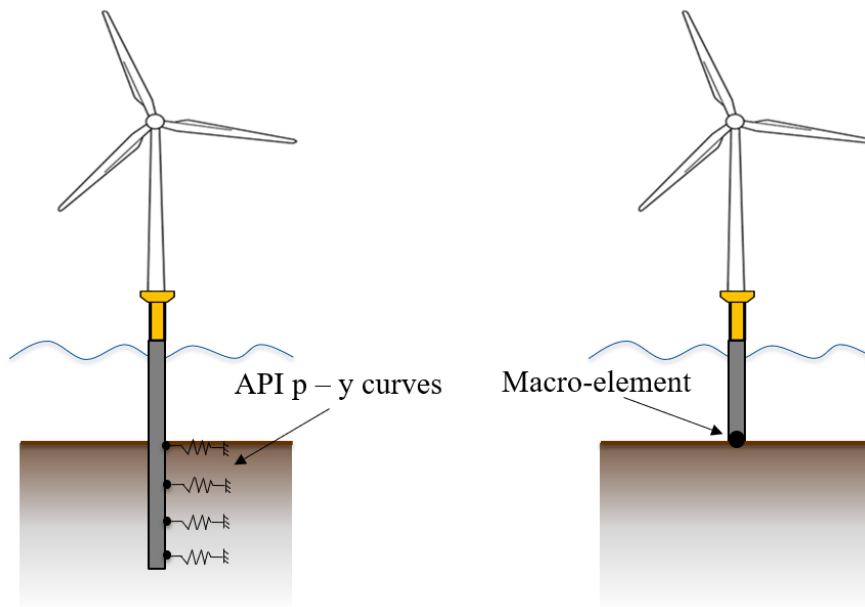
The API p - y model depends purely on the API p - y formulation of clay, as described in Section 5.2.1. The API p - y curves were implemented directly in the 3DFloat input files, as distributed springs along the monopile foundation. This is illustrated in Figure 8.1a. Each spring was defined with unique properties corresponding to the API p - y curves at the depth of the spring.

8.2.2 The macro-element model

This model apply the newly developed macro-element foundation model, described in Section 5.2.2, which has shown to accurately reproduce the experimental response from

field tests and FE analyses (Page et al. 2018). The macro-element was implemented in the 3DFloat input files, through a dynamic link library (dll), at a node on the mudline. This is illustrated in Figure 8.1b. Two input files had to be included as inputs to 3DFloat, for each unique calibration of the model. the reader is referred to Section 5.2.2 for a description of these inputs. The input for the elastic stiffness matrix of the Abaqus calibration for Geometry 1, is presented in Equation 8.1, to provide an example.

$$K = \begin{bmatrix} k_{xx} & 0 & 0 & 0 & k_{x\beta} & 0 \\ 0 & k_{yy} & 0 & k_{y\alpha} & 0 & 0 \\ 0 & 0 & k_{zz} & 0 & 0 & 0 \\ 0 & k_{\alpha y} & 0 & k_{\alpha\alpha} & 0 & 0 \\ k_{\beta x} & 0 & 0 & 0 & k_{\beta\beta} & 0 \\ 0 & 0 & 0 & 0 & 0 & k_{\gamma\gamma} \end{bmatrix}, \text{ where } \begin{cases} k_{xx} = k_{yy} = 3.08 \cdot 10^9 \\ k_{x\beta} = k_{\beta x} = 1.32 \cdot 10^{10} \\ k_{y\alpha} = k_{\alpha y} = -1.32 \cdot 10^{10} \\ k_{zz} = k_{\gamma\gamma} = 1.00 \cdot 10^{12} \\ k_{\alpha\alpha} = k_{\beta\beta} = 1.63 \cdot 10^{11} \end{cases} \quad (8.1)$$



(a) Illustration of the API p - y model. (b) Illustration of the macro-element model.

Figure 8.1: Illustrations of the two models.

To obtain the foundation response below the mudline, the following two p - y formulations were used in the MATLAB program:

- API p - y curves.
- FEA p - y curves, extracted from finite element analyses.

8.3 Turbine Properties

The turbine studied in this analysis was the NREL 5 MW wind turbine, defined by National Renewable Energy Laboratory (NREL). The description of this wind turbine is provided in *Definition of a 5-MW Reference Wind Turbine for Offshore System Development* by Jonkman et al. (2009), whereupon some properties are presented in Table 8.2.

Table 8.2: Some properties of the NREL 5 MW wind turbine (J. M. Jonkman et al. 2009).

Rating	5 MW
Rotor Orientation, Configuration	Upwind, 3 Blades
Rotor, Hub Diameter	126 m, 3 m
Hub Height	90 m
Cut-In, Rated, Cut-Out Wind Speed	3 m/s, 11.4 m/s, 25 m/s
Cut-In, Rated Rotor Speed	6.9 rpm, 12.1 rpm
Rotor mass	110,000 kg
Nacelle mass	240,000 kg
Tower mass	347,460 kg

8.4 Soil Profile

The soil profile was the one specified for the FE model, described in Section 6.2.2. For obtaining the API p - y curves, some additional parameters were needed. Table 8.3 contain all the specific soil parameters used for obtaining the API p - y curves for the idealized clay site.

Table 8.3: Soil parameters for the API p - y formulation.

γ' (kN/m ³)	$s_{u,top}$ (kN/m ²)	$ds_u dz$ (kN/m ³)	ϵ_{50} (-)	J (-)
10	50	20	0.005	0.5

8.5 Environmental Conditions

The different load cases (LCs) were selected based statistical data from the *Upwind Design Basis*, presented by Fischer et al. (2010), which are presented in Table 8.4. As the

turbine’s operating wind speeds ranges from 3 - 25 m/s, load cases 1 and 13 - 16, are idling cases, where the turbine is not operating. For these load cases, the blades were pitched out of the wind.

Table 8.4: Environmental load cases.

	Mean wind speed (m/s)	Turbulence intensity (%)	Significant wave height (m)	Peak period (s)	Probability of occurrence (%)
Load case 1	2.0	29.2	1.07	6.03	0.06071
Load case 2	4.0	20.4	1.10	5.88	0.08911
Load case 3	6.0	17.5	1.18	5.76	0.14048
Load case 4	8.0	16.0	1.31	5.67	0.13923
Load case 5	10.0	15.2	1.48	5.74	0.14654
Load case 6	12.0	14.6	1.70	5.88	0.14272
Load case 7	14.0	14.2	1.91	6.07	0.08381
Load case 8	16.0	13.9	2.19	6.37	0.08316
Load case 9	18.0	13.6	2.47	6.71	0.04186
Load case 10	20.0	13.4	2.76	6.99	0.03480
Load case 11	22.0	13.3	3.09	7.40	0.01534
Load case 12	24.0	13.1	3.42	7.80	0.00974
Load case 13	26.0	12.0	3.76	8.14	0.00510
Load case 14	28.0	11.9	4.17	8.49	0.00202
Load case 15	30.0	11.8	4.46	8.86	0.00096
Load case 16	32.0	11.8	4.79	9.12	0.00050

From the same statistical data by Fischer et al. (2010), the environmental parameters describing the 50 year extremes were as listed in Table 8.5.

Table 8.5: Environmental parameters for the 50 year extreme events.

Mean wind speed (m/s)	Turbulence intensity (%)	Significant wave height (m)
42.73	12.3	8.24

For a ULS analysis, the peak period should, according to the IEC standard (2009), be selected as the value from Equation 8.2, that results in the highest loads on the structure.

$$11.1\sqrt{H_{s,50}(U)/g} \leq T_p \leq 14.3\sqrt{H_{s,50}(U)/g} \tag{8.2}$$

8.6 Assumptions and Simplifications

Some assumptions and simplifications were made upon processing the data. When calculating the resulting stresses, used in the fatigue analysis, the axial force, N_x , was neglected, resulting in slightly lower stresses than what would have been achieved by including this. The choice of S - N data was based on established curves from DNV GL (2016), and assumptions made on the monopile welds. Figure 8.2 presents the selected S - N curve for the analysis. The data for the different S - N curves for steel with cathodic protection in seawater, defined by DNV GL (2016), are listed in Appendix D.

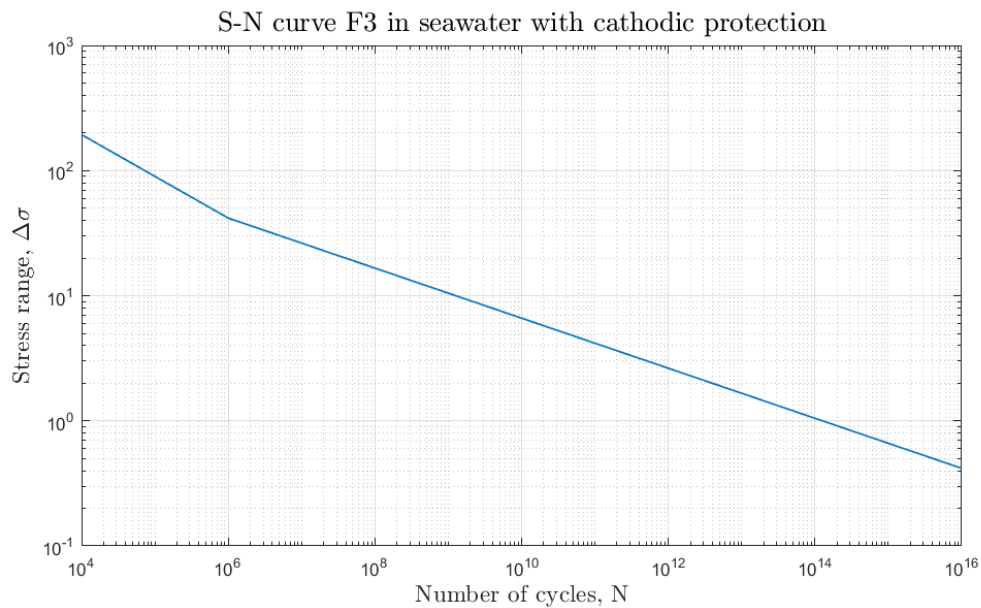


Figure 8.2: S - N curve F3 for steel in seawater with cathodic protection.

16 load cases were assumed for the fatigue damage calculations. These were assumed to repeat throughout the entire design life of the OWT, thus providing a rather unrealistic load history. As well, the wind and waves were assumed co- and unidirectional, with the exception of turbulence.

In the fatigue calculations, results from 3DFloat simulations with only one seeding of the wind- and wave representations were used for each load case. For optimal results, more seedings of the each load case should be performed, to ensure a fatigue assessment that is seeding independent. However, the same seeding was applied to both models to ensure the same loading histories.

The outputs at the mudline obtained from 3DFloat was in three directions, however, only the moment about the y-axis, M_y , and the horizontal load in the x-direction, H_x , were transferred to the MATLAB program for obtaining the response below the mudline.

The purpose of this analysis was, however, not to provide accurate estimates on the fatigue damage, but to compare the obtained estimates from different foundation modeling. The

listed assumptions and simplifications apply equally to both models investigated, and the results should therefore be valid for a comparison between the two.

8.7 Results and Discussion

This section will present the results, in the following order:

1. Model inspections. Here some results will be presented to validate the modeling in 3DFloat.
2. Natural frequency and damping. In this part of the results section, the obtained natural frequencies and damping response of the two models will be presented.
3. Mudline moments and load excitation. This subsection presents the resulting moments at the mudline, and provides a discussion on the sensitivity of foundation modeling to the environmental- and mechanical loads.
4. Fatigue assessment. Here the fatigue calculations will be presented. These include the calculations at, and below, the mudline for Geometry 1, as well as calculations at the mudline for the two new suggested geometries.
5. ULS assessment. A brief ULS assessment will be presented in this part of the results section, for the three suggested geometries.
6. Calibration sensitivity. The final part of the results will present the sensitivity of the fatigue estimates obtained from the macro-element model, when calibrating the model by different FE programs.

To make it easier for the reader, the results are being discussed as they are presented in this section.

8.7.1 Model Inspections

Figure 8.3 plots the wind speeds in the x-, y- and z-directions for load case 6. The figure confirms that the wind is modeled correctly, with a mean wind speed in the x-direction of 12m/s, and zero for the two other directions. Additionally, the figure confirms that the turbulence box from TurbSim is read after a simulation time of 100s. This was selected to ensure a steady start up.

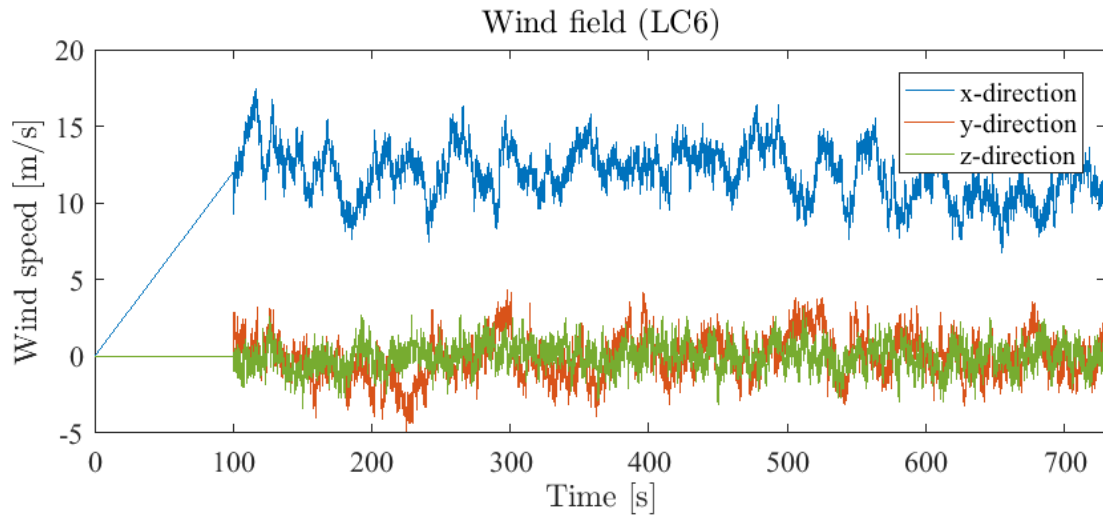


Figure 8.3: Wind speeds for load case 6.

Figure 8.4 plots a caption of the wave elevation for the same load case, with the corresponding JONSWAP spectrum plotted in Figure 8.5. The JONSWAP spectrum indicate a spectral peak at $f_p = 0.170$ Hz, corresponding to a peak period of 5.88 s, as defined for load case 6.

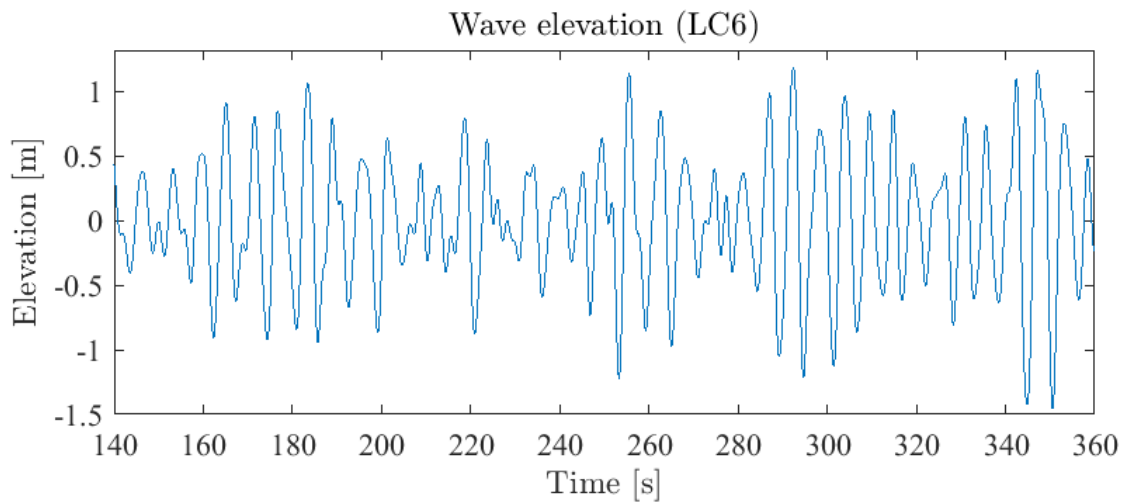


Figure 8.4: Wave elevation for load case 6.

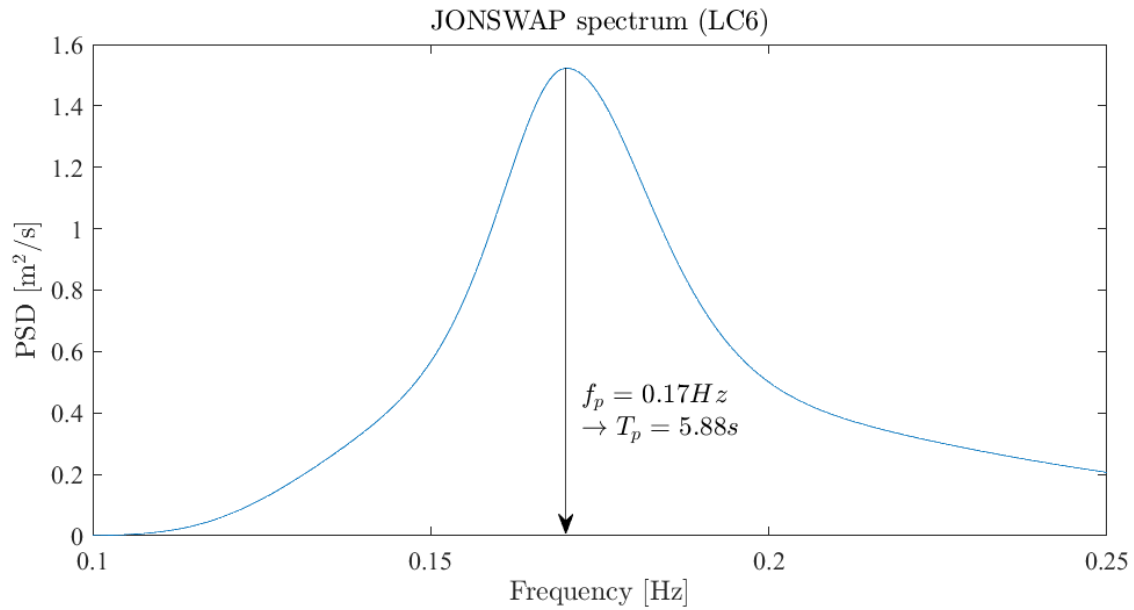


Figure 8.5: JONSWAP spectrum for load case 6.

Figure 8.6 plots the rotor speed for various LCs. The figure confirms the upper limit of rotational speed for the rotor, at 12.1 rpm, as well as no rotor speed for the idle cases. Additionally, it is visible from the figure that load case 3 spends longer on the start-up process, hence the need for a longer simulation time to obtain a useful 600s.

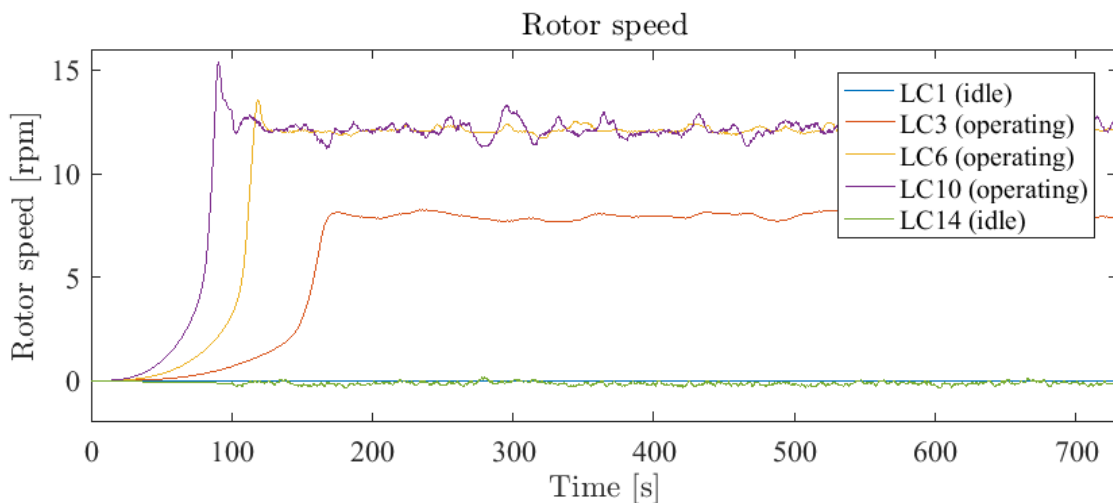
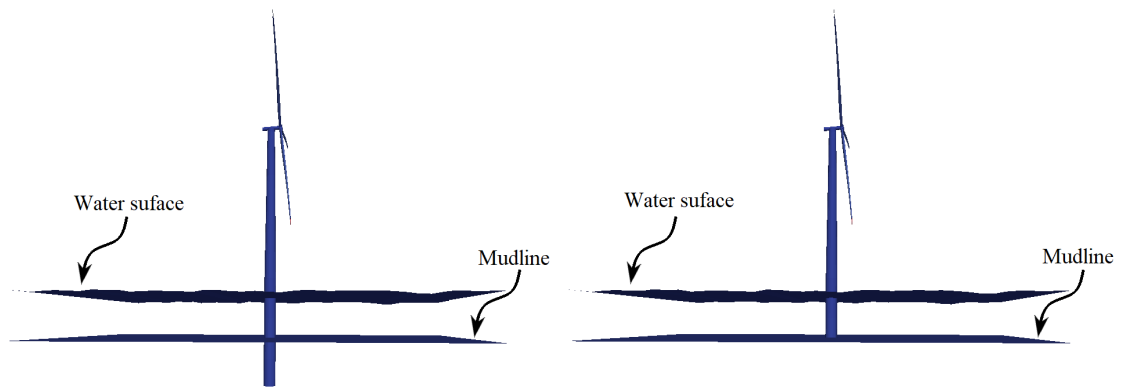


Figure 8.6: Rotor speeds for various LCs.

Figure 8.7a and 8.7b plot visualizations of the modeled OWT for the API p - y model and the macro-element model, respectively. The plots were obtained from Paraview, which provides an easy way to control the structural modeling of the 3DFloat input. As indicated by the figures, the API p - y model is extending below the mudline, whereas the macro-element model is only defined to the mudline.



(a) Paraview plot of the API p - y model in the xz-plane.

(b) Paraview plot of the macro-element model in the xz-plane.

Figure 8.7: Paraview plots in the xz-plane.

Figure 8.8 indicate that the nacelle is correctly connected for an upwind configuration, and that it is correctly attached at the tower top. Additionally, it is visible from Figure 8.8 that the blades are angled correctly for a production case.

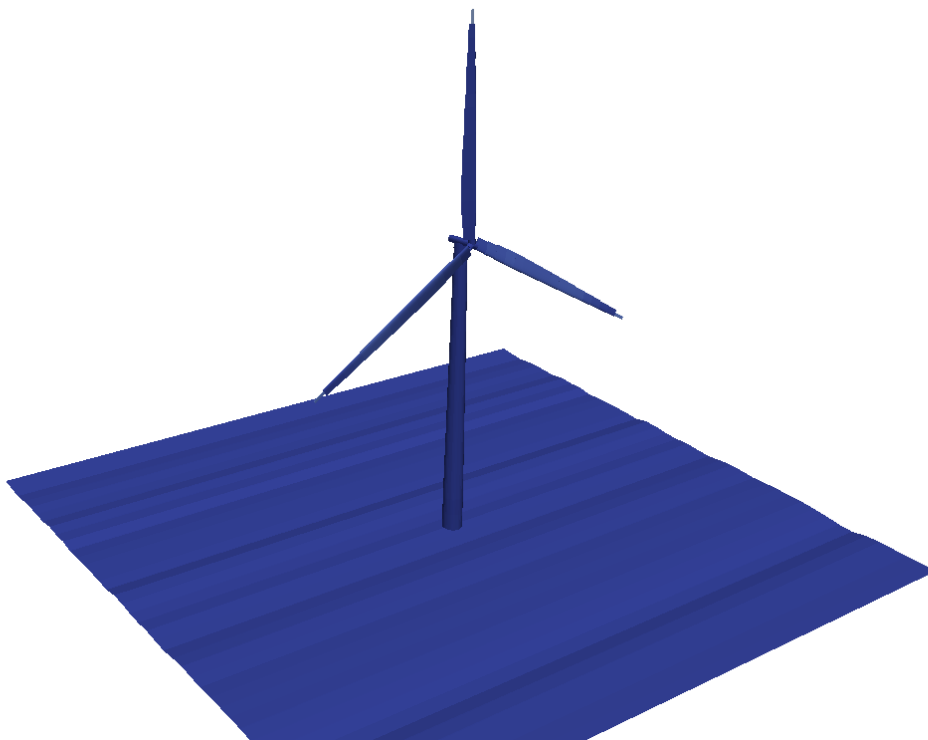
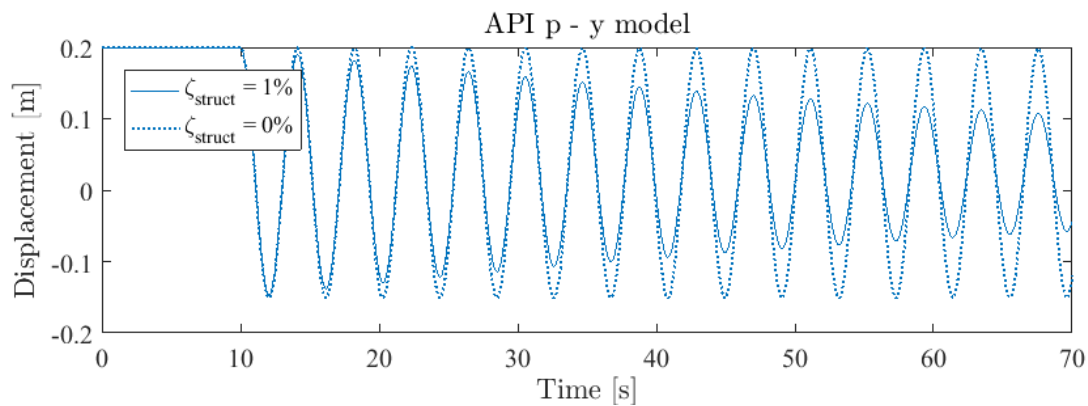


Figure 8.8: Paraview plot of the OWT.

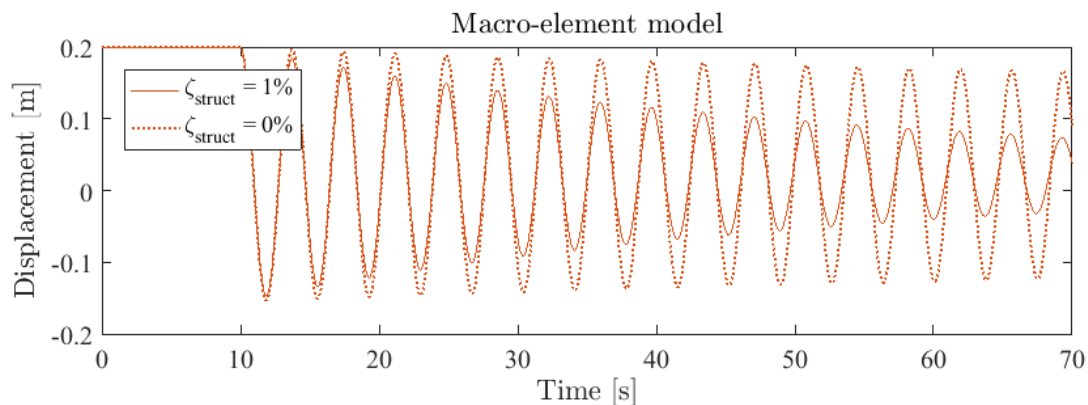
8.7.2 Natural Frequency and Damping

Before presenting the fatigue results, it is of interest to look at the resulting natural frequencies and damping of the two models, as the model differences relate to the stiffness and damping of the foundation.

Both models assumed a structural damping ratio, for the first mode, of $\zeta_{struct} = 1\%$. A free vibration test was performed to further investigate the damping of the two models. The free vibration test was performed with no environmental loads, hence, no aerodynamic damping or hydrodynamic damping were present, and the damping contributions were from the structural damping and the soil damping only. The tower top was initially displaced 0.2 meters, and then released after 10 seconds. Figure 8.9a and 8.9b presents the results, including both the actual damping on the system, with a structural damping ratio of $\zeta_{struct} = 1\%$, as well as a case where there was assumed no structural damping ($\zeta_{struct} = 0\%$). The prior indicate the higher total damping in macro-element model, whereas the latter clearly indicate the presence of soil damping in macro-element model, and the lack of it in the API p - y model.



(a) Tower top displacement from free vibration test of the API p - y model.



(b) Tower top displacement from free vibration test of the macro-element model.

Figure 8.9: Tower top displacements from free vibration test with initial displacement of 0.2m.

Longer periods are also seen for the API p - y model, indicating a lower fundamental frequency. The first two tower-bending frequencies are the most important in OWT design, as these often coincide with the frequencies of the environmental and mechanical loads. The natural frequencies of the systems were found through eigen analyses in 3DFloat, and Figure 8.10 plots the corresponding mode shapes of the first tower-bending frequencies.

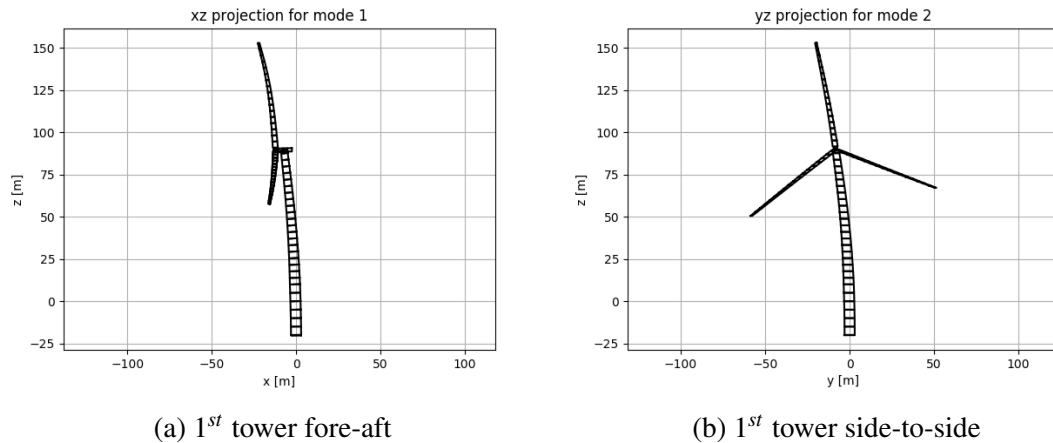


Figure 8.10: Visualizations of the 1st tower-bending natural frequencies

The obtained values for the fundamental tower-bending frequencies of the two models are listed in Table 8.6. Additionally, the natural frequencies of a model rigidly clamped at the mudline, as well as one applying the elastic stiffness matrix of macro-element model at the mudline, were included for verification purposes.

Table 8.6: 1st simulated tower-bending natural frequencies for different foundations models.

	API p - y model	Macro- element model	Elastic stiffness matrix	Clamped model
1 st fore-aft natural frequency (Hz)	0.241	0.270	0.270	0.295
1 st side-to-side natural frequency (Hz)	0.241	0.271	0.271	0.295

The first thing to notice is that the clamped model obtained the highest natural frequency, as expected from the stiffest model. The natural frequency of the macro-element correlates to its elastic part, and it was therefore expected to obtain approximately the same fundamental frequencies as the model applying the equivalent stiffness matrix at the mudline. This was also the obtained response presented in Table 8.6. The API p - y model resulted in the lowest values for the fundamental frequencies, noting that it was the softest

model. Assuming that the macro-element model provides the correct frequencies, the API p - y model was seen to under predict the fundamental fore-aft tower-bending frequency by 10.7%. This corresponds to other observations found in the literature. Kallehave et al. (2015) presents in their study a comparison of the measured natural frequency to the design frequency of 400 monopile-based OWTs, all under predicting the fundamental frequency of the system, some by more than 20%. Byrne et al. (2015) found the method based on API p - y curves to significantly under predict the ultimate capacity and stiffness of monopiles in clay.

Figure 8.11 plots the moment - displacement curve at the mudline for the two different models. The figure clearly indicate the softer response of the API p - y model, as compared to macro-element model.

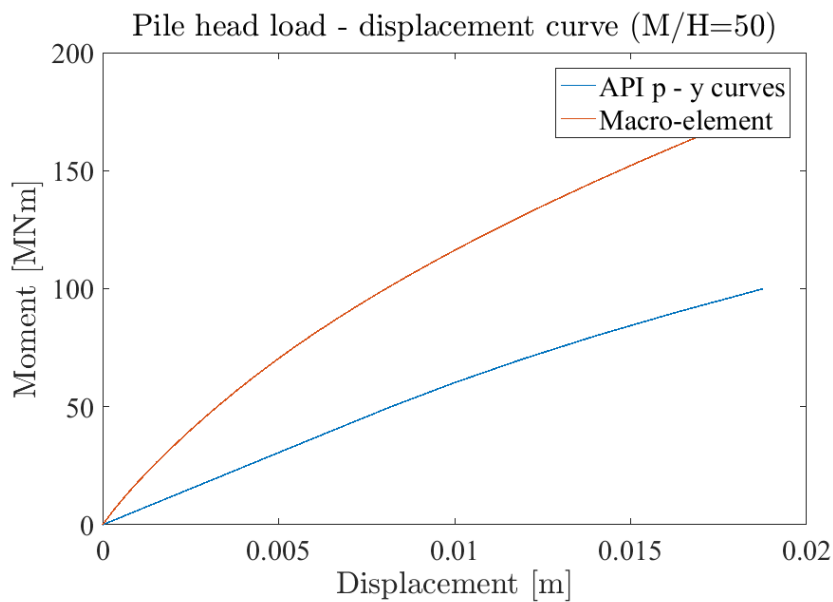


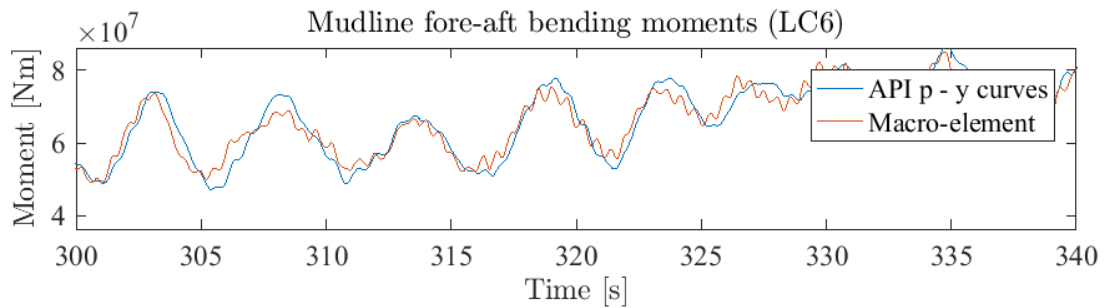
Figure 8.11: Load - displacement curve at the mudline for $M/H = 50$.

8.7.3 Mudline Moments and Load Excitation

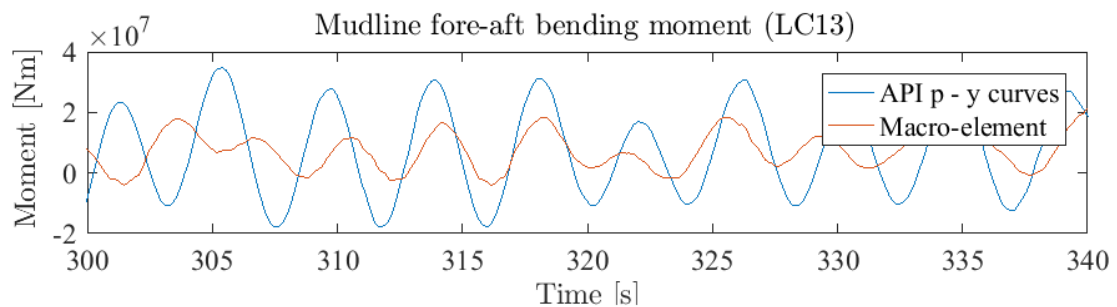
This subsection presents the results on the mudline moments, and discuss the excitation from the environmental- and mechanical loads on the structure. With this in mind, an easier evaluation of the fatigue results is ensured.

Captions of the resulting mudline moments, are presented in Figure 8.12a and 8.12b for load case 6 (operating) and load case 13 (idling), respectively. It is observed that the general moment response was more amplified for the API p - y model as compared to the macro-element model, however, to a greater extent for the idling cases. Under power production, the rotor will cause forced vibrations on the support structure, hence the more vibratory moment response observed. In contrast, with the rotor parked for the idling cases, the support structure is free to vibrate at its natural frequency. It may be observed

from Figure 8.12b, that the moment response appears to, in general, be obtaining peaks separated by periods corresponding to the first natural period of the two models.



(a) Caption of the mudline moments for load case 6.



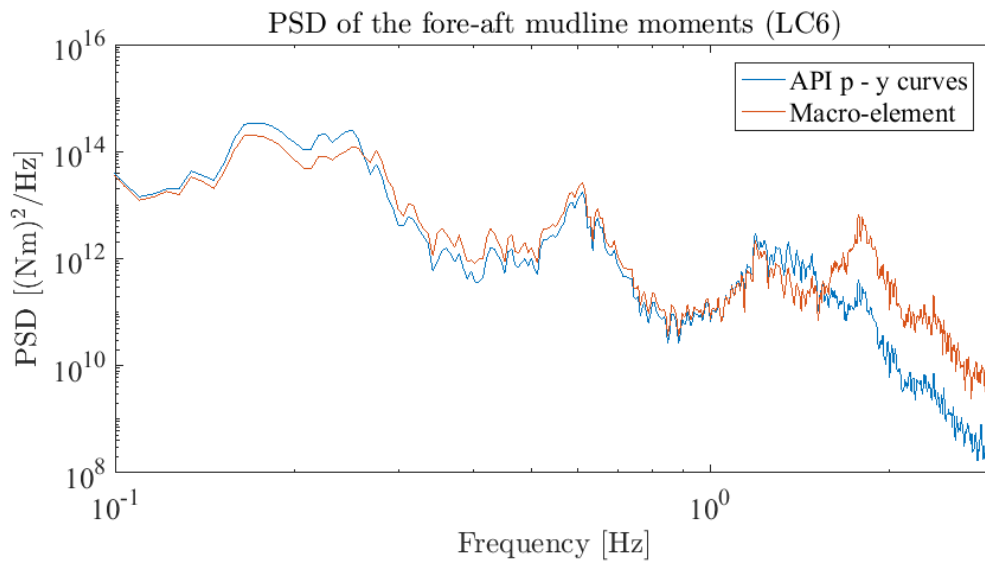
(b) Caption of the mudline moments for load case 13.

Figure 8.12: Mudline fore-aft bending moments.

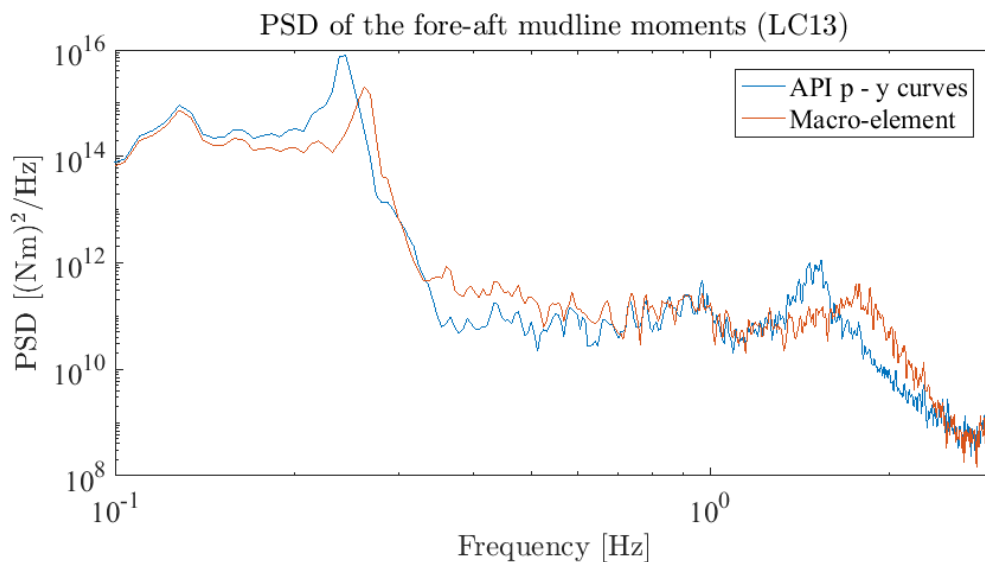
This can also be seen from PSDs of the fore-aft mudline moments, as plotted in Figure 8.13a and 8.13b for the same load cases. The initial peak corresponds to the first tower-bending frequency in the fore-aft direction. As seen by the figures, the operating case obtained a wider spread of the moment energy over the frequency spectrum, whereas the idling case had the energy greatly concentrated at the fundamental frequency of the support structure. Note that the plots are on a log-scale.

As the macro-element model, in general, obtained lower moment amplitudes than the API p - y model, lower estimates on the fatigue damage are thus also expected.

Dynamic amplification occurs when the natural frequencies of a dynamic system is excited. Therefore, to understand why the macro-element model is obtaining lower amplifications of the mudline moments, a relation to the natural frequencies and the extent of excitation from the environmental- and mechanical loads will be discussed further. The discussion will also include an assessment on damping of the dynamic response.



(a) PSD of the fore-aft mudline moments for load case 6.



(b) PSD of the fore-aft mudline moments for load case 13.

Figure 8.13: PSDs of the mudline fore-aft bending moments.

Excitation by Environmental Loads

Figure 8.14 plots the JONSWAP spectrum for load case 6, describing the frequency distribution of the wave energy for that load case. Additionally, vertical lines corresponding to the fundamental fore-aft tower-bending frequency of the two models, are included to visualize the amount of energy from the waves that are in the frequency range of the fundamental frequencies to the two models.

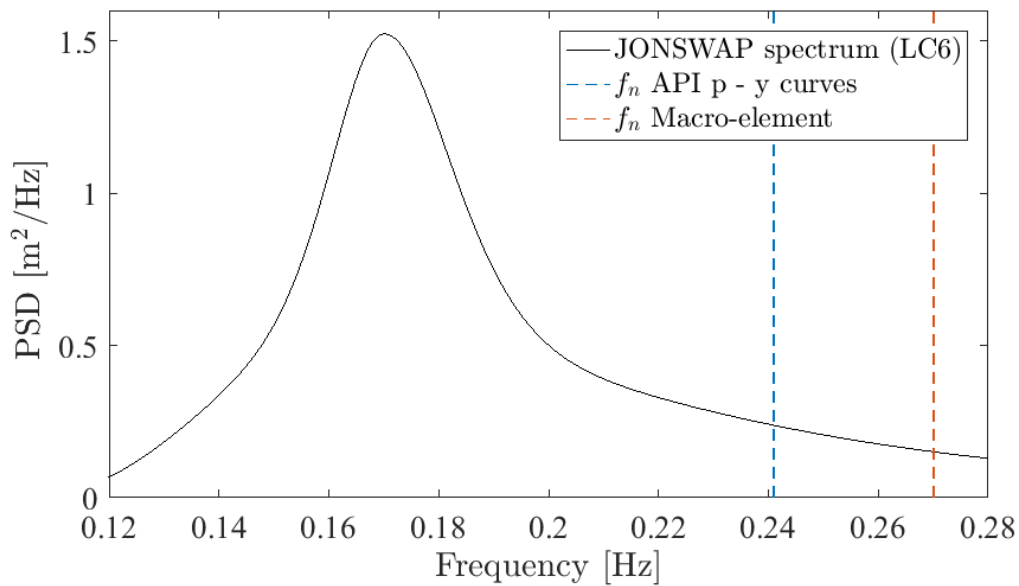


Figure 8.14: JONSWAP spectrum of load case 6, the fundamental frequency of the two models.

From the JONSWAP spectrum, it is observed that the wave energy at the fundamental frequency of the API p - y model, is almost double as compared to the wave energy at the fundamental frequency of the macro-element model. The fundamental frequency of the macro-element model is therefore expected to be less excited by the wave loads on the structure, than the API p - y model. Consequently, larger amplifications are expected for the API p - y model. This corresponds to the observations above.

Similar responses were seen for all load cases, as the peak frequency of the JONSWAP spectrum remained lower than the fundamental frequencies of the two models.

Excitation by Mechanical Loads

In addition to coincidence with the environmental frequencies, the structure's natural frequencies may be excited by the mechanical loads from the turbine itself.

The Campbell diagram, plotted in Figure 8.15, provides a visualization of how close the OWT support structure is to be excited by the mechanical frequencies of the rotor system. The fundamental frequencies of the system are plotted as functions of rotor speed, and superimposed on the plot are lines that correspond to 1P, 3P and 6P. The vertical lines corresponds to the average rotor speed for each operating load case. The figure indicate that the API p - y model was much closer to exciting 1P than the macro-element model. For the load cases that have the wind turbine operating at the rated speed, the API p - y model was, in fact, quite close to coinciding with the excitation frequency of 1P. It is therefore expected that the API p - y model will obtain a larger amplification of the 1P

resonance response than the macro-element model.

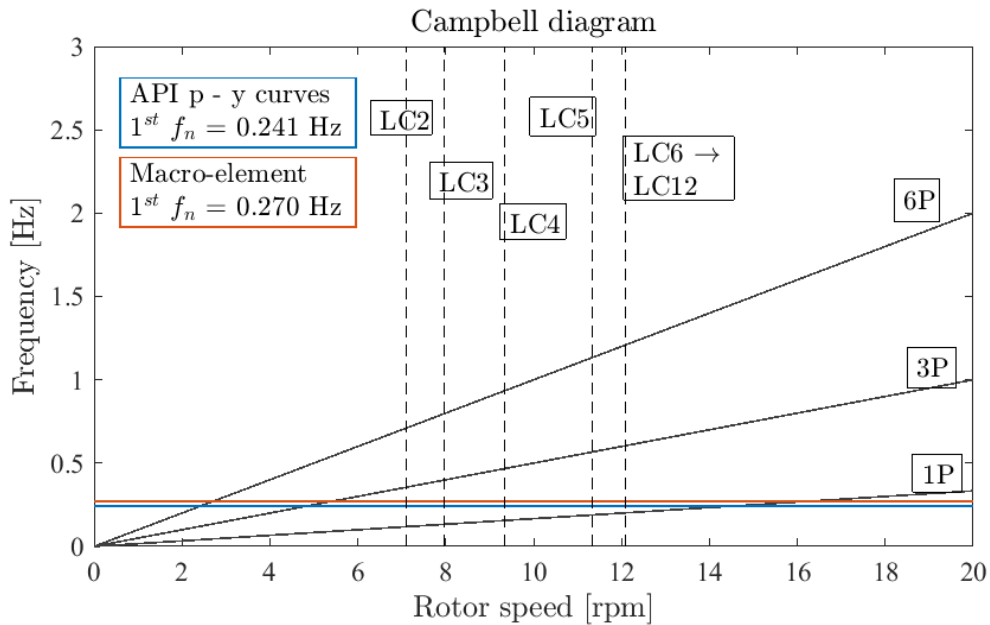


Figure 8.15: Campbell diagram.

Damping of the Dynamic Response

Damping ensures energy dissipation, and by that reducing the amplification of the dynamic response. As the macro-element includes soil damping in its formulation, it will obtain a larger dissipation of energy than the API p - y model, which neglects the contribution of soil damping. Consequently, in addition to the expected lower amplitudes due to the differences in the natural frequencies as previously discussed, the macro-element model is also expected to obtain lower amplitudes of the mudline moments due to the additional damping.

In the operating cases, the aerodynamic damping will be of highest significance to the total damping on the structure, in the fore-aft direction, and is equally present in both models. It is therefore expected that the contribution from soil damping to the deviations between the two models, will be of largest significance for the idling cases, where the aerodynamic damping is negligible.

8.7.4 Fatigue Assessment

To ensure that the fatigue calculations were performed at the cross-sectional position of the pile with the largest fatigue damage, the fatigue damage over the cross-section at the mudline was investigated for load case 6. The different positions on the cross-section investigated is indicated in Figure 8.16. These positions were uniformly spread across the circumference of the pile, with an angle of 45 degrees between them.

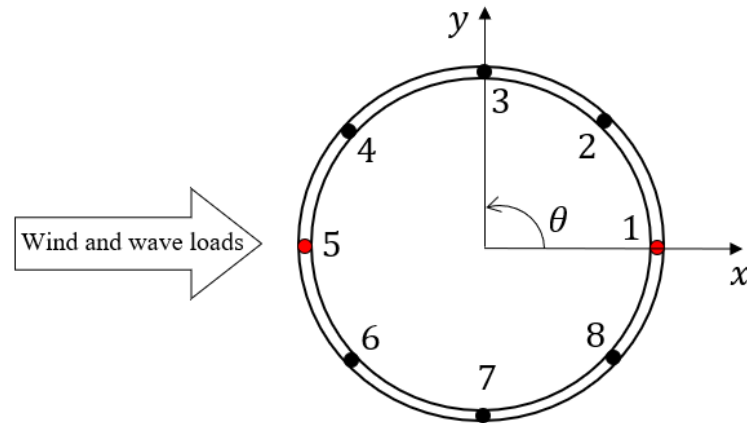


Figure 8.16: Positions on the cross-section investigated for fatigue damage.

The, by far, highest fatigue damage occurred for positions 1 and 5 (marked in red). This was as expected, as these positions are on the axis of the main loading direction, for both the wind and wave loading applied. Figure 8.17 plots the moment time-series obtained for load case 6 at the various positions on the cross-section of the pile. As the figure indicate, the larger moment amplitudes are found for positions 1 and 5, thus resulting in larger fatigue damage. Additionally, as the figure indicate, symmetry of the pile ensures equal (but reverse) moments over the symmetry plane.

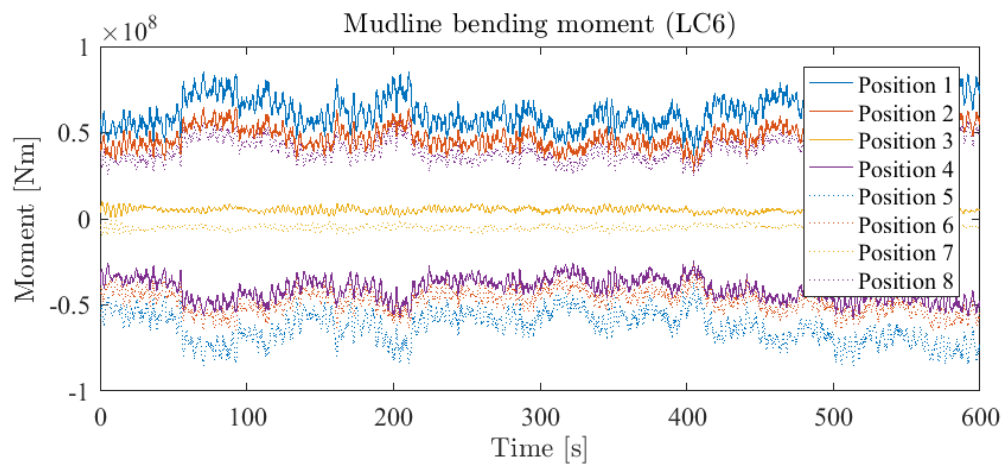


Figure 8.17: Mudline moments at different positions on the pile cross-section.

Similar results were expected for the remaining load cases, and the total fatigue calculations were therefore only performed for position 1 (which is equal to position 5).

Initial Geometry

The normalized values of the estimated fatigue damage at the mudline for Geometry 1, are presented in Figure 8.18. Here, the probability of occurrence has been included for a

better visualization of each load case's contribution to the total fatigue damage.

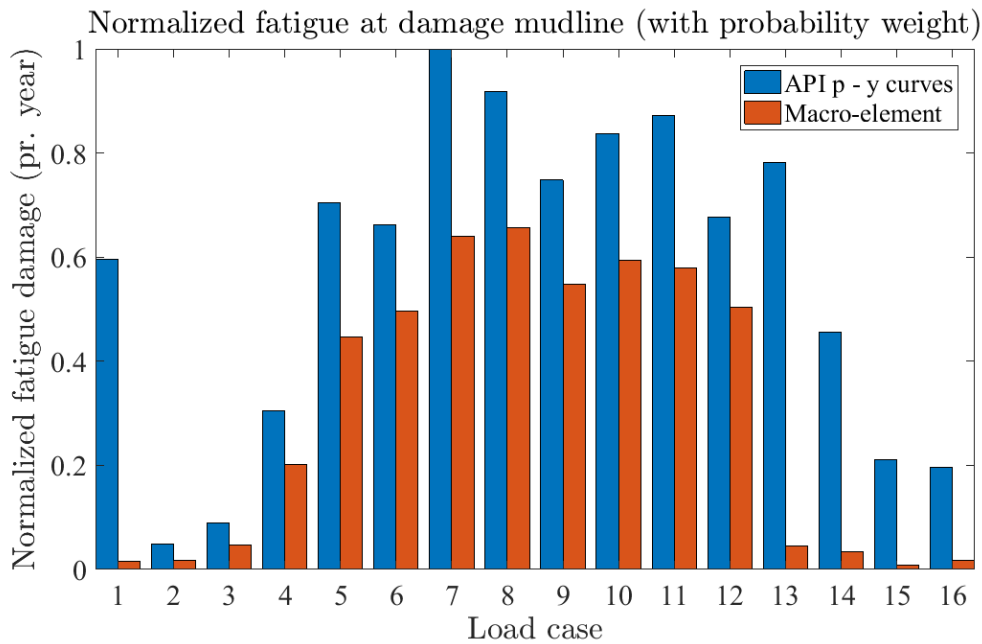


Figure 8.18: Normalized fatigue damage at the mudline for the initial geometry.

With the selected S - N curve, this resulted in expected fatigue design lifetimes as provided in Table 8.7.

Table 8.7: Expected fatigue life for the initial geometry.

	Expected fatigue design life (years)
API p - y model	18.7
Macro-element model	35.5

The fatigue life expectancy at the mudline was hence increased by 89.8%, when modeling the foundation by the use of the macro-element as compared to the industry practise of API p - y curves. Similar observations have been made by Kallehave et al. (2015), where a reassessment on the fatigue damage based on measured data of the natural frequency and wave loads, resulted in an increase in the fatigue life of the structure by 88%.

As the two models are identically described above the mudline, and are exposed to the exact same wave- and wind load histories of the same seeding, the variations in the estimated fatigue damage should only be caused by the different foundation modeling. Here, the two important factors relate to the differences in stiffness and damping, as previously discussed. The obtained fatigue damage estimates correspond well to the expectations based on above assessment of the mudline moments.

Figure 8.18 also illustrates how the foundation performance appears to be more significant for the idling cases. Again, this relates to the differences in the natural frequencies as discussed earlier. With the absence of the rotor to generate forced vibrations on the structure, it is allowed to vibrate at its natural frequency. As the fundamental frequency of macro-element model is larger than the API p - y model, it will endure less excitation from the wind- and waves, thus result in lower amplifications of the mudline moments, and consequently less fatigue damage. The decisive factor to fatigue damage is the amplitudes of the stresses, and as larger deviations in the mudline moment amplification are obtained for the idling cases, the differences in the estimated fatigue damage will also be larger. Other studies, such as by Aasen et al. (2017) have seen the same trend of the idling cases to be more sensitive to foundation performance.

Additionally, the macro-element model will limit the amplification even further through energy dissipation by soil damping. However, in this analysis it is difficult to quantify the contribution to the differences in fatigue damage from the differences in stiffness and damping isolated, as they are co-occurring. Yet, it is believed that the contribution from the damping is less significant than the natural frequencies, as small differences in the natural frequencies have showed to have a large impact on the dynamic amplification of the support structure.

Figure 8.19 plots the resulting maximum values for the moments at the mudline for each load case. It is noticeable that the maximum moments do not differ much between the two models. This corresponds to observations by Jung et al. (2015), where they found that the maximum moments obtained by API p - y curves and FEA varied insignificantly, regardless of large deviations in the displacements and rotations.

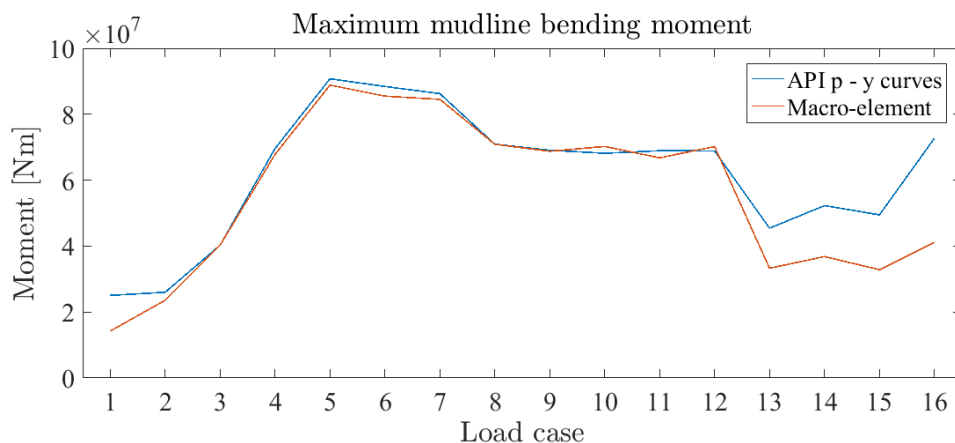


Figure 8.19: Maximum obtained moments at the mudline.

As the figure indicate, the maximum moments occur for load case 5 for both models. Yet, load case 5 was not the one accumulating the most fatigue damage. This indicate how the fatigue damage is not affected by the magnitudes of stresses, but by the amplitudes of the stress cycles. Figure 8.20 plots the moment time-series of load case 5 and load

case 12 for the API p - y model. Even though the magnitudes of the moments are, in general, larger for load case 5, load case 12 accumulated the more fatigue damage, due to the larger moment amplitudes.

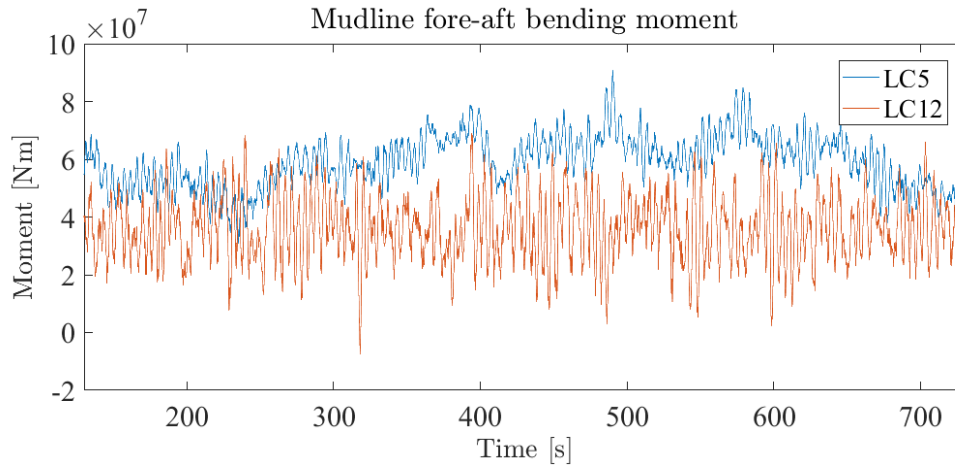


Figure 8.20: Mudline moments of load cases 5 and 12 for the API p - y model.

Fatigue Along the Pile

The moments at the mudline are transferred to the monopile foundation that extends below the mudline, and typically, the maximum moments on the foundation occur at a distance beneath the mudline. For optimization of the pile foundation, it is also important to investigate the fatigue along the pile, as a better understanding of the fatigue damage along the foundation, will increase the reliability of the positioning of the welds. Additionally, the thickness of the monopiles used in industry is typically not constant, but varying with depth. An accurate assessment of the fatigue occurring along the pile, may therefore be of usefulness in optimization of foundation design.

For the fatigue assessment below the mudline, the macro-element model applied two different p - y formulations in the MATLAB program: one applying FEA p - y curves, obtained from finite element analysis, the other applying API p - y curves. Figure 8.21 plots the obtained pile response from the different p - y formulations, and compares this to results from finite element analysis. As the figure indicate, the FEA p - y curves provide a much more accurate representation of the pile response than the API p - y curves. Hence, the FEA p - y curves are believed to provide the more accurate estimates on the fatigue damage between the two p - y formulations.

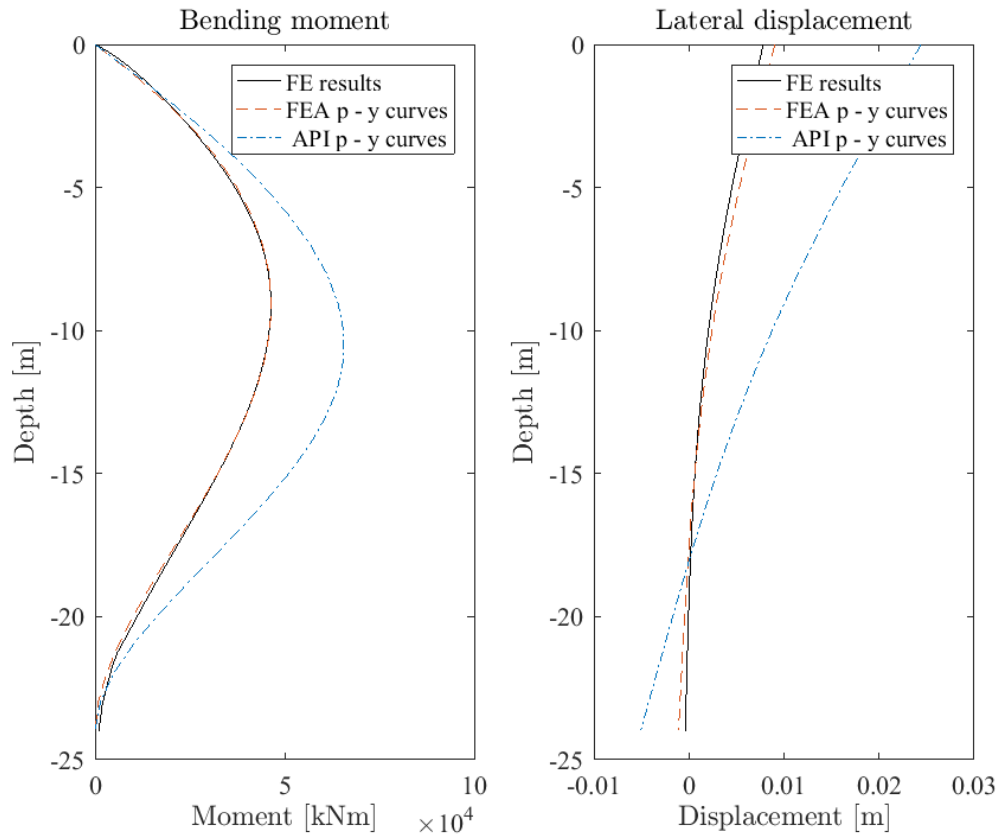


Figure 8.21: Comparison of the pile response from Abaqus model to the two p - y formulations.

The resulting normalized values of the yearly total fatigue damage along the pile foundation is presented in Figure 8.22. Here, the probability of occurrence has been included to each load case, and the contribution from all load cases has been summed at each position along the pile.

Based on the comparison with the FE model, and the more accurate foundation description of the macro-element model, it is believed that the macro-element model, applying FEA p - y curves (in orange), provides the most accurate representation of the fatigue calculations along the pile foundation. This model showed to result in a maximum fatigue damage of less than half of the maximum of the pure API p - y model. This highlights the extreme potential of improved methods. However, most of this difference was due to the larger deviations at the mudline. Between using API p - y curves below the mudline and FEA p - y curves with the same damage estimate at the mudline, the maximum fatigue below the mudline was 18% lower, when applying the FEA p - y curves.

Another important observation is that the position of the maximum fatigue damage differ between applying FEA p - y curves and API p - y curves. An accurate prediction of this position may be of great importance in considering the positions of the monopile welds.

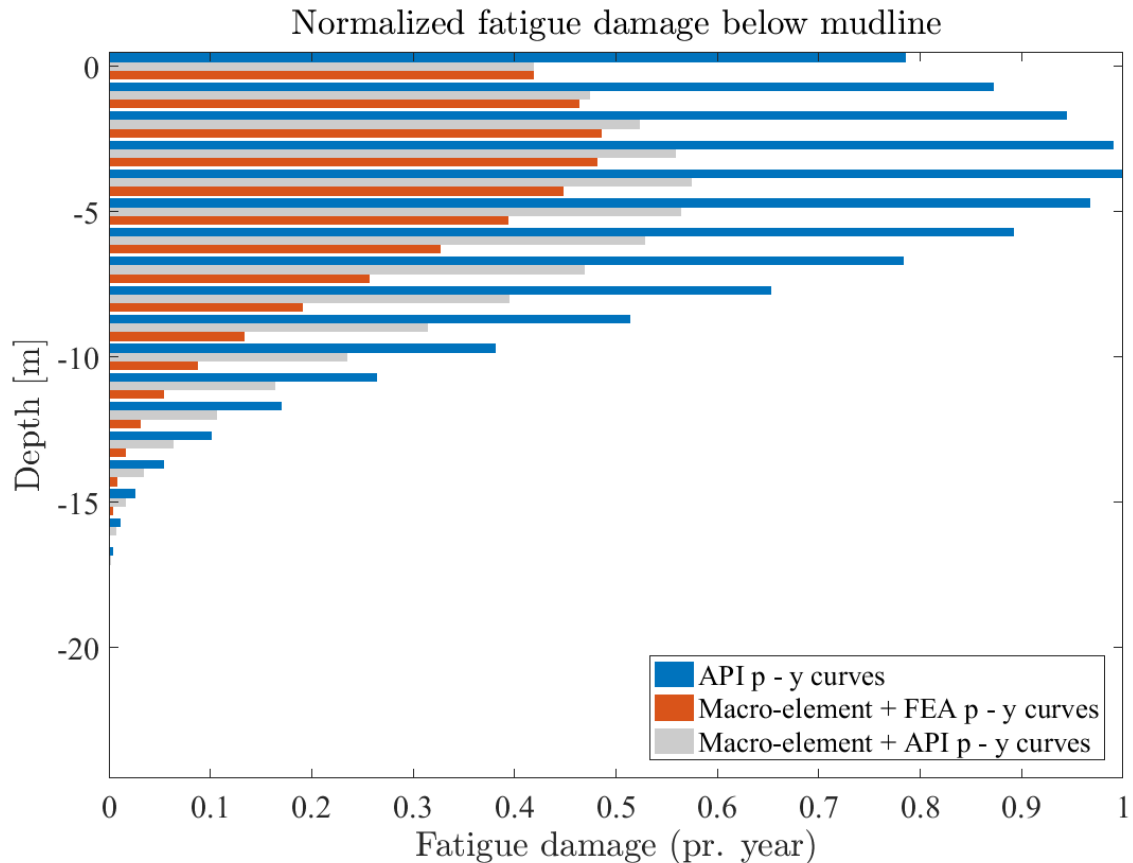


Figure 8.22: Normalized fatigue damage below the mudline.

The welds are the most vulnerable positions along the pile to cyclic loading, and it is therefore important to avoid positioning welds at areas that are expected to endure large fatigue damage (Kallehave et al. 2015).

Optimization of the Pile Geometry

The wall thickness of the monopile was reduced to obtain similar estimations on the fatigue damage at the mudline from the macro-element model as the API p - y model, to investigate the potential of steel savings. Two new geometries were suggested, where one obtained approximately the same fatigue life expectancy (Geometry 3) and the other obtained approximately the same fatigue damage for the operating cases (Geometry 2). The resulting fatigue damage at the mudline for the different geometries are plotted in Figure 8.23, and the expected fatigue lifetimes are presented in Table 8.8.

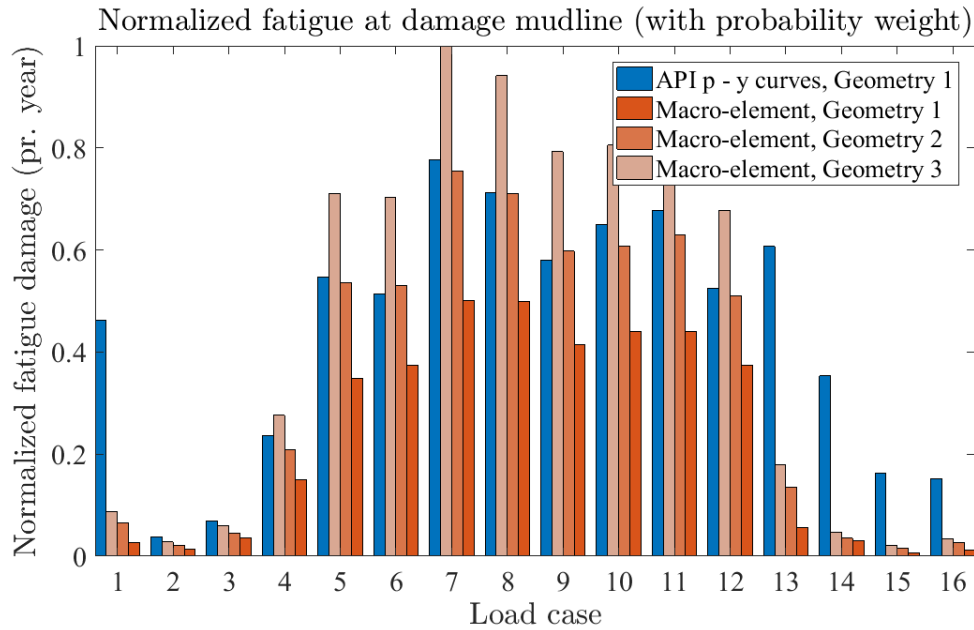


Figure 8.23: Normalized fatigue damage at the mudline for the different geometries.

Table 8.8: Expected fatigue life for the different geometries.

	Pile thickness (m)	Expected fatigue design life (years)
API p - y curves, Geometry 1	0.060	18.7
Macro-element, Geometry 1	0.060	35.5
Macro-element, Geometry 2	0.054	24.3
Macro-element, Geometry 3	0.050	18.4

For the new suggested geometries, the wall thickness remained constant by the new value. The entire monopile geometry was changed, while the tower remained with its initial geometry. The monopile in this analysis extended 10m above the mudline and 24m below, thus having a total length of 34m. The initial geometry was of constant diameter of 6m, and constant thickness of 0.06m. The initial steel volume of the monopile was therefore of 38.1m³. The potential steel savings of the monopile for the two new suggested geometries are listed in Table 8.9.

Table 8.9: Possible steel savings of the monopile.

	Thickness reduction (%)	Steel savings		
		Volume (m ³)	Tonnage (ton) (assuming $\rho_{steel} = 7850kg/m^3$)	Percentage (%)
Geometry 2	10	3.77	29.6	9.9
Geometry 3	17	6.29	49.4	16.5

This indicates a large potential on steel savings of the monopile alone. By trusting that the macro-element model provides more accurate estimates on the fatigue damage, a potential of steel savings on the monopile ranging from 10-17% was recognized. These results supports the statement from Kallehave et al. (2015), on realistic steel savings in the industry of 10 - 25% to be expected by better predictions on the foundation response.

8.7.5 ULS Assessment

In addition to fatigue, another design driver for the choice of monopile wall thickness, is the issue of shell buckling during installation and extreme events (Kallehave et al. 2015). However, in a linear buckling analysis, the buckling load factor (BLF) will be overestimated due to a model representation of a geometry with no imperfections. In the FE model for this thesis, the monopile welds are not accounted for, and a linear buckling analysis is therefore assumed to provide quite unrealistic results. Therefore, buckling was not investigated in the ultimate limit state (ULS) assessment. Instead, a brief analysis on yield was performed.

For ULS analyses, DNV (2014) suggests using extreme load values from a 50 year return period. These were listed earlier in Table 8.5. Design load case (DLC) 6.1a from the IEC standard (2009), was selected as a basis for the ULS consideration. This corresponds to an extreme turbulence model with $U_{hub} = 0.95U_{ref}$ and an extreme sea state with $H_s = 1.09H_{s,50}$. In total, 20 time-domain analyses in 3DFloat were performed, whereupon 10 included only wave loads, and 10 only wind loads. The sum of the maximum values for both isolated cases were selected to be used for the ULS assessment. The loads are provided in Table 8.10.

Table 8.10: ULS loads.

	Only wind		Only waves		Total	
	H_x [MN]	M_y [MNm]	H_x [MN]	M_y [MNm]	H_x [MN]	M_y [MNm]
Maximum	1.2	109.5	2.6	47.6	3.8	157.1
St. dev.	0.2	18.3	0.3	6.9		

The IEC standard (2009), states to include currents, however, studies by Velarde (2016) indicate that the currents contribute little to the total loads in a ULS consideration, and it was therefore neglected in this analysis. The obtained ULS loads presented in Table 8.10 corresponds well to those obtained by Laszlo et al. (2017), however slightly lower.

Figure 8.24 plots the resulting stresses along the pile for the three geometries. The figure indicate that they all remain within the yield limit of S355 steel, which yields at 355MPa. Thus indicating that they will not yield under the applied ULS loads.

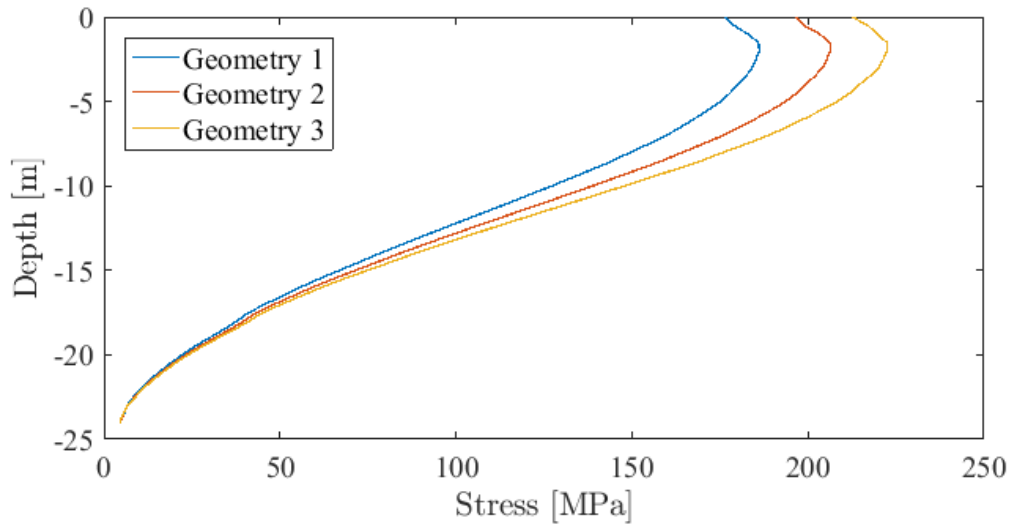


Figure 8.24: Stress along pile under ULS loads.

The results indicate that all geometries are within the yield limit, with a good margin, and it is therefore believed that they would survive an extreme event. There are of course many limitations to this assessment, and the IEC standard (2009) lists many additional DLCs for ULS considerations. A more thorough ULS analysis should be performed before concluding on survival, however this is beyond the scope of this thesis.

8.7.6 Calibration Sensitivity

The macro-element model was calibrated based on an Abaqus model, as well as an equivalent PLAXIS model. The resulting fatigue damage at the mudline for Geometry 1 is plotted in Figure 8.25, for the two calibrations.

The estimated fatigue design lifetimes were as provided in Table 8.11.

Table 8.11: Expected Fatigue life for the different calibrations of the macro-element.

FE program for calibration	Fatigue life (years)
Abaqus	35.5
PLAXIS	35.1

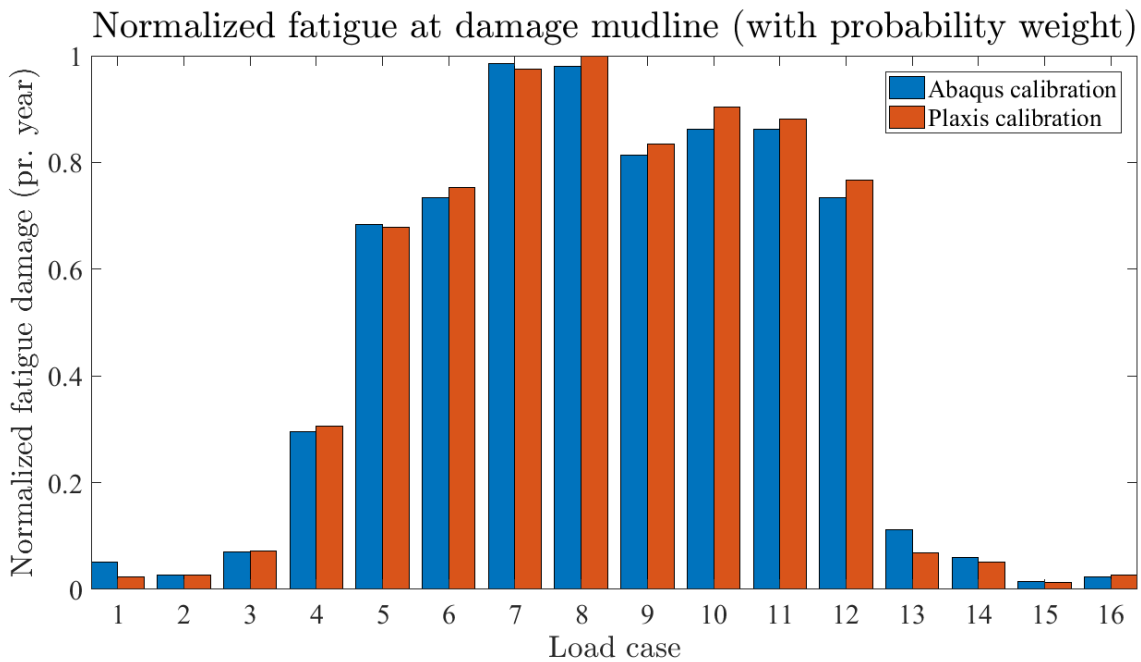


Figure 8.25: Normalized fatigue damage at the mudline for the different calibrations of the macro-element.

Between the two calibrations, the obtained expected fatigue life at the mudline was, in fact, only 1.1% larger for the Abaqus model. This indicates that the fatigue calculations are not too sensitive to the choice of FE program for calibration of the macro-element model.

In the analysis presented in the next chapter, the macro-element model was calibrated by a PLAXIS model. Supported by these results, this should not affect the fatigue damage estimates.

8.8 Summary

The purpose of this analysis was to investigate the optimization potential of a monopile OWT foundation, based on fatigue assessments. Following is a summary of the main findings with regards to this objective.

The analysis indicated that the industry practice of using API $p - y$ curves in fatigue calculations, may grossly overestimate the fatigue damage on the structure. Applying the macro-element model, which has shown to be able to reproduce results by field tests and finite element analysis, resulted in an estimated fatigue design life of 89.8% longer than the estimates by the API $p - y$ model. A large optimization potential was therefore recognized.

The two models provided identical modeling of the OWT extending above the mudline, with the same definition on structural damping, and applied the exact same environmental

load histories. It was therefore understood that the differences in the estimated fatigue damage occurred due to the differences in the foundation modeling, especially with regards to foundation stiffness and damping. In general, the idling cases showed to be more sensitive to the foundation performance than the operating cases.

The fatigue calculations along the monopile foundation indicated to be of importance in design considerations for optimization, as it contributes to reliability in the design, especially regarding weld positioning. Based on the same fatigue damage at the mudline, the magnitude of the maximum estimated fatigue damage along the pile foundation was 18% lower, when applying the more reliable $p - y$ curves, extracted from FEA, as compared to the API $p - y$ curves. Additionally, it was observed that the position of the maximum estimated fatigue damage along the pile foundation varied between the two $p - y$ formulations. Thus, not only will a more accurate model reduce the predicted fatigue damage, allowing for reductions in geometrical parameters, but also ensure a safer positioning of the monopile welds.

The suggested new geometries showed large optimization potentials of the monopile. By trusting that the macro-element model obtained the most accurate fatigue estimates, particularly for the idling cases, possible steel savings on the monopile geometry in the range of 10 - 17% were recognized in this analysis.

The lower fundamental frequency of the API $p - y$ model was, by this analysis, believed to be the main contributor to its excessive fatigue damage estimates, as compared to the macro-element model. Optimal and reliable design is therefore understood to be obtained by a foundation model that is able to provide good predictions of the fundamental frequency of the support structure. The contribution of soil damping was also recognized, however, it was difficult to quantify its isolated contribution.

Chapter 9

Real Site Analysis

The previous chapter indicated a large optimization potential for the monopile foundation through using the macro-element model in design. However, the optimization potential is only realistic if the model is accurately estimating the dynamic response, loads, and particularly the foundation stiffness and natural frequencies of the support structure. The purpose of this chapter is therefore to validate the macro-element model by comparing measured data to simulated data of a monopile-based OWT situated in the North Sea. In addition, fatigue assessments at the mudline were performed for this OWT, with a focus on the influence of soil damping to the accumulated damage.

9.1 Method

Similarly to the analysis presented in Chapter 8, integrated time-domain simulations in 3DFloat were used to obtain the response and loads at the mudline. The structural model in 3DFloat was provided by Jacobus B. De Vaal and Tor Anders Nygaard at IFE, and has been modified to represent the three foundation models studied in this analysis. The macro-element was, for this analysis, calibrated from a PLAXIS model by PhD candidate Ana M. Page at NTNU/NGI.

The structural damping of the system had to be assumed. According to Shirzadeh et al. (2013), the structural damping ratios of monopile OWTs are typically ranging between 0.5% - 1.5%, where the lower limit correlate to pure material damping. In accordance with their study, a structural damping ratio of 0.6% was used in this analysis.

This analysis assumed the same environmental conditions as in the previous analysis, and the reader is referred to Table 8.4 for a list of the different load cases. The wind was, as with the previous analysis, described through turbulence files generated with TurbSim. The Power Law was used to describe the wind shear, and Kaimal spectra were used in describing the turbulence. The waves were described through JONSWAP spectra.

In evaluation of the accuracy of the three models, focus has been set on the natural frequencies. These were estimated both from PSDs of the mudline moments, and through eigen analyses in 3DFloat, and were compared against measured data provided by Karin Norén-Cosgriff at NGL.

The fatigue damage at the mudline was calculated for two of the models to investigate the sensitivity to foundation modeling on the fatigue damage, in particular regarding the effect of accounting for soil damping. The process of calculating the fatigue damage was, as in the previous analysis, based on the recommended practice by DNV GL (2016).

9.2 Model Description

The three different models considered in this analysis were:

- The macro-element model, applying the macro-element at the mudline.
- The API p - y model, applying API p - y curves along the length of the pile foundation
- The FEA p - y model, applying p - y curves extracted from a finite element analysis, along the length of the pile foundation.

Figure 9.1 compares the load- and displacement distributions for the two p - y models to the FE results from PLAXIS.

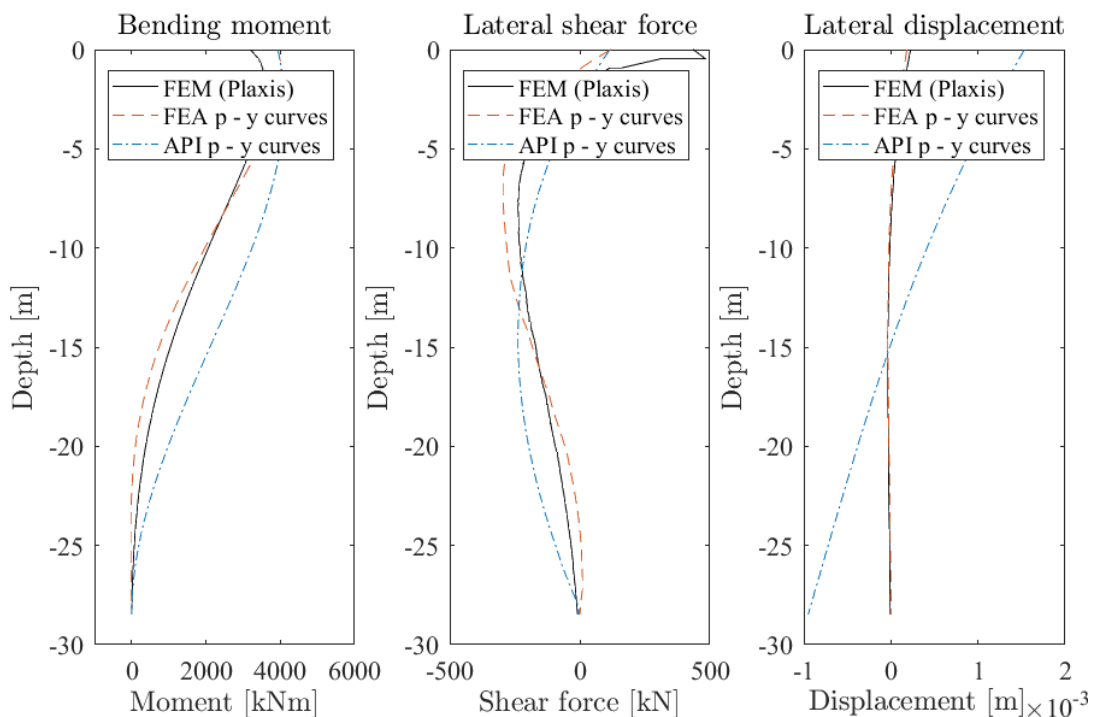


Figure 9.1: Comparison of the results from FEA to the two p - y formulations.

The FEA p - y curves were extracted from the PLAXIS model, from loading combinations corresponding to $M/H = 0$ and $M/H = \infty$. The figure above plots the result to a load combination of $M/H = 30m$, validating the usefulness of the FEA p - y curves to other loads than those extracted from. As seen by the figure, the FEA p - y model, are providing a more accurate representation of the pile response, particularly in the pile stiffness, as compared to the API p - y model.

9.3 Assumptions and Simplifications

The same assumptions and simplifications of the previous analysis, regarding the fatigue calculations and the load cases, apply to this. In short summary these include:

- Disregarding the axial force in the fatigue calculations
- Assumptions on the choice of S - N curve for the fatigue calculations
- 16 load cases, represented by 10 minute simulations, that are repeated throughout the entire design life of the structure
- Assumptions on the structural damping of the system
- Only one seeding of each load case
- The wind and wave loads remain in the same direction throughout the entire design life

Additionally, the measured data used in this analysis was obtained from only one turbine, which was limited to idling conditions.

9.4 Results and Discussion

9.4.1 Comparison Between Simulations and Measurements

Figure 9.2 plots the mudline displacements of the pile versus the applied moments at the mudline. Clearly, the API p - y curves are providing a much too soft response, as also observed by the excessive displacements in Figure 9.1.

The stiffness at the mudline is directly related to the natural frequencies of the support structure, leading to an expectancy of lower tower-bending natural frequencies for the API p - y model, as compared to the other two models.

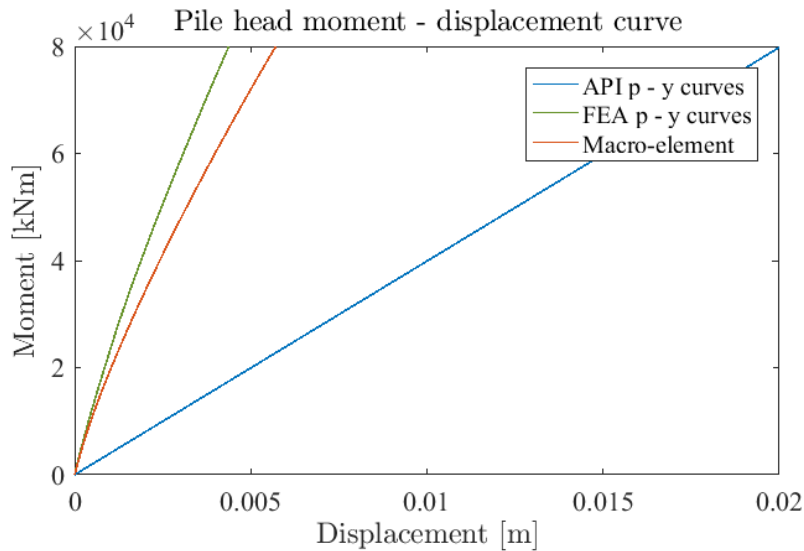


Figure 9.2: Moment - displacement curve at the mudline.

Estimations of the natural frequencies, and corresponding modes, of the three models were obtained from eigen analyses in 3DFloat. Figure 9.3 plots the power spectral densities (PSDs) of the measured accelerations, provided by Karin Norén-Cosgriff at NGI. Included on this plot, are vertical lines corresponding to 10 first simulated natural frequencies obtained for the macro-element model.

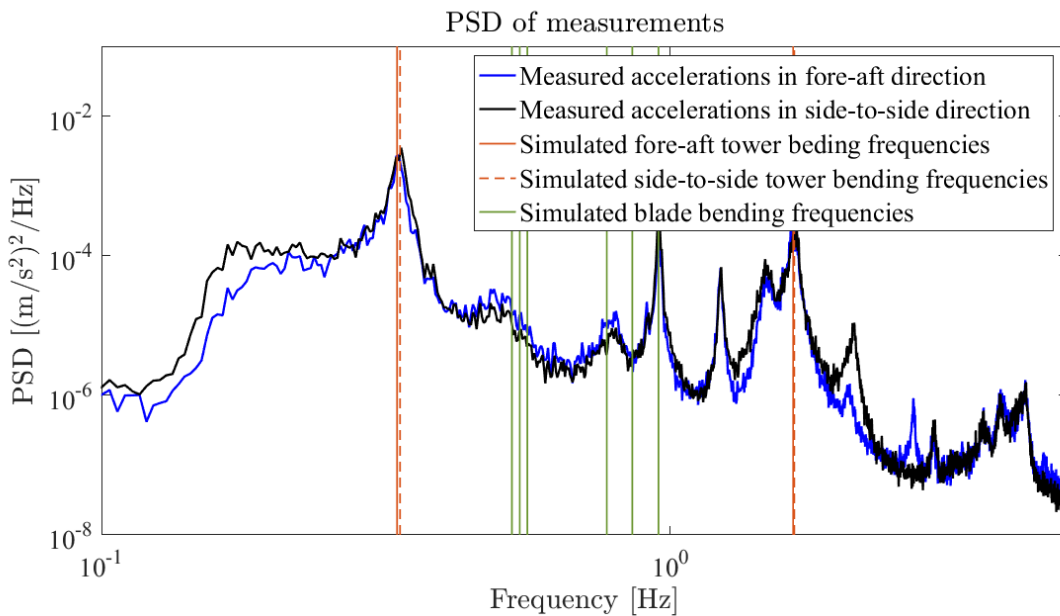














Figure 9.3: PSD of the measured accelerations at site versus simulated natural frequencies from the macro-element model.

The natural frequencies that directly relate to the foundation modeling, are the tower-bending frequencies. These are listed and visualized for the three models, in Table 9.1, together with the measured values. A table containing the measured and simulated natural

frequencies for the blade modes can be found in Appendix E.

Table 9.1: Comparison between the measured and the simulated natural frequencies for the first two tower modes.

	Measured freq. (Hz)	Simulated freq. (Hz)			Simulated modes		
		API p-y curves	FEA p-y curves	Macro- element model	Front view	Side view	Top view
1 st Sup. Struct. FA	0.332	0.298	0.336	0.331			
1 st Sup. Struct. SS	0.336	0.30	0.341	0.335			
2 nd Sup. Struct. FA	1.650	1.357	1.595	1.649			
2 nd Sup. Struct. SS	1.650	1.371	1.597	1.654			

FA = fore-aft
SS = side-to-side

The deviations from the measured frequencies are listed in Table 9.2.

Table 9.2: Measured vs. simulated tower-bending frequencies.

Mode	$f_{n,measured}/f_{n,simulated}$		
	Macro-element	FEA p - y curves	API p - y curves
1 st Sup. Struct. FA	1.003	0.988	1.114
1 st Sup. Struct. SS	1.003	0.985	1.120
2 st Sup. Struct. FA	1.001	1.033	1.217
2 st Sup. Struct. SS	0.998	1.033	1.203

These results indicate that the macro-element model is most accurate in predicting the

natural frequencies of the support structure. It is also important to note that the FEA p - y curves are, in fact, providing good estimations of the natural frequencies as well, whereas the API p - y curves are under predicting all natural frequencies related to the support structure by more than 10%. The deviations obtained for the API p - y model to the measured data, noted in Table 9.2, corresponds well with observations by Kallehave et al. (2015), where the estimated design frequency compared to measured data for 400 monopile-based OWTs, typically had $f_{0,measured}/f_{0,simulated}$ ranging from 1.0 - 1.2.

Figure 9.4 illustrates the accuracy of the predicted fundamental frequency in the fore-aft direction for the three models, by a comparison with the PSD from the measurements.

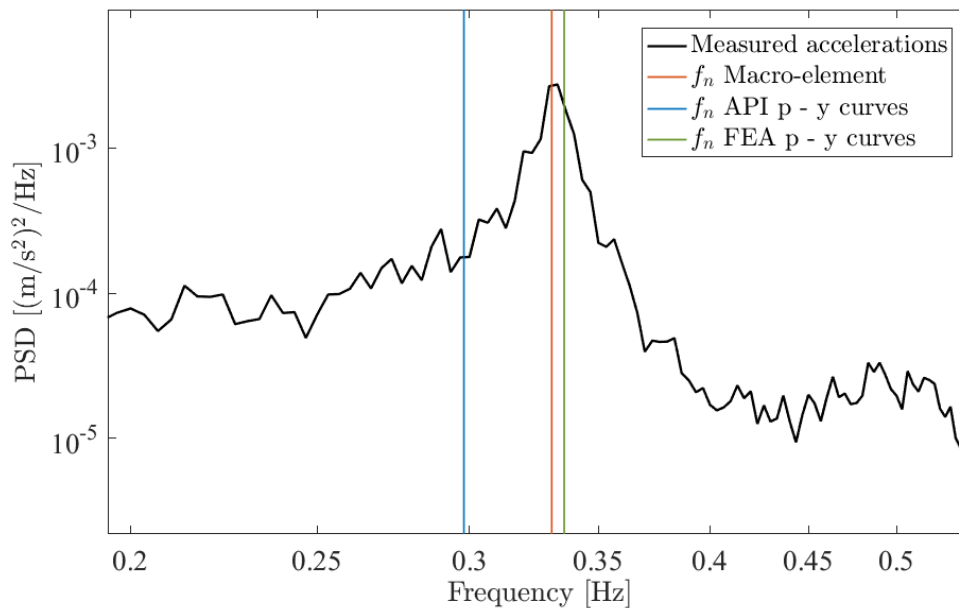


Figure 9.4: PSD of the measured accelerations in the fore-aft direction, and the corresponding fundamental frequencies of the three models.

The limited accuracy of the API p - y curves are an important observation, as they are much used in the industry for design of monopile-based OWTs. For this particular installed OWT in the North Sea, the API p - y curves were seen to under predict the measured fundamental frequency by 10.2%. If the support structure and foundation is designed based on this estimation, some issues may arise.

The first issue is the possibility of excessive material usage. As the analysis presented in Chapter 8 indicated, such an under prediction of the fundamental frequency may grossly over estimate the fatigue damage on the OWT support structure. Consequently, overly conservative dimensions are needed to obtain the desired fatigue life predictions.

Another important aspect is that the rotor, blades and structure for OWTs are designed to avoid resonance coincidence (Shirzadeh et al. 2013). By designing the support structure to such an under prediction of the resonance frequency, the actual fundamental frequency

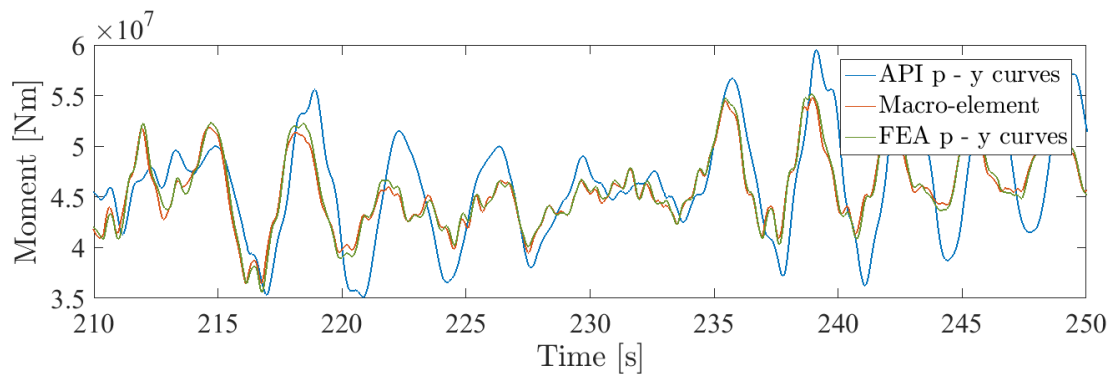
of the structure might enter into the designed range of 3P. This will have the turbine endure resonance, thus causing large amounts of cyclic damage on the structure.

9.4.2 Fatigue Assessment

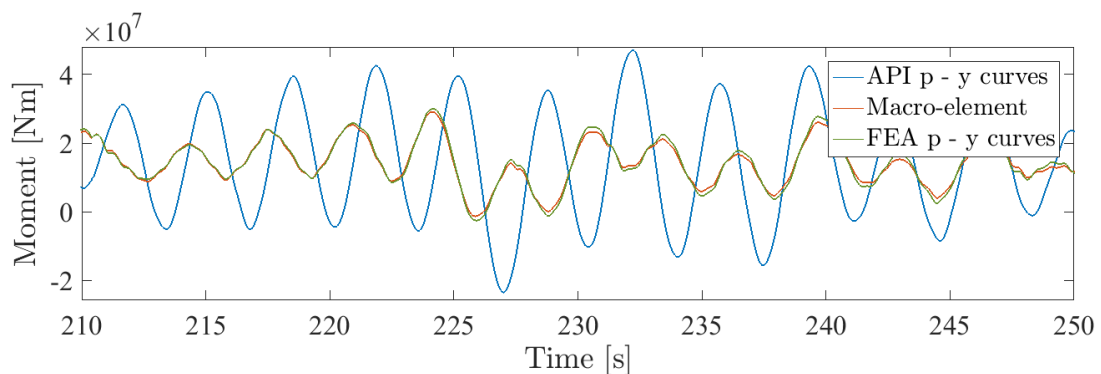
The comparison with the measured data suggests that both applying the macro-element model and the FEA p - y model, would quite accurately predict the natural frequencies of the support structure. Based on the observations of the natural frequencies' significance to the estimated fatigue damage, as seen from the previous chapter, it is believed that both the macro-element model and the FEA p - y model are useful for improved fatigue estimations, as compared to the API p - y model. This section will present observations on the resulting mudline moments and damping, and then proceed to present the fatigue calculations.

Mudline Moments

Figure 9.5a and 9.5b plots captions of the simulated mudline moments in the fore-aft direction for load case 5 (operating) and 15 (idling), respectively.



(a) Simulated mudline moments for load case 5 (operating).

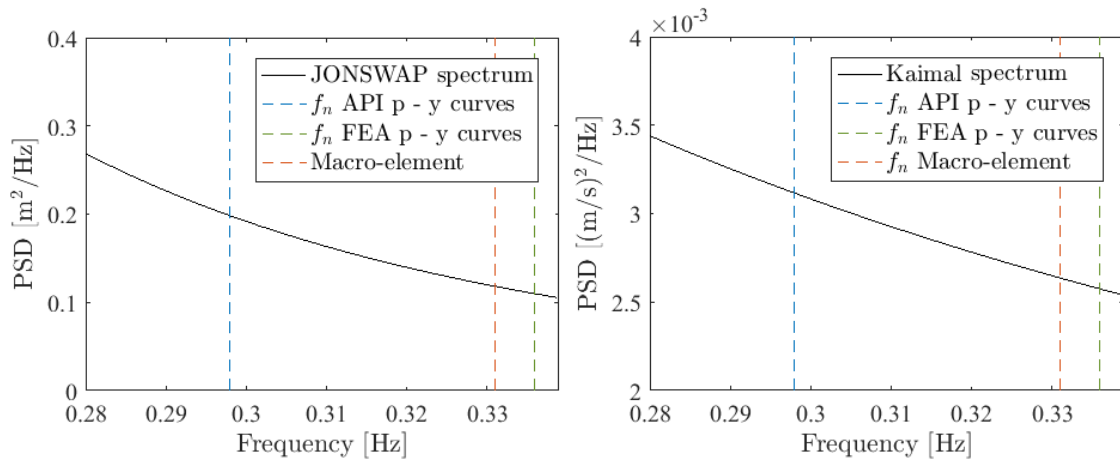


(b) Simulated mudline moments for load case 15 (idle).

Figure 9.5: Simulated mudline moments.

Figure 9.5a correspond to a turbine under power production, and is useful for illustrating the general observation for the operating cases. The macro-element model and the FEA p - y model obtained a similar moment response, however slightly larger in amplitudes for the FEA p - y model. In contrast, the API p - y model obtained significantly larger amplitudes of the mudline moments.

In Figure 9.5b, the turbine is parked and the figure illustrates the general observation for the idling cases. The obtained response was smoother for all models, mostly causing vibrations at the support structures' fundamental frequency. As the figure illustrates, the amplitudes were much larger for the model applying API p - y curves. This is as expected, due to the lower natural frequencies of this model. For the model applying API p - y curves, the support structure will endure larger amounts of excitation of its fundamental frequency from the wind- and wave loads, as seen from the captions of the environmental spectra, plotted in Figure 9.6.

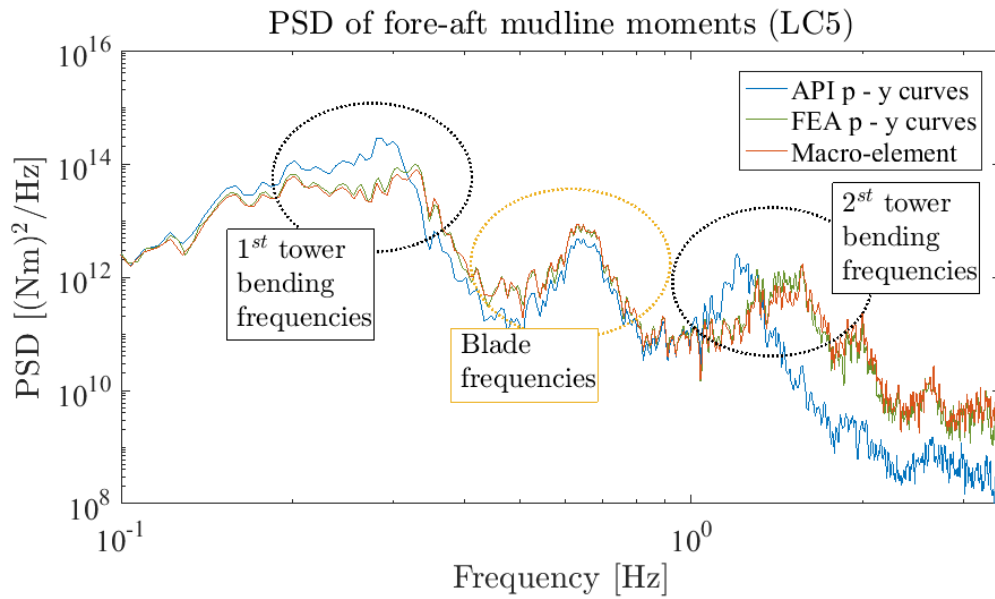


(a) Caption of the JONSWAP spectrum for load case 15. (b) Caption of the Kaimal spectrum for load case 15 .

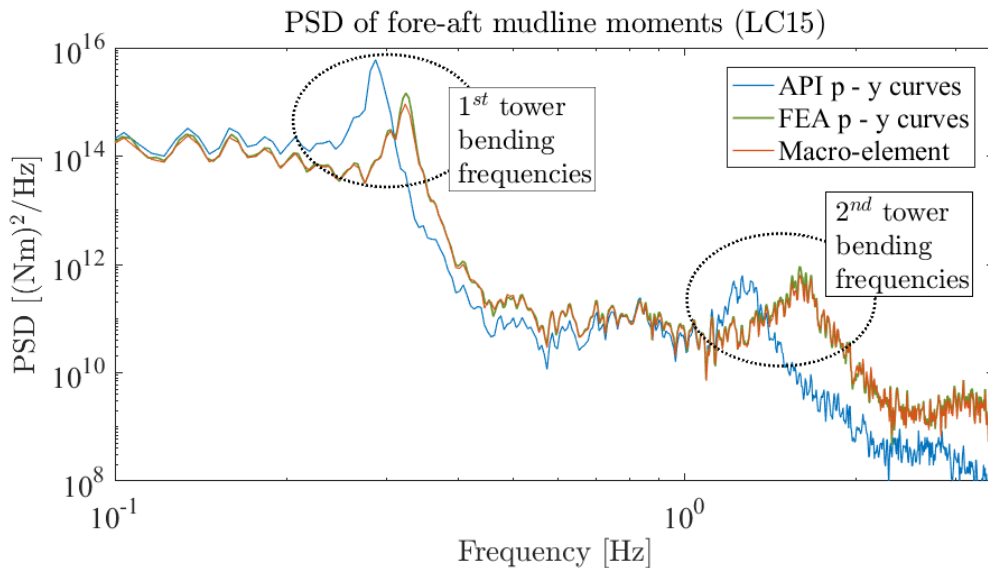
Figure 9.6: Captions of environmental spectra for load case 15.

Between the FEA p - y model and the macro-element model, the stiffness at the mudline was approximately equal, resulting in a very similar moment response at the mudline. However, slightly lower amplitudes were obtained for the macro-element model, as it includes soil damping in its formulation.

Figure 9.7a and 9.7b plots the PSDs of the mudline moments for load case 5 and 15, respectively. The PSDs illustrate the observations already commented. The more obvious peak at the first tower-bending frequencies in Figure 9.7b as compared to Figure 9.7a, indicate that the idle case is obtaining more excitation of this frequency for all models, however larger for the API p - y model than the other two.



(a) PSD of the fore-aft mudline moments for LC7 (operating).



(b) PSD of the fore-aft mudline moments for LC15 (idle).

Figure 9.7: PSD of the mudline fore-aft bending moments.

Additionally, the effect of including soil damping in the foundation models becomes visible from the lower peaks for the macro-element model as compared to the FEA p - y model. Note that the figures are plotted on a log-scale.

It may also be worth noting that the blade frequencies are only excited for the operating case, and are equally represented in all models. This underlines that the foundation model does not affect the blade modes.

Damping

Both the macro-element model, and the models that are applying p - y curves are similar in that they are providing a non-linear representation of the soil-foundation response. However, between the three, only the macro-element model include soil damping in its formulation. The hysteretic damping contribution from the soil is load dependent, and will be larger for higher loads. Figure 9.8 plots a caption of the obtained mudline moments from a free vibration test. Note that the initial bending moment prior to releasing the displacement, was largest for the FEA p - y model, and lowest for the API p - y model, as these were the stiffest and softest models, respectively. Hence, the variable amplitudes between the models, that the figure is showing.

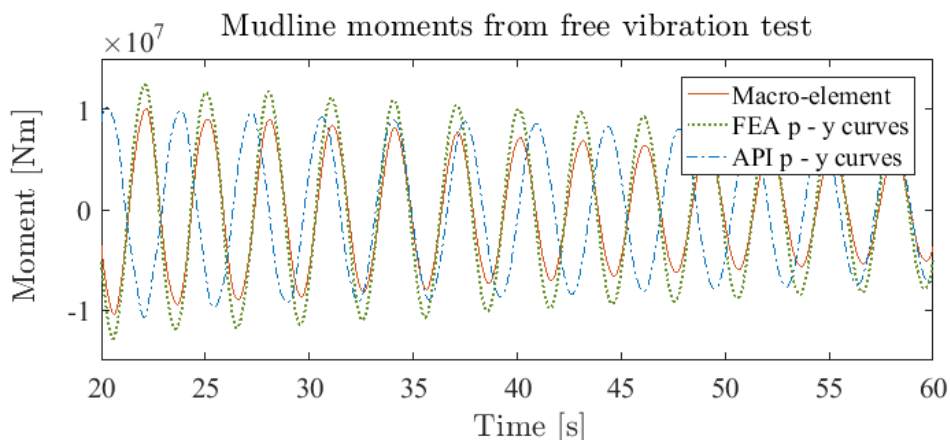
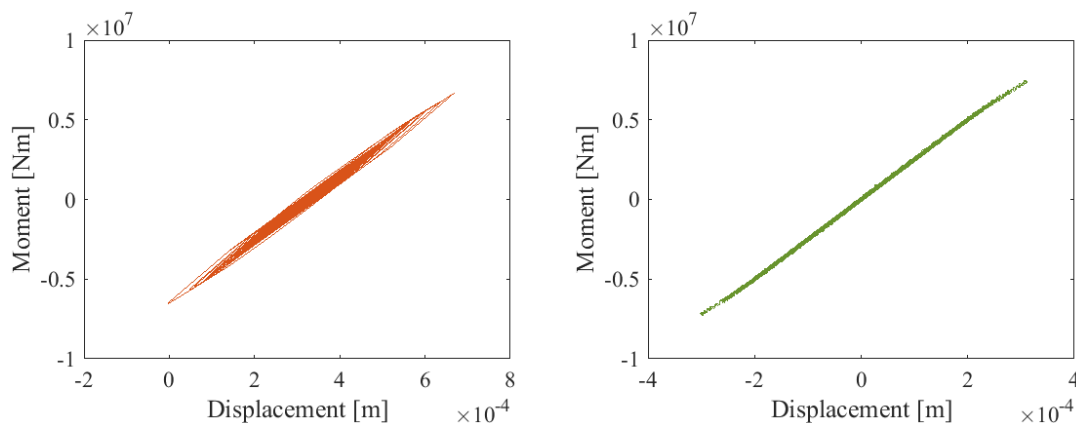


Figure 9.8: Mudline moments from free vibration test.

The Hysteretic damping contribution of the macro-element model becomes clear when plotting the resulting mudline displacements to the mudline moments. Figure 9.9a and 9.9b plots this for the macro-element model and the FEA p - y model, respectively.



(a) Mudline moments and displacements for the macro-element model. (b) Mudline moments and displacements for the FEA p - y model.

Figure 9.9: Mudline moments and displacements, illustrating the load-displacement paths of the macro-element model and the FEA p - y model.

As the figures indicate, the macro-element model is producing hysteretic loops upon loading and unloading, whereas the FEA p - y model is loaded and unloaded along the same path.

By use of the logarithmic decrement of the free vibration test, the total damping ratio of the first mode, was found for various amplitudes of the mudline moments. Figure 9.10 plots the resulting damping ratios for the three models. In the free vibration test, the blades were pitched out of the wind, and the aerodynamic contribution to the damping should therefore be negligibly small. However, in the time-domain simulations for the fatigue calculations, the total damping ratio is expected to vary between the load cases, due to variations in wind- and wave conditions. Hence this plot is mainly to provide a visualization of the trend, and not to provide a set value for the damping on the structure.

There are two important observations to note from Figure 9.10.

1. For low loads, the macro-element response is elastic. This is recognized by the constant damping ratio of the macro-element at low moment amplitudes. It is first when the plastic deformations starts occurring that the macro-element is producing the hysteretic damping. As the figure indicate, the magnitude of damping from the soil is load-dependent, and increase with increasing loads. This corresponds with the observed behaviour from laboratory- and field tests (Aasen et al. 2017).
2. The p - y models obtain a constant damping ratio for all load magnitudes, as the models are non-linear elastic, and do not account for soil damping.

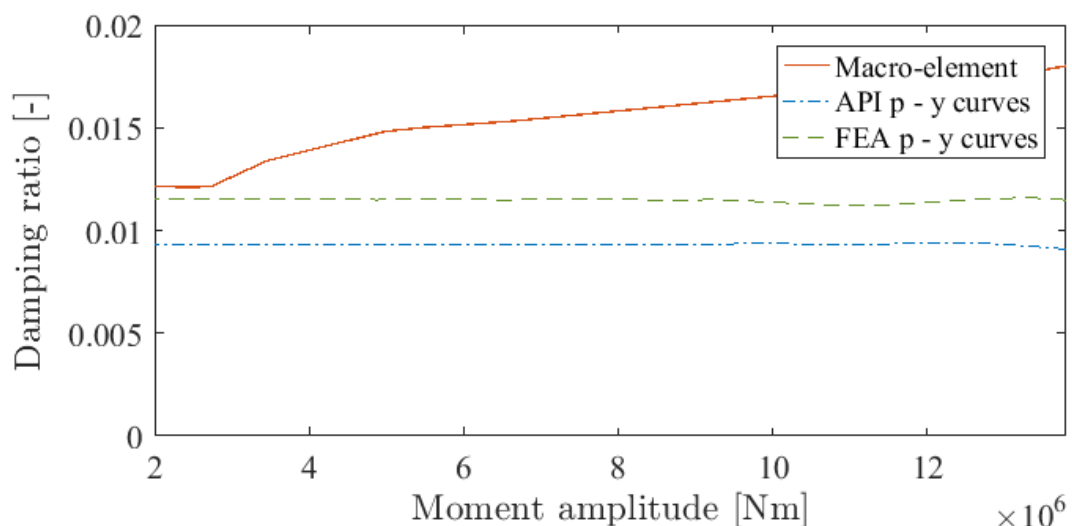


Figure 9.10: Damping ratios for various moment amplitudes at the mudline.

According to Shirzadeh et al. (2013) and Damgaard et al. (2012), the total damping of OWTs can be approximated as a linear combination of the contribution from all sources of damping on the system. As the three models were situated in the same environment,

modeled identical above the mudline, and defined with the same ratio for the structural damping, it was therefore expected that they would obtain approximately the same value for the total damping ratio in the elastic region of the macro-element model. However, this was not the obtained response, as the figure indicate. It is believed that the deviations seen in the p - y models was due to limitations on the constraints along the foundation. The focus of the fatigue analysis, however, has been on comparing the FEA p - y model and the macro-element model. Between those, the initial deviation was insignificant as compared to the contribution from the soil damping in the macro-element. The possible error in the damping ratio is therefore expected not to have a profound effect on the fatigue results.

Fatigue Calculations

The focus of the fatigue calculations has been on the two models that showed good accuracy in estimating the measured natural frequencies. These were the macro-element model and the FEA p - y model. As the simulated natural frequencies between two models were approximately equal, the fatigue damage comparison of the two, will provide an indication of the significance of including soil damping in the model formulation.

The resulting normalized fatigue damage and life expectancy at the mudline is presented in Figure 9.11 and Table 9.3 respectively. The expected fatigue life has been normalized to the estimated value for the macro-element model.

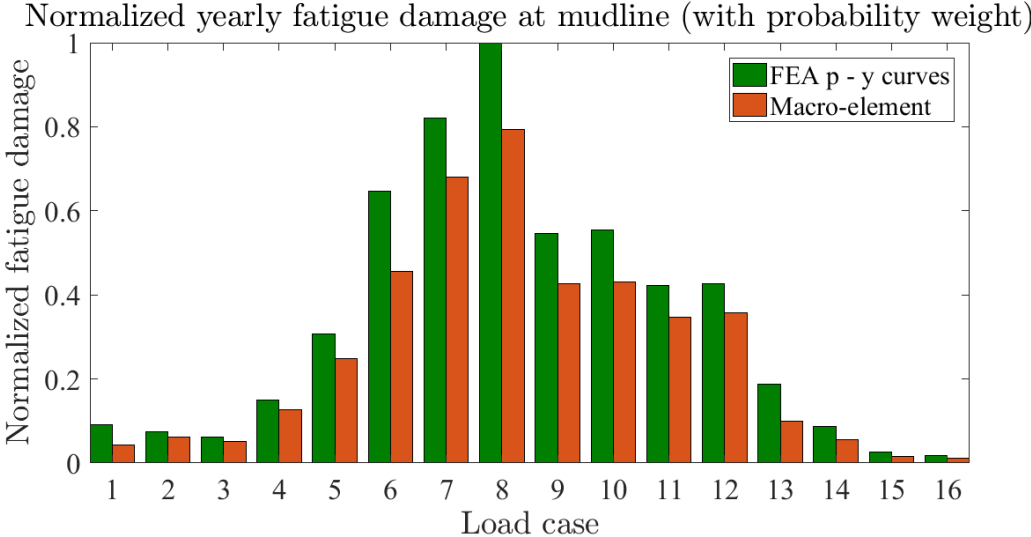


Figure 9.11: Normalized fatigue damage at the mudline.

Table 9.3: Expected fatigue life normalized by the results from the macro-element model.

	Macro-element	FEA p - y curves
Normalized fatigue life	1	0.776

From Table 9.3, it is observed that by excluding soil damping in the model formulation, the estimated fatigue life of the support structure was reduced by 22.4%. The results therefore indicates that including soil damping may be of great importance to exploit the optimization potential of the foundation and support structure. This corresponds to observations by Aasen et al. (2017), where by including a factor of 0.3% of soil damping, the fatigue damage estimates were reduced by 13%. With the fundamental frequencies close to the excitation frequencies of the waves, small differences in the damping may, as these results indicate, be of significance to the estimated fatigue life expectancy.

An overview of which load cases that are most sensitive to the foundation performance with regards to damping, can be obtained by plotting the deviations in the estimated fatigue damage between the two models. Figure 9.12 presents this comparison.

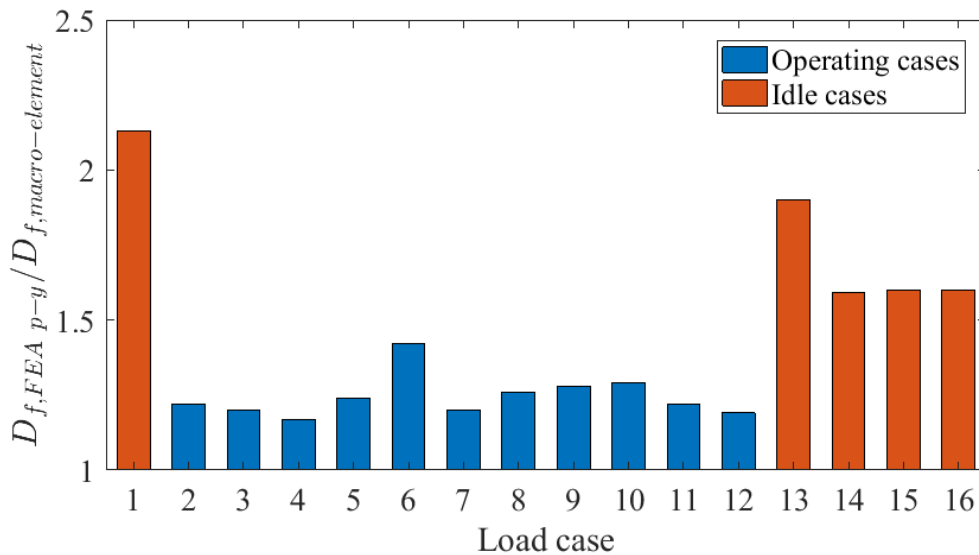


Figure 9.12: Deviation from the obtained fatigue damage for the FEA p - y model to the macro-element model.

The figure indicate, in accordance with observations by Aasen et al. (2017), that the importance of including soil damping was, in general, more significant for the idling cases.

9.5 Summary

In the comparison with the measured data from the installed OWT in the North Sea, the macro-element model showed to be most accurate in predicting the measured natural frequencies of the support structure. In fact, the macro-element model only under predicted the fundamental fore-aft tower-bending frequency by 0.3%, whereas the industry practice of using an API p - y model showed to under predict this by 11.4%.

An alternative p - y model, based on p - y curves obtained from FEA, also provided good estimates on the natural frequencies of the support structure, however somewhat less accurate than the macro-element model.

Soil damping has been observed in laboratory- and field tests, and the reliability of a foundation model is increased when accounting for this. By comparing the two models with equivalent natural frequencies, a 29% longer fatigue life expectancy was obtained for the model that included soil damping in its formulation. The fatigue calculations thus indicated that including soil damping in the foundation model, may be of significance to the reliability of the results, and consequently for exploiting the optimization potential.

A general observation was that the response of the OWT was more sensitive to the foundation performance in the idling cases. This was highlighted by the larger deviations in the moments obtained at the mudline as well as the fatigue estimates.

Chapter 10

Conclusion

Offshore wind energy has experienced a fast growth over the recent years, however limited by the excessive costs as compared to its onshore counterpart. Cost reductions in the reliability of the design are therefore crucial for a further development of the industry. The common industry practice of analyses and design optimization of monopile-based OWTs has shown to be limiting in its application, and more accurate models are needed. In the light of this, the two main objectives of this thesis has been the following:

- To assess the accuracy of different foundation models.
- To study the optimization potential of monopile OWT foundations, with regards to fatigue damage estimates.

10.1 Conclusion

This section will conclude the main findings regarding the thesis objectives.

Assessment of Model Accuracy

From the comparison with the measured natural frequencies presented in Chapter 9, it is concluded that, between the models investigated, the macro-element model is the most accurate in reproducing the measured response. In fact, the largest deviation to the measurements of the four first tower bending frequencies simulated by the macro-element model, was of 0.3%. Hence, the model was recognized as, not only the most accurate of the ones studied, but very accurate indeed.

The p - y curves extracted from FEA also provided good predictions of the measured natural frequencies, however slightly less accurate than the macro-element model. For the two first tower bending frequencies (1th fore-aft and side-to-side), the maximum deviation

from the measurements was of 1.5%. Larger deviations were obtained for the second bending modes (2nd fore-aft and side-to-side), where the maximum deviation from the measurements was of 3.2%.

The model that showed to be the least accurate in predicting the measured natural frequencies, was the API p - y model. This is also the model that is commonly used in the industry today. The comparison with the measured data showed the model to under predict the measured natural frequencies by 10.2% and 10.7% for the first fore-aft and side-to-side bending modes respectively. The second fore-aft and side-to-side bending modes from the simulations were under predicted by as much as 17.8% and 16.9% to the measurements. Hence concluding that the API p - y model was, by far, the least accurate of the ones studied in this thesis.

With regards to damping, it was recognized in Chapter 9 that only the macro-element model was able to reproduce a load-dependent hysteretic foundation damping as observed in field- and laboratory tests. It was therefore concluded to provide the most realistic representation of the total damping on the OWT support structure.

Fatigue Estimates and Optimization Potential

This thesis has indicated how accurate predictions of natural frequencies and damping are crucial for the reliability of the fatigue life estimations. The co-occurring difference in foundation stiffness and damping between the two models investigated in Chapter 8, resulted in an increase of the estimated fatigue life by 89.8%, through applying the macro-element foundation model. As the two models were identically described above the mudline and exposed to the same load-histories, it was concluded that the differences in the fatigue estimates was due to the difference foundation performance. In general, the monopile-based OWTs studied in this thesis were more sensitive to the foundation performance under idling conditions.

The macro-element model was concluded to provide the most realistic representation of the total damping on the support structure. Between two models with equivalent fundamental frequencies, a larger fatigue life expectancy of 29% was obtained for the macro-element model, indicating the significance of correct representation of damping to the fatigue estimates. Yet, with regards to foundation modeling, accurate predictions on the natural frequencies was still recognized as of highest significance in obtaining reliable and optimal design.

It was also concluded that considering the fatigue damage along the pile foundation may be of significance in optimization of the monopile design, as it will provide reliability to the positioning of the welds, as well as a guidance upon designing for a depth dependent geometry. Suggestions on new monopile geometries of the OWT studied in Chapter 8, recognized potential of steel savings on the monopile ranging from 10 - 17%, by applying

the macro-element model.

General Conclusion

This study has shown that, by use of the macro-element model in foundation design and optimization, large potentials for cost reductions in the industry may be achieved. Not only did the estimated fatigue damage decrease with the macro-element model, but the reliability of the estimations were larger due to the more accurate performance of the foundation model. Thus, by applying the macro-element in design, cost reductions may be obtained both in optimization of the geometries, as well as cost reductions relating to the reduced risks.

10.2 Suggestions for Further Work

The complexity of foundation design for OWT applications are of a much larger scope than has been presented in this thesis. This study involve many limitations, and there are therefore many suggestions for further work, some of which are listed in this section.

- The main focus of this thesis has been on monopile-based OWTs on soil conditions dominated by clay. The macro-element model is yet to be tested for sites dominated by sandy soils, and a study on its performance on a sand-dominated site would be a suggestion for further work.
- A significant limitation to this study was the uncertainties and assumptions made on damping. A more comprehensive study on damping is therefore a natural continuation of this work. According to Kallehave et al. (2015), the overall structural damping on OWTs contain large uncertainties and are difficult to quantify. Yet, the choice of design values may be of significance to the fatigue estimates. Therefore, to include more confidence in the design calculations, a sensitivity study to the estimated fatigue damage for various values of the structural damping is suggested as an extension of this study. Additionally, a comparison with predictions and measurements of the damping on OWTs is of interest as an inclusion to the suggested further work on damping.
- The fatigue analysis in this theses was only performed for idling and production cases. The IEC standard (2009) suggests, as well, fatigue considerations under start up, shut down and under the occurrence of faults. For a more thorough fatigue analysis, these conditions could have been included, to see if their impact on the life estimations are significant.

- Research has indicated that different seeding of the wind- and wave stochastics may cause significant variations on the response of the OWT (Stewart et al. 2015). In this thesis, the fatigue calculations were intended as a comparison between different models, and only one seeding for each load case was considered. However, an improved fatigue assessment is suggested as an extension to this study, upon which more seedings should be evaluated to ensure a fatigue assessment that is seeding independent.
- Another significant limitation to this study was that the wind- and waves remained uni- and co-directional throughout the entire design life of the structure. However, in reality the wind- and wave directions are constantly changing, and will at times be misaligned. As the aerodynamic damping is negligible in the side-to-side direction, disregarding the occurrence of misalignment and multi-directional loading, may result in inaccurate fatigue assessments. A study on the same models' performance under multi-directional loading is therefore suggested as further work.
- The ULS analysis of this study contained many limitations. It is clear that upon suggesting new dimensions to obtain material savings, other limit state considerations than only fatigue must be considered. Therefore, a more thorough ULS analysis should be performed as an extension to this study, as well as considerations on the serviceability limit state (SLS). This should also include considerations on shell buckling upon installing the monopile, as Kallehave et al. (2015) states this as a limiting factor on thickness design.

Bibliography

- 3D Float User Manual* (n.d.).
- Aasen, Steffen (2016). “Soil-structure interaction modelling for an offshore wind turbine with monopile foundation”. MA thesis. Norwegian University of Life Sciences.
- Aasen, Steffen et al. (2017). “Effect of the Foundation Modelling on the Fatigue Lifetime of a Monopile-based Offshore Wind Turbine”. In: *Wind Energy Science* 2.2, pp. 361–376.
- Abaqus/CAE User’s Guide* (2013).
- Abaqus/CAE User’s Guide* (2014).
- Alipour, A. and F. Zareian (2008). “Study Rayleigh Damping in Structures; Uncertainties and Treatments”. In: *The 14th World Conference on Earthquake Engineering*.
- Andersen, L. (2010). “Assessment of lumped-parameter models for rigid footings”. In: *Computers & Structures*.
- API (2011). *ISO19901-4:2003 (Modified). Geotechnical and Foundation Design Considerations*. 1st ed.
- Arany, Laszlo et al. (2017). “Design of monopiles for offshore wind turbines in 10 steps”. In: *Soil Dynamics and Earthquake Engineering*.
- Arany, László et al. (2014). “Simplified critical mudline bending moment spectra of offshore wind turbine support structures”. In: *Wind Energy*.
- Arshad, Muhammad and Brendan C. O’Kelly (2016). “Analysis and Design of Monopile Foundations for Offshore Wind-Turbine Structures”. In: *Marine Georesources & Geotechnology* 34.6, pp. 503–525.
- Beuckelaers, W. J. A. P. (2015). “Fatigue life calculation of monopiles for offshore wind turbines using a kinematic hardening soil model”. In: *Ground Engineering*, pp. 26–29.
- Brennan, Feargal and Isaac Tavares (2014). “Fatigue design of offshore steel mono-pile wind substructures”. In: *Proceedings of the Institution of Civil Engineers - Energy* 167.4, pp. 196–202.
- Byrne, Byron W. et al. (2015). *New design methods for large diameter piles under lateral loading for offshore wind applications*.
- Cao, Shuyang (2013). “Strong Winds and Their Characteristics”. In: *Advanced Structural Wind Engineering*. Springer Japan, pp. 1–25.

- Carswell, W. et al. (2015). “Foundation damping and the dynamics of offshore wind turbine monopiles”. In: *Renewable Energy* 80, pp. 724–736.
- Chakrabarti, Subrata (2005). *Handbook of Offshore Engineering*. 1st. Vol. 1. Elsevier.
- Damgaard, Mads et al. (2012). “Natural Frequency and Damping Estimation of an Offshore Wind Turbine Structure”. In: *Proceedings of the 22nd (2012) International Offshore and Polar Engineering Conference*.
- DNV (2010). *DNV-RP-C205. Environmental conditions and environmental loads - Recommended Practice*. Det Norske Veritas.
- (2014). *Offshore Standard DNV-OS-J101. Design of Offshore Wind Turbine Structures*. Det Norske Veritas.
- DNVGL (2016). *DNVGL-RP-C203. Fatigue design of offshore steel structures - Recommended practice*. Det Norske Veritas and Germanischer Lloyd.
- DNV/Risø (2002). *Guidelines for Design of Wind Turbines*. 2nd ed. DNV/Risø. ISBN: 87-550-2870-5.
- Esteban, M. Dolores et al. (2011). “Why offshore wind energy?” In: *Renew. Energ.* 36.2, pp. 444–450.
- Fischer, T., W. E. De Vries, and Björn Schmidt (2010). *Upwind design basis, WP4: offshore foundations and support structures*. Tech. rep. Endowed Chair of Wind Energy (SWE) University of Stuttgart.
- Grimstad, Gustav and Lars Andersen and Hans Petter Jostad (2012). “Ngiadp: Anisotropic shear strength model for clay”. In: *International Journal for Numerical and Analytical Methods in Geomechanics* 36.4, pp. 483–497.
- GWEC (2015). *Global Wind Report*.
- Haiderali, Aliasger and Gopal Madabhushi (2012). “Three-Dimensional Finite Element Modelling of Monopiles for Offshore Wind Turbines”. In: *Advances in Civil, Environmental, and Materials Research*, pp. 3277–3295.
- Hopperstad, Odd Sture and Tore Brøvik (2015). “Materials Mechanics Part I”. Lecture notes NTNU.
- Hoven, Isaac van der (1956). “Power Spectrum of Horizontal Wind Speed in the Frequency Range From 0.0007 to 900 Cycles per Hour”. In: *Journal of Meteorology* 14, pp. 160–164.
- IEC 61400-3: Wind turbines - Part 3: Design requirements for offshore wind turbines* (2009). International Electrotechnical Commission (IEC).
- Jonkman, B. J. and L. Kilcher (2012). *TurbSim User’s Guide: Version 1.06.00*. Tech. rep. National Renewable Energy Laboratory (NREL).
- Jonkman, Jason and W. Musial (2010). *Offshore Code Comparison Collaboration (OC3) for IEA Task 23 Offshore Wind Technology and Deployment*. Tech. rep. National Renewable Energy Laboratory (NREL).
- Jonkman, J. et al. (2009). *Definition of a 5-MW Reference Wind Turbine for Offshore System Development*. Tech. rep. National Renewable Energy Laboratory (NREL).

- Jung, Sungmoon et al. (2015). “Effect of monopile foundation modeling on the structural response of a 5-MW offshore wind turbine tower”. In: *Ocean Engineering* 109, pp. 479–488.
- Kallehave, Dan et al. (2015). “Optimization of monopiles for offshore wind turbines”. In: *Philosophical Transactions of The Royal Society A Mathematical, Physical and Engineering Sciences* 373.
- Karimirad, Madjid and Torgeir Moan (2012). “Wave- and Wind-Induced Dynamic Response of a Spar-Type Offshore Wind Turbine”. In: *Journal of Waterway, Port, Coastal, and Ocean Engineering* 138.1, pp. 9–20. ISSN: 0733-950X/2012/1-9–20.
- Kramer, Steven L. (1996). *Geotechnical Earthquake Engineering*. Pearson. ISBN: 0-13-374943-6.
- Maleque, Md Abdul and Mohd Sapuan Salit (2014). *Materials Selection and Design*. Springer. 132 pp. ISBN: 9814560375.
- Manwell, J. F., J. G. McGowan, and A. L. Rogers (2010). *Wind Energy Explained*. Wiley John & Sons. 704 pp. ISBN: 0470015004.
- Mardfekri, Maryam, Paolo Gardoni, and Jose M. Roesset (2013). “Modeling Laterally Loaded Single Piles Accounting for Nonlinear Soil-Pile Interaction”. In: *Journal of Engineering*.
- Marsh, Gabriel et al. (2016). “Review and application of Rainflow residue processing techniques for accurate fatigue damage estimation”. In: *International Journal of Fatigue* 82, pp. 757–765.
- Matlock, Hudson (1970). “Correlations for Design of Laterally Loaded Piles in Soft Clay”. In: *Proceedings of the 2th Annual Offshore Technology Conference* 1, pp. 577–588.
- Newland, D. E. (2005). *An Introduction to Random Vibrations, Spectral & Wavelet Analysis: Third Edition*. DOVER PUBN INC. 477 pp. ISBN: 0486442748.
- Page, Ana M. et al. (2018). “A macro-element pile foundation model for integrated analyses of monopile-based offshore wind turbines”.
- Perumalsamy, Kavitha, Muthu Venkatesh M., and Sundaravadivelu R. (2015). “Soil Structure Interaction Analysis of a Dry Dock”. In: *Aquatic Procedia* 4, pp. 287–294.
- PLAXIS Material Models Manual* (2017). <https://www.plaxis.com/support/manuals/plaxis-2d-manuals/>.
- Reese, L. C., W. R. Cox, and F. K. Koop (1974). “Analysis of laterally loaded piles in sand”. In: *Proceedings of the 6th Annual Offshore Technology Conference* 2, pp. 473–483.
- Reese, Lymon C., William R. Cox, and F. D Koop (1975). “Field Testing and Analysis of Laterally Loaded Piles in Stiff Clay”. In: *Proceedings of the 7th Annual Offshore Technology Conference* 2, pp. 671–679.
- Sanchez, Hector et al. (2015). “Health-aware Model Predictive Control of Wind Turbines using Fatigue Prognosis”. In: *IFAC-PapersOnLine* 48.21, pp. 1363–1368.

- Schafhirt, Sebastian et al. (2016). "Influence of Soil Parameters on the Fatigue Lifetime of Offshore Wind Turbines with Monopile Support Structure". In: *Energy Procedia* 94, pp. 347–356.
- Shirzadeh, R. et al. (2013). "Experimental and Computational Damping Estimation of an Offshore Wind Turbine on a Monopile Foundation". In: *Journal of Wind Engineering and Industrial Aerodynamics* 120, pp. 96–106.
- Stewart, Gordon M. et al. (2015). "Statistical Estimation of Extreme Loads for the Design of Offshore Wind Turbines During Non-Operational Conditions". In: *Wind Engineering* 39, pp. 629–640.
- Tempel, J. van der et al. (2010). "Design of support structures for offshore wind turbines". In: *Wind Power Generation and Wind Turbine Design*. WITPRESS LTD., pp. 559–591.
- Velarde, Joey (2016). "Design of Monopile Foundations to Support the DTU 10 MW Offshore Wind Turbine". MA thesis. Norwegian University of Science and Technology.
- Verruijt, Arnold (2006). *Offshore Soil Mechanics*. Delft University of Technology.
- (2011). *Soil Mechanics*. Delft University of Technology.
- Wang, Shih-Tower and Lymon C. Reese (1993). *COM624P - Laterally Loaded Pile Analysis Program for the Microcomputer, Version 2.0*. Tech. rep.
- Zaaijer, M.B. (2006). "Foundation modelling to assess dynamic behaviour of offshore wind turbines". In: *Applied Ocean Research* 28.1, pp. 45–57.

Appendix A

3DFloat Input File

```
!  
! 3dfloat test input file for a 5MW NREL MONOPILE  
! Created by: JB de Vaal  
! Modified by: Veronika Næss  
!   updated: 04.11.17 VN  
!  
! Modifications by VN has been done in this section  
! Notes by VN
```

```
! -----  
! SET ENVIRONMENT:  
! -----
```

```
set_environment  
gravity:          on  
buoyancy:        on  
rho_water:       1025.0001  
rho_air:         1.225  
nu_water:        0.00001000  
nu_air:          0.00000100  
waves:           irregular_waves  
tshift_waves:    10.  
wave_ramps:      0.  
wave_rampe:      100.  
!wave_amplitude: 1.70  
!spectral_peak:  5.88  
wave_direction:  0.  
depth:           20.  
norder           -1  
surface_option:  2ndorder  
kinematics_option: initial  
dtwkin:          -1.  
pre_computed_waves_file: off  
hydro_force:     morison  
current_speed:   0.  
current_exponent: 0.  
current_direction: 0.
```

```

! wind is setup at line 700
wind:          mean_profile
tshift_wind:   0.
wind_speed:    12.
wind_ref_height: 90.
wind_exponent: 0.14
wind_direction: 0.
wind_force:    drag

! -----
! SET UP AND TEST IRREGULAR WAVES:
! -----
!jswap_wavelets_constant hs: 1.70   tp: 5.88   tstart: 25.
tcut: -1.  gamma: 2.87
depth: 20.  file: wavelets6.txt  tperiodic: 3600. ! TAN

wavelets  scale_amplitude: 1.  file wavelets6.txt

test_irregairy dt 1.  nstep 600 x 0. 0. 0. filename waveheight.txt

wave_forces cm_morison 1.63

! -----
! MATERIALS DEFINITION:
! -----

define_material name OC4semisub          rho 7850.0   e 2.1e+13   g
7.89473684211e+12
define_material name connect_mat        rho 1e-08    e 2.1e+15   g
8.1e+14
define_material name wire_OC4           rho 24596.54 e 1.6353e+11 g
65119666311.8
define_material name massless1          rho 0.0001   e 210.e9    g
80.8e9
define_material name massless2          rho 0.0001   e 210.e9    g
80.8e9
define_material name massless3          rho 0.0001   e 210.e10   g
80.8e11
!Applied to Nacelle to avoid 3f
define_material name mainshaft          rho 0.0001   e 210.e9    g
1.05610143e9
define_material name mainshaft_stiff    rho 0.0001   e 210.e11   g
80.8e11
!Applied to mainshaft to avoid 3f
!define_material name mainshaft_stiff   rho 1000.    e 210.e11   g
80.8e11
define_material name steeltowerMassless rho 0.00001   e 2.1e+11   g
8.08e+11
define_material name steeltowerMassless2 rho 0.00001   e 2.1e+15   g
8.08e+15
define_material name steeltower2        rho 8500.    e 20.1e+11  g
80.08e+10

! -----
! STRUCTURE DEFINITION:
! -----

```

```

! -----
! MONOPILE: BELOW MUDLINE TO MUDLINE DEFINITION:
! -----
!Used when applying p - y curves along the foundation, not used for
the macro-element

!new_elements_beam1 nelem 1 material steeltower connect_mode
connect_none
!x1 0.0 0.0 -44.0 dcyll 6.00 tcyl1 0.06
!x2 0.0 0.0 -43.5 dcyll2 6.00 tcyl2 0.06 btype beam

!new_elements_beam1 nelem 23 material steeltower connect_mode
connect_1 ! p-y curves attached here
!x1 0.0 0.0 -43.5 dcyll 6.00 tcyl1 0.06
!x2 0.0 0.0 -20.5 dcyll2 6.00 tcyl2 0.06 btype beam

!new_elements_beam1 nelem 1 material steeltower connect_mode
connect_1
!x1 0.0 0.0 -20.5 dcyll 6.00 tcyl1 0.06
!x2 0.0 0.0 -20.0 dcyll2 6.00 tcyl2 0.06 btype beam

! -----
! MONOPILE: MUDLINE TO TOWER DEFINITION:
! -----

new_elements_beam1 nelem 6 material steeltower connect_mode
connect_none !connect_1 when applying p - y curves
x1 0.0 0.0 -20.0 dcyll 6.00 tcyl1 0.06
x2 0.0 0.0 10.0 dcyll2 6.00 tcyl2 0.06 btype beam

! -----
! TOWER DEFINITION:
! -----
new_body name tower reftype: inertial parent: inertial axes: normal

new_elements_beam1 nelem 20 material steeltower connect_mode
connect_1 ! TAN according to OC3 report
x1 0.0 0.0 10.0 dcyll 6. tcyl1 0.035
x2 0.0 0.0 87.6 dcyll2 3.87 tcyl2 0.024 btype beam

! -----
! NACELLE DEFINITIONS:
! -----

! yaw drive
new_body name yawdrive parent tower reftype refnode xfind 0. 0. 87.6
rotorder 123 rotation 0. 0. 0. axes normal
! yaw can be added here eg rotation 0. 0. 8.

! element to Nacelle reference point
new_elements_beam1 nelem 1 material massless1 connect_mode connect_1
x1 0. 0. 0. dcyll 4.0 tcyl1 1.
x2 0. 0. 1.9626 dcyll2 4.0 tcyl2 1. btype beam

```

```

! nacelle
new_body name nacelle parent yawdrive reftype refnode xfind 0. 0.
1.9626 rotorder 123 rotation 0. 5. 0. axes normal ! rotor tilt: 5
degrees

! shaft from main bearing to point mass 1
new_elements_beam1 nelem 1 material massless3 connect_mode
no_connect
x1 -3.1071 0. 0. dcyll 2.0 tcyll 1.
x2 -0.7968 0. 0. dcyll 2.0 tcyll 1. btype beam

! point mass 1 to nacelle reference point
new_elements_beam1 nelem 1 material massless3 connect_mode
connect_both
x1 -0.7968 0. 0. dcyll 2.0 tcyll 1. pointmass 120.e3
x2 0. 0. 0. dcyll 2.0 tcyll 1. btype beam

! nacelle reference point to nacelle CG
new_elements_beam1 nelem 1 material massless3 connect_mode connect_1
x1 0. 0. 0. dcyll 2.0 tcyll 1.
x2 1.9072 0. 0. dcyll 2.0 tcyll 1. btype beam

! point mass 2 to nacelle CG
new_elements_beam1 nelem 1 material massless3 connect_mode connect_2
x1 4.6113 0. 0. dcyll 2.0 tcyll 1. pointmass 120.e3
x2 1.9072 0. 0. dcyll 2.0 tcyll 1. btype beam

! mainbearing
new_body name mainbearing parent nacelle reftype refnode
xfind -3.1071 0. 0. rotorder 123 rotation 0. 0. 0. axes normal

! shaft from hub CG to main bearing via moment sensor

new_elements_beam1 nelem 1 material mainshaft_stiff connect_mode
no_connect ! Stiffness chosen to avvoid 3f
x1 -1.912 0. 0. dcyll 2.0 tcyll 1. pointmass
5159.11681
x2 -1.0 0. 0. dcyll 2.0 tcyll 1. btype beam
generator nrel5mwfloating !NB: have to define generator
"nrel5mwfloating"

new_elements_beam1 nelem 1 material mainshaft_stiff connect_mode
connect_both ! Stiffness chosen to avvoid 3f
x1 -1. 0. 0. dcyll 2.0 tcyll 1.
x2 0. 0. 0. dcyll 2.0 tcyll 1. btype beam

! hub
new_body name hub parent mainbearing reftype refnode xfind -
1.912 0. 0. rotorder 123 rotation 0. 0. 0. axes normal

! -----
! BLADE STRUCTURAL AND AERODYNAMIC PROPERTIES

```

```

! -----
!
! blade element structural coordinate system:
!
! y out TE          along flap principal axis
! z out suction side along lag principal axis
! x = y x z ! NB CAN THEREFORE BE TOWARDS TIP OR HUB
!
! structural twist is positive around x
! mass center and shear center offsets are given in blade element
structural
! coordinate system
!
! BLADE PROPERTIES
! -----
! distributed structural properties for blade, 5MW NREL rotor
!
r[m],eiflap[Nm**2],eiedge,gtors,ea[N],rho[kg/m],structwist[deg],flpi
nert[kgm],edginert[kgm],&
! flpcgofs[m],edgcgofs[m],flpshrofs[m],edgshrofs[m]
!
blade_table  blname nrel5mw
1.4999e+00 1.8110e+10 1.8114e+10 5.5644e+09 1.3943e+10 6.7893e+02
13.30818 972.86 973.04 0. 0.00017 0. 0.
1.6999e+00 1.8110e+10 1.8114e+10 5.5644e+09 1.3943e+10 6.7893e+02
13.30818 972.86 973.04 0. 0.00017 0. 0.
2.6999e+00 1.9425e+10 1.9559e+10 5.4316e+09 1.5055e+10 7.7336e+02
13.30818 1091.52 1066.38 0. -0.02309 0. 0.
3.6999e+00 1.7456e+10 1.9498e+10 4.9940e+09 1.3708e+10 7.4055e+02
13.30818 966.09 1047.36 0. 0.00344 0. 0.
4.6998e+00 1.5287e+10 1.9789e+10 4.6666e+09 1.3330e+10 7.4004e+02
13.30818 873.81 1099.75 0. 0.04345 0. 0.
5.6998e+00 1.0782e+10 1.4859e+10 3.4747e+09 9.9814e+09 5.9250e+02
13.30818 648.55 873.02 0. 0.05893 0. 0.
6.6998e+00 7.2297e+09 1.0221e+10 2.3235e+09 6.8863e+09 4.5027e+02
13.30818 456.76 641.49 0. 0.06494 0. 0.
7.6998e+00 6.3095e+09 9.1447e+09 1.9079e+09 6.0480e+09 4.2405e+02
13.30818 400.53 593.73 0. 0.07718 0. 0.
8.6998e+00 5.5284e+09 8.0632e+09 1.5704e+09 5.2795e+09 4.0064e+02
13.30818 351.61 547.18 0. 0.08394 0. 0.
9.7010e+00 4.9801e+09 6.8844e+09 1.1583e+09 4.4607e+09 3.8206e+02
13.30818 316.12 490.84 0. 0.10174 0. 0.
1.0700e+01 4.9368e+09 7.0092e+09 1.0021e+09 4.3293e+09 3.9965e+02
13.30818 303.60 503.86 0. 0.10758 0. 0.
1.1700e+01 4.6917e+09 7.1677e+09 8.5590e+08 4.4610e+09 4.2632e+02
13.30818 289.24 544.70 0. 0.15829 0. 0.
1.2700e+01 3.9495e+09 7.2717e+09 6.7227e+08 4.6253e+09 4.1682e+02
13.30818 246.57 569.90 0. 0.22235 0. 0.
1.3700e+01 3.3865e+09 7.0817e+09 5.4749e+08 5.0243e+09 4.0619e+02
13.18151 215.91 601.28 0. 0.30756 0. 0.
1.4701e+01 2.9337e+09 6.2445e+09 4.4884e+08 4.3749e+09 3.8142e+02
12.84784 187.11 546.56 0. 0.30386 0. 0.
1.5700e+01 2.5690e+09 5.0490e+09 3.3592e+08 3.4799e+09 3.5282e+02
12.19218 160.84 468.71 0. 0.26519 0. 0.
1.6700e+01 2.3887e+09 4.9485e+09 3.1135e+08 3.2615e+09 3.4948e+02
11.56072 148.56 453.76 0. 0.25941 0. 0.

```

1.7700e+01	2.2720e+09	4.8080e+09	2.9194e+08	3.0296e+09	3.4654e+02
11.07246	140.30	436.22	0.	0.25007	0. 0.
1.9701e+01	2.0501e+09	4.5014e+09	2.6100e+08	2.5650e+09	3.3933e+02
10.79246	124.61	398.18	0.	0.23155	0. 0.
2.1700e+01	1.8283e+09	4.2441e+09	2.2882e+08	2.1678e+09	3.3000e+02
10.23218	109.42	362.08	0.	0.20382	0. 0.
2.3700e+01	1.5887e+09	3.9953e+09	2.0075e+08	1.8811e+09	3.2199e+02
9.67221	94.36	335.01	0.	0.19934	0. 0.
2.5700e+01	1.3619e+09	3.7508e+09	1.7438e+08	1.6197e+09	3.1382e+02
9.10971	80.24	308.57	0.	0.19323	0. 0.
2.7700e+01	1.1024e+09	3.4471e+09	1.4447e+08	1.2478e+09	2.9473e+02
8.53403	62.67	263.87	0.	0.14994	0. 0.
2.9701e+01	8.7580e+08	3.1391e+09	1.1998e+08	1.0212e+09	2.8712e+02
7.93217	49.42	237.06	0.	0.15421	0. 0.
3.1700e+01	6.8130e+08	2.7342e+09	8.1192e+07	7.5893e+08	2.6334e+02
7.32134	37.34	196.41	0.	0.13252	0. 0.
3.3700e+01	5.3472e+08	2.5549e+09	6.9091e+07	6.5899e+08	2.5321e+02
6.71112	29.14	180.34	0.	0.13313	0. 0.
3.5700e+01	4.0890e+08	2.3340e+09	5.7454e+07	5.5600e+08	2.4167e+02
6.12152	22.16	162.43	0.	0.14035	0. 0.
3.7700e+01	3.1454e+08	1.8287e+09	4.5915e+07	4.1878e+08	2.2064e+02
5.54647	17.33	134.83	0.	0.13950	0. 0.
3.9701e+01	2.3863e+08	1.5841e+09	3.5977e+07	3.4208e+08	2.0029e+02
4.97147	13.30	116.30	0.	0.15134	0. 0.
4.1700e+01	1.7588e+08	1.3234e+09	2.7441e+07	2.7031e+08	1.7940e+02
4.40118	9.96	97.98	0.	0.17418	0. 0.
4.3700e+01	1.2601e+08	1.1837e+09	2.0903e+07	2.9801e+08	1.6509e+02
3.83417	7.30	98.93	0.	0.24922	0. 0.
4.5700e+01	1.0726e+08	1.0202e+09	1.8543e+07	2.3954e+08	1.5441e+02
3.33243	6.22	85.78	0.	0.26022	0. 0.
4.7700e+01	9.0884e+07	7.9781e+08	1.6276e+07	1.7713e+08	1.3894e+02
2.88971	5.19	69.96	0.	0.22554	0. 0.
4.9701e+01	7.6310e+07	7.0961e+08	1.4535e+07	1.4630e+08	1.2956e+02
2.50304	4.36	61.41	0.	0.22795	0. 0.
5.1700e+01	6.1049e+07	5.1819e+08	9.0729e+06	9.6794e+07	1.0726e+02
2.11618	3.36	45.44	0.	0.20600	0. 0.
5.3700e+01	4.9482e+07	4.5487e+08	8.0573e+06	7.9643e+07	9.8776e+01
1.72958	2.75	39.57	0.	0.21662	0. 0.
5.5700e+01	3.9359e+07	3.9512e+08	7.0783e+06	6.4663e+07	9.0248e+01
1.34158	2.21	34.09	0.	0.22784	0. 0.
5.6700e+01	3.4672e+07	3.5372e+08	6.0927e+06	5.4862e+07	8.3001e+01
0.95358	1.93	30.12	0.	0.23124	0. 0.
5.7700e+01	3.0414e+07	3.0473e+08	5.7539e+06	2.8044e+07	7.2906e+01
0.76037	1.69	20.15	0.	0.14826	0. 0.
5.8700e+01	2.6522e+07	2.8142e+08	5.3306e+06	2.5113e+07	6.8772e+01
0.57435	1.49	18.53	0.	0.15346	0. 0.
5.9200e+01	2.3837e+07	2.6171e+08	4.9352e+06	2.2218e+07	6.6264e+01
0.40435	1.34	17.11	0.	0.15382	0. 0.
5.9701e+01	1.9632e+07	1.5881e+08	4.2381e+06	1.1334e+07	5.9340e+01
0.31935	1.10	11.55	0.	0.09470	0. 0.
6.0200e+01	1.6002e+07	1.3788e+08	3.6589e+06	8.6067e+06	5.5914e+01
0.25317	0.89	9.77	0.	0.09018	0. 0.
6.0700e+01	1.2825e+07	1.1879e+08	3.1269e+06	6.4434e+06	5.2484e+01
0.21572	0.71	8.19	0.	0.08561	0. 0.
6.1200e+01	1.0083e+07	1.0163e+08	2.6432e+06	4.7679e+06	4.9114e+01
0.17820	0.56	6.82	0.	0.08035	0. 0.

Appendix A. 3DFloat Input File

```

6.1700e+01 7.5459e+06 8.5070e+07 2.1719e+06 3.3999e+06 4.5818e+01
0.14033 0.42 5.57 0. 0.07096 0. 0.
6.2200e+01 4.6046e+06 6.4256e+07 1.5810e+06 1.9367e+06 4.1669e+01
0.10107 0.25 4.01 0. 0.05424 0. 0.
6.2700e+01 2.4509e+05 6.6083e+06 2.5369e+05 3.8278e+05 1.1453e+01
0.06181 0.04 0.94 0. 0.05387 0. 0.
6.3001e+01 1.7458e+05 5.0128e+06 1.8655e+05 2.2568e+05 1.0319e+01
0.02295 0.02 0.68 0. 0.05181 0. 0.

```

```

aero_blade_table blname nrel5mw ! r/R c/R twist [deg]
airfoil
0.02 0.05622222222222 13.308 Cylinder1
0.0455031746032 0.05622222222222 13.308 Cylinder1
0.088888888888889 0.0611746031746 13.308 Cylinder1
0.132274603175 0.0661428571429 13.308 Cylinder2
0.186507936508 0.07233333333333 13.308 DU40_A17
0.251587301587 0.0738412698413 11.48 DU35_A17
0.3166666666667 0.0707619047619 10.162 DU35_A17
0.381746031746 0.06744444444444 9.011 DU30_A17
0.446825396825 0.0636031746032 7.795 DU25_A17
0.511904761905 0.0594920634921 6.544 DU25_A17
0.576984126984 0.0555873015873 5.361 DU21_A17
0.642063492063 0.0516825396825 4.188 DU21_A17
0.707142857143 0.04777777777778 3.125 NACA64_A17
0.7722222222222 0.043873015873 2.319 NACA64_A17
0.837301587302 0.0399682539683 1.526 NACA64_A17
0.891534920635 0.0367142857143 0.863 NACA64_A17
0.934920634921 0.03311111111111 0.37 NACA64_A17
0.978306349206 0.0225238095238 0.106 NACA64_A17
1.001 0.00001 0.106 NACA64_A17 ! dbg
used to be as at .978

```

```

read_airfoil
file ../../airfoils/Cylinder1.dat afname Cylinder1 thick 1.000
read_airfoil
file ../../airfoils/Cylinder2.dat afname Cylinder2 thick .736
read_airfoil
file ../../airfoils/DU40_A17.dat afname DU40_A17 thick .400
read_airfoil
file ../../airfoils/DU35_A17.dat afname DU35_A17 thick .350
read_airfoil
file ../../airfoils/DU30_A17.dat afname DU30_A17 thick .300
read_airfoil
file ../../airfoils/DU25_A17.dat afname DU25_A17 thick .250
read_airfoil
file ../../airfoils/DU21_A17.dat afname DU21_A17 thick .210
read_airfoil
file ../../airfoils/NACA64_A17.dat afname NACA64_A17 thick .18

```

```
! BLADE GEOMETRY
```

```
! -----
```

```
! blade 1
```

```
! blade 1 root - body coordinate system that does not pitch
```

```

new_body name blade_1_root parent hub reftype refnode xfind -1.912
0. 0.
rotorder 321 rotation 0. -2.5 0. axes normal

! blade_1_pitching - this body has coordinate system that pitches
new_body name blade_1_pitching parent blade_1_root reftype refnode
xfind 0. 0. 0. rotorder 321 rotation 0. 0. 0. axes normal ! pitch (z
axis) !-90 for idle cases

! from blade root to hub CG
new_elements_beam1 nelelem 3 material massless2 connect_mode
connect_2
x1 0. 0. 1.5 dcyll1 2.0 tcyll1 1. pointmass 17206.961
x2 0. 0. 0.0 dcyll2 2.0 tcyll2 1. btype beam

! from blade tip to root
new_elements_beam1 nelelem 17 material massless1 connect_mode
connect_2
x1 0. 0. 63.0 dcyll1 1. tcyll1 .45
x2 0. 0. 1.5 dcyll2 3. tcyll2 .45 btype beam
blname nrel5mw scale_mass 1.057486996 frac_stiff 1.

! blade 2

! blade_2_root - body coordinate system that does not pitch
new_body name blade_2_root parent hub reftype refnode xfind -1.912
0. 0.
rotorder 321 rotation 120. -2.5 0. axes normal

! blade_2_pitching - this body has coordinate system that pitches
new_body name blade_2_pitching parent blade_2_root reftype refnode
xfind 0. 0. 0. rotorder 321 rotation 0. 0. 0. axes normal ! pitch (z
axis) !-90 for idle cases

! from blade root to hub CG
new_elements_beam1 nelelem 3 material massless2 connect_mode
connect_2
x1 0. 0. 1.5 dcyll1 2.0 tcyll1 1. pointmass 17206.961
x2 0. 0. 0.0 dcyll2 2.0 tcyll2 1. btype beam

! from blade tip to root
new_elements_beam1 nelelem 17 material massless1 connect_mode
connect_2
x1 0. 0. 63.0 dcyll1 1. tcyll1 .45
x2 0. 0. 1.5 dcyll2 3. tcyll2 .45 btype beam
blname nrel5mw scale_mass 1.057486996 frac_stiff 1.

!copy_elements
!from_body: blade_1_pitching
!to_body: blade_2_pitching

```



```

!print_b1_elements
e34.txt
34 34
1 12
1 12

!print_b1_elements
e54.txt
54 54
1 12
1 12

! blade 3

! blade_3_root - body coordinate system that does not pitch
new_body name blade_3_root parent hub reftype refnode xfind -1.912
0. 0.
rotorder 321 rotation -120. -2.5 0. axes normal

! blade_3_pitching - this body has coordinate system that pitches
new_body name blade_3_pitching parent blade_3_root reftype refnode
xfind 0. 0. 0. rotorder 321 rotation 0. 0. 0. axes normal ! pitch (z
axis) !-90 for idle cases

! from blade root to hub CG
new_elements_beam1 nelem 3 material massless2 connect_mode
connect_2
x1 0. 0. 1.5 dcyll1 2.0 tcyl1 1. pointmass 17206.961
x2 0. 0. 0.0 dcyll2 2.0 tcyl2 1. btype beam

! from blade tip to root
new_elements_beam1 nelem 17 material massless1 connect_mode
connect_2
x1 0. 0. 63.0 dcyll1 1. tcyl1 .45
x2 0. 0. 1.5 dcyll2 3. tcyl2 .45 btype beam
blname nrel5mw scale_mass 1.057486996 frac_stiff 1.

!copy_elements
!from_body: blade_1_pitching
!to_body: blade_3_pitching

! -----
! ROTOR WAKE MODEL AND PITCH CONTROL NODES
! -----

rotor_wake
name: rotor_1
shaft_element_body: mainbearing
shaft_element_position: -1.4 0. 0. ! expressed in body
mainbearing system
rotating_node: 1
induction: all
logfile: rotor_1.txt
nblades: 3
bladenames: blade_1_pitching
blade_2_pitching

```

```

blade_3_pitching
pitch_control_name:      5mw_fixed
pitch_actuator_bodies:  blade_1_pitching
                        blade_2_pitching
                        blade_3_pitching
pitch_actuator_positons: 0. 0. 0.75
                        0. 0. 0.75
                        0. 0. 0.75

! -----
! CONTROL SYSTEM PART 1: Define the generator specification
! -----
generator name: nrel5mwfloating  gen_eta: 1.
scale_omega: 1.26710903694  scale_mgen: 4180074.35
omega:          mgen:          ! [rad/s]  [Nm]
0.570826146749  0.0           ! constant torque above and
below this
0.742097666716  0.450259926989
0.824734617833  0.556121407034
0.90737156895   0.673149455494
0.990008520067  0.801344072373
1.0             1.0
omega_eta:      eta:
0.15  0.85
0.97  0.944

! -----
! CONTROL SYSTEM PART 2: Define the pitch control specification
! -----
pitchcontrol
control_type:  iea_oc3_fixed
name:         5mw_fixed
scale_omega:  1.
scale_vaxial: 1.
scale_pitchcoll: -1.0
omeganom:     1.2671
ti:           10.
gain:         1.
pitchref:     0.
aux: 1. 2. 3. 4. 5. 6. 7. 8. 9. 10.

! -----
! DEFINE NGI MACRO ELEMENT
! -----

springs          ! Define a set of springs
  name: idealized_clay  ! Name of this set of springs.
  type: ngi_dll         ! Algorithm
  inputfiles:         ! list of input files, terminated by
blank line
  ..\..\tools\Props_Abaqus.txt           ! First input file
  ..\..\tools\MomentDisplacement_Abaqus.txt ! Second input file
  C:\3Dfloat\tools\REDWINmodel2E.dll     ! Third input file, must
be in this order

! -----

```

```

!      APPLY NGI MACRO ELEMENT
! -----

add_node_stiffness
  find:  0.    0.   -20.0
  f_lin: 0. 0. 0.    0. 0. 0.
  x_lin: 0. 0. -20.0 0. 0. 0.
  springs_name:  idealized_clay
  idof_springs: 5
  logfile:  ngi_all dof.txt

! -----
!      APPLY BOUNDARY CONDITIONS
! -----

! Apply gravity to point masses for nacelle/hub system
!
apply_nodal_bc find -7.9377E-01 0.0000E+00 8.9632E+01 apply_force 0.
0. -1176780.0 0. 0. 0. ! nacelle 120 t
apply_nodal_bc find  4.5938E+00 0.0000E+00 8.9161E+01 apply_force 0.
0. -1176780.0 0. 0. 0. ! nacelle 120 t
apply_nodal_bc find -5.0000E+00 0.0000E+00 90.0      apply_force 0.
0. -556821.59 0. 0. 0. ! hub (on shaft and at eccentricities)

! Drop tower 0.2 m at top
! apply_nodal_bc find 0.0 0.0 87.6 apply_displ idofs 1 idofe 1 displ
0.2 tend 10.0 ! For free vibration

-----
P-Y CURVES
-----

! Only 1 springs is included for illustration purposes. When
applying p - y curves, 24 springs (similar to the one included here)
was applied in total, with 1m spacing. (Z = -20.5:-1:-43.5).

!springs
  maxsprings 24
  name: spring_no_1
  type: linear_py
  stiffness_maxforce:
0.000000 0.000000
0.000000 0.000000
0.000000 0.000000
0.000000 0.000000
0.000000 0.000000
0.000000 0.000000
0.000000 0.000000
0.000000 0.000000
0.000000 0.000000
0.000000 0.000000
0.000000 0.000000
168000.000000 201600.000000
874500.000000 393525.000000
1176887.755105 176533.163266
2387755.102029 107448.979591
16392857.142867 245892.857143

!add_node_stiffness

```

```

find: 0. 0. -20.5
f_lin: 0. 0. 0. 0. 0. 0.
x_lin: 0. 0. -20.5 0. 0. 0.
springs_name: spring_no_1
idof_springs: 1
logfile: py_spring_no_1_x.txt

!add_node_stiffness
find: 0. 0. -20.5
f_lin: 0. 0. 0. 0. 0. 0.
x_lin: 0. 0. -20.5 0. 0. 0.
springs_name: spring_no_1
idof_springs: 2
logfile: py_spring_no_1_y.txt

! ... etc

! -----
! CLAMP TOWER BOTTOM NODE FOR DOF 3&6
! -----
! Used when applying p - y curves

!apply_nodal_bc find 0. 0. -44. apply_displ idofs 3 idofe 3 displ 0.
displacement along vertical axis (z-axis)
!apply_nodal_bc find 0. 0. -44. apply_displ idofs 6 idofe 6 displ 0.
rotation around vertical axis (z-axis, torsion)

! -----
! TOWER SHADOWING
! -----

tower_shadow type: potential
xfind: 0. 0. 10. d cyl: 6. cdn: 1.0 ! node in tower,
diameter, drag
xfind: 0. 0. 87.6 d cyl: 3.87 cdn: 1.0 ! if linear all the
way, two nodes are enough

! -----
! APPLY MONITORS TO SENSOR SELECTED OUTPUT
! -----

! sensor 18 to 23 platform displacements swl
!
monitor_element_b1 type orientation file turb1_swl.txt nmonitor 1
find 0.0 0.0 0.5 node 1 body_name inertial
label PtfmSurge PtfmSway PtfmHeave Ptfm_xx Ptfm_xy Ptfm_xz Ptfm_yx

! sensor 48 to 50 blade 1 tip deflection
!
monitor_element_b1 type forces file UC1DU1_forces.txt nmonitor 1
find -7.21687836487 12.5 10.0 node 2 body_name inertial
label UC1DU1Fx UC1DU1Fy UC1DU1Fz s4 s5 s6

! sensor 39 to 41 tower base forces

```

```

!
monitor_element_b1 type forces file TwrBs_forces_z.txt nmonitor 1
find 0.0 0.0 2.5 node 1 body_name tower
label s1 s2 s3 TwrBsFxt TwrBsFyt TwrBsFzt to 100 !'to' set by saa

! sensor 42 to 44 tower base moments
!
monitor_element_b1 type moments file TwrBs_moments.txt nmonitor 1
find 0.0 0.0 2.5 node 1 body_name tower
label s1 s2 s3 TwrBsMxt TwrBsMyt TwrBsMzt to 100 !'to' set by saa

! sensor 15 to 17 blade 1 tip deflection
!
monitor_element_b1 type orientation file tower_topx.txt nmonitor 1
find 0.0000E+00 0.0000E+00 8.6900E+01 node 2 body_name tower
label TTDspFA TTDspSS s3 s4 s5 s6 TTDsp_yx

! sensor 5 Wave elevation
!
monitor_element_b1 find 0. 0. 18. nmonitor 1 node 1 type
waveheight_origin
file waves_origin.txt label WaveElev

! sensor 11 to 12 blade 1 tip deflection
!
monitor_element_b1 find 0. 0. 63. nmonitor 1 node 1 type
orientation
file blade_1_tipx.txt body_name blade_1_root label OoPDefl1 IPDefl1

! Elastic twist of blade tip
!
monitor_element_b1 find 0. 0. 63. nmonitor 1 node 1 type
orientation
file blade_1_tiptwist.txt body_name blade_1_pitching label s1 s2 s3
s4 s5 s6 Twst_yx

! Actual pitch angle measured at blade root
!
monitor_element_b1 find 0. 0. 1.5 nmonitor 1 node 1 type
orientation
file blade_1_pitch.txt body_name blade_1_root label s1 s2 s3 s4 s5
s6 Pitch_yx

! sensor 24 to 26 blade 1 forces at 0% span (1.5 m)
!

monitor_element_b1 find 0. 0. 1.25 nmonitor 1 node 1 type forces
! dbg
file blade_1_root_force_hub_n1.txt body_name blade_1_root label s1
s2 s3 RootFxc1 RootFyc1 RootFzc1

monitor_element_b1 find 0. 0. 1.25 nmonitor 1 node 1 type moments
! dbg
file blade_1_root_moment_hub_n1.txt body_name blade_1_root label s1
s2 s3 RootMxc1 RootMyc1 RootMzc1

```

```

! sensor 27 to 29 blade 1 moments at 0% span (1.5 m)
!
monitor_element_b1 find 0. 0. 3.305 nmonitor 1 node 2 type
moments ! dbg
file blade_1_root_moment.txt body_name blade_1_root label blade_mx
blade_my blade_mz ! elem system

! sensor 30 to 32 low speed shaft moments TAN May 20, 2013
!
monitor_element_b1 find 1.162 0. 0. nmonitor 1 node 2 type
moments ! dbg
file lsshft_torque.txt body_name hub label s1 s2 s3 RotTorq

monitor_element_b1 find 1.662 0. 0. nmonitor 1 node 2 type
moments ! dbg
file lsshft_bend.txt body_name hub label s1 s2 s3 s4 LSSGagMya
LSSGagMza

! sensor 33 to 35 tower top forces
!
!TAN 20/5-2013 Express in system following tower top

!monitor_element_b1 find 0. 0. 0. nmonitor 1 node 1 type forces
file tower_top_force.txt body_name yawdrive label s1 s2 s3 YawBrFxp
YawBrFyp YawBrFzp

! sensor 36 to 38 tower top forces
!
!TAN 20/5-2013 Express in system following tower top

!monitor_element_b1 find 0. 0. 0. nmonitor 1 node 1 type moments
file tower_top_moment.txt body_name yawdrive label s1 s2 s3
YawBrMxp YawBrMyp YawBrMzp

monitor_element_b1 type wind_fixed find 0. 0. 90. nmonitor 1
node 2
file wind.txt body_name inertial label WindVxi WindVyi WindVzi

! Mudline forces and moments
!
monitor_element_b1 type forces file mudline_forces.txt nmonitor 1
find 0.0 0.0 -20. node 1 body_name inertial
label s1 s2 s3 fx_mud fy_mud fz_mud

monitor_element_b1 type moments file mudline_moments.txt nmonitor 1
find 0.0 0.0 -20. node 1 body_name inertial
label s1 s2 s3 mx_mud my_mud mz_mud

!
monitor_element_b1 type orientation file turb1_mud.txt nmonitor 1
find 0.0 0.0 -20. node 1 body_name inertial
label surge_mud sway_mud heave_mud mud_xx mud_xy mud_xz mud_yx

monitor_element_b1 find 0. 0. -20. nmonitor 1 node 1 type
gather
file IFE_3DFloat_sensors.txt label oc4_gather toffset 1.

```

Appendix A. 3DFloat Input File

```

sensors:
nfact: 1 source: WindVxi          scale: 1.          unit: [m/s] !
header as source label
nfact: 1 source: WindVyi          scale: 1.          unit: [m/s] !
nfact: 1 source: WindVzi          scale: 1.          unit: [m/s] !
nfact: 1 source: WaveElev         scale: 1.          unit: [m] !
nfact: 1 source: GenPwr_1         scale: .000944     unit: [kW]
header: GenPwr
nfact: 1 source: GenTq_1          scale: 1.030927835e-5 unit:
[kNm] ! 1./97.e3 header: GenTq
nfact: 1 source: Azimuth_1        scale: 57.295779513082323 unit:
[deg] header: Azimuth ! 180./rpi
nfact: 1 source: RotSpeed_1       scale: 9.549296585513721 unit:
[rpm] header: RotSpeed ! 30./pi
nfact: 1 source: RotSpeed_1       scale: 926.2817687948309 unit:
[rpm] header: GenSpeed ! 30.*97./rpi
nfact: 1 source: PtfmSurge        scale: 1.          unit: [m] !
nfact: 1 source: PtfmSway         scale: 1.          unit: [m] !
nfact: 1 source: PtfmHeave        scale: 1.          unit: [m] !
nfact: 1 source: OoPDefl1         scale: 1.          unit: [m] !
nfact: 1 source: IPDefl1          scale: 1.          unit: [m] !
nfact: 1 source: Twst_yx          scale: -57.295779513082323 unit:
[deg] header: TwstDefl1
nfact: 1 source: BldPitch1_1      scale: -57.295779513082323
unit: [deg] header: BldPitch1 !
nfact: 1 source: TTDspFA          scale: 1.          unit: [m] !
nfact: 1 source: TTDspSS          scale: 1.          unit: [m] !
nfact: 1 source: TTDsp_yx         scale: 57.295779513082323 unit:
[deg] header: TTDspTwst
nfact: 1 source: RootFxc1         scale: .001        unit: [kN]
nfact: 1 source: RootFyc1         scale: .001        unit: [kN]
nfact: 1 source: RootFzc1         scale: -.001       unit: [kN]
nfact: 1 source: RootMxc1         scale: -.001       unit: [kNm]
nfact: 1 source: RootMyc1         scale: -.001       unit: [kNm]
nfact: 1 source: RootMzc1         scale: -.001       unit: [kNm] !
nfact: 1 source: RotTorq          scale: -.001       unit: [kNm] !
nfact: 1 source: blade_mx         scale: -.001       unit: [kNm] !
nfact: 1 source: blade_my         scale: -.001       unit: [kNm] !
nfact: 1 source: blade_mz         scale: -.001       unit: [kNm] !
nfact: 1 source: LSSGagMya        scale: .001        unit: [kNm] !
nfact: 1 source: LSSGagMza        scale: .001        unit: [kNm] !
nfact: 1 source: YawBrFxp         scale: -.001       unit: [kN] !
Nacelle coord.syst.
nfact: 1 source: YawBrFyp         scale: -.001       unit: [kN] !
nfact: 1 source: YawBrFzp         scale: .001        unit: [kN] !
nfact: 1 source: YawBrMxp         scale: .001        unit: [kNm] !
nfact: 1 source: YawBrMyp         scale: .001        unit: [kNm] !
nfact: 1 source: YawBrMzp         scale: .001        unit: [kNm] !
nfact: 1 source: TwrBsFxt         scale: -.001       unit: [kN] !
Tower base coord.sys.
nfact: 1 source: TwrBsFyt         scale: -.001       unit: [kN] !
nfact: 1 source: TwrBsFzt         scale: .001        unit: [kN] !
nfact: 1 source: TwrBsMxt         scale: .001        unit: [kNm] !
nfact: 1 source: TwrBsMyt         scale: .001        unit: [kNm] !
nfact: 1 source: TwrBsMzt         scale: .001        unit: [kNm] !
nfact: 1 source: fx_mud           scale: -.001       unit: [kN] !

```

```

nfact: 1 source: fy_mud      scale:  -.001      unit: [kN]  !
nfact: 1 source: fz_mud      scale:   .001      unit: [kN]  !
nfact: 1 source: mx_mud      scale:   .001      unit: [kNm] !
nfact: 1 source: my_mud      scale:   .001      unit: [kNm] !
nfact: 1 source: mz_mud      scale:   .001      unit: [kNm] !

```

```

! -----
! SET UP WIND INCLUDING TURBULENCE
! -----

```

```

! Wind settings
!
wind_transient
0.      0.01  0.
100.    12.0  0.

turbulence_box  turbulence  file  turbulence_info
c:\3Dfloat\turbulence\LC6.bts !Turbsim file
turb_tstart: 100.  turb_intens: 0.146  reference_node:  0. 0. 0.
reference_height  90.
turbulence_scaling target_turbulence_intensity

```

```

! -----
! RUN DESIRED SOLUTION SETTINGS
! -----

```

```

! Take one step to assemble all matrices
! -----

```

```

monitor_element_b1  type plot nmonitor 100
file turb1.plot

```

```

monitor_element_b1  type tecplot nmonitor 100
file turb1.dat

```

```

! set solver settings
newmark dt: 0.01  nassemble: 1  nnewton: 50  nsubmin: 3  rwilson: 0.9
relax: 0.0  resid_newton: 1e-15  nmonitor: 10

```

```

damping type ratio2rayl  ratio_1 0.00  ratio_2 0.01  omega_1  0.0
omega_2  1.6956  !1.5135 for p - y model
step nstep 72500  method step9

```

```

!end

```

```

!time 730s

```

```

END

```


Appendix B

TurbSim Input File

TurbSim Input File. Valid for TurbSim v1.06.00, 21-Sep-2012; for Certification Test #1 (Kaimal Spectrum, formatted FF files).

```
-----Runtime Options-----
13428          RandSeed1
RanLux        RandSeed2
False        WrBHHTP
False        WrFHHTP
False        WrADHH
True         WrADFF
False        WrBLFF
True         WrADTWR
False        WrFMTFF
False        WrACT
True         Clockwise
0            ScaleIEC

-----Turbine/Model Specifications-----
31            NumGrid_Z
31            NumGrid_Y
0.01         TimeStep
630.0        AnalysisTime
630.0        UsableTime
90.00        HubHt
145.00       GridHeight
145.00       GridWidth
0            VFlowAng
0            HFlowAng

-----Meteorological Boundary Conditions-----
"IECKAI"     TurbModel
"1-ED3"      IECstandard
14.6         IECturbc
"NTM"        IEC_WindType
default      ETMc
"PL"         WindProfileType
```

```
90.00          RefHt
12.00          URef
default       ZJetMax
default       PLExp
default       Z0

-----Non-IEC Meteorological Boundary Conditions-----
default       Latitude
0.05          RICH_NO
default       UStar
default       ZI
default       PC_UW
default       PC_UV
default       PC_VW
default       IncDec1
default       IncDec2
default       IncDec3
default       CohExp
-----Coherent Turbulence Scaling Parameters-----
".\EventData" CTEventPath
"Random"      CTEventFile
true          Randomize
  1.0         DistScl
  0.5         CTLy
  0.5         CTLz
10.0         CTStartTime
```

```
=====
NOTE: Do not add or remove any lines in this file!
=====
```

Appendix C

MATLAB Script for Calculating Fatigue Damage

```
%This script calculates the fatigue damage at the mudline

clc; clear all; close all

%% 1. Input values
% 1.1. General
t = 0.06; %Pile wall thickness [m]
DFE = 3; %From DNV OS-J101

% 1.2. Input values for S-N curve F3 in seawater with cathodic
protection (DNV2016)
k = 0.25; %Thickness exponent
t_ref = 0.025; %Reference thickness [m]
SCF = 1.61; %Stress concentration factor

% 1.2.1. Cycles, N, =< 10^6
m1 = 3; %Negative slope of S-N curve on logN-logS plot
loga1 = 11.146; %Intercept of logN axis

% 1.2.2. Cycles, N, > 10^6
m2 = 5; %Negative slope of S-N curve on logN-logS plot
loga2 = 14.576; %Intercept of logN axis

%% 2. Find mudline moments
% 2.1. Read files
FileID = fopen(fullfile('FileLocation','FileName.txt'),'r');

% 2.2. Find mudline moments
text = textscan(FileID,'%s');
start = find(strcmp({'and'},text{1})) + 2;
stop = length(text{end});
col = 11;
row = (stop - start)/col;
```

```

for i = 1:row
    ti(i) = str2num(cell2mat(text{1}(start + 2 + col*(i-1))));
    My(i) = str2num(cell2mat(text{1}(start + 10 + col*(i-1))));
end

%% 3. Create vector of useful values (ignoring first 130s of
simulation)
% 3.1. Find where time series after 130sec
n = 1; %Step counter
for i = 1:length(ti)
    if ti(i) == 130
        break
    else
        n = n + 1; %Update step counter
    end
end

% 3.2. Create vector with usefull time steps
time = ti(n+1:end); %Useful time vector, [s]

% 3.3. Create vectors with usefull moment history
M = My(1,n+1:end); %Useful moment history [Nm]

%% 4. Generate stresses for useful time history
% 4.1. Input
r_o = 3.0; %Outer radius, [m]
r_i = r_o-t; %Inner radius, [m]
r_m = r_o-t/2; %Mean radius, [m]
I = pi/4*(r_o^4-r_i^4); %Moment of inertia, [m^4]

% 4.2. Create vectors with stress time histories
sigmaY = SCF*((r_m*10^(-6))/I).*My; %Stress time series

%% 5. Perform Rainflow counting
% 5.1. Finding turning points
tp = sig2ext(sigmaY);

% 5.2. Rainflow analysis
rf = rainflow(tp);

% 5.3. Select values
% 5.3.1 Count of stress ranges
count = rf(3,:);

% 5.3.2 Amplitude of stress ranges
dS = rf(1,:);

%% 6. S-N analysis
% 6.1. Find maximum number of cycles per stress range
logN1 = loga1-m1*log10(dS*(t/t_ref)^k);
logN2 = loga2-m2*log10(dS*(t/t_ref)^k);
logN = logN1;

```

```

for i = 1:length(dS)
    if logN(i) > 6
        logN(i) = logN2(i);
    end
end

N = 10.^(logN); %Maximum number of cycles per stress range

%% 7. Fatigue damage and lifetime calculation
% 7.1. Fatigue damage over time series (Miner sum)
D = sum(count./N);

% 7.2. Fatigue damage over 1 year
D_y = (365*24*60*60/600)*D;

% 7.3. Fatigue lifetime
L = 1/D_y;

% 7.4. Design fatigue lifetime (include DFF)
D_L = 1/(DFF*D_y);
D_D = DFF*D_y;

%% 8. Print results
disp(['Design fatigue life: ' num2str(D_L) ' years']);

```


Appendix D

S - N Data for Steel with Cathodic Protection in Seawater

S-N curve	$N \leq 10^6$ cycles		$N > 10^6$ cycles $\log \bar{a}_2$ $m_2 = 5.0$	Fatigue limit at 10^7 cycles (MPa) *)	Thickness exponent k	Structural stress concentration embedded in the detail (S-N class), see also equation (2.3.2)
	m_1	$\log \bar{a}_1$				
B1	4.0	14.917	17.146	106.97	0	
B2	4.0	14.685	16.856	93.59	0	
C	3.0	12.192	16.320	73.10	0.05	
C1	3.0	12.049	16.081	65.50	0.10	
C2	3.0	11.901	15.835	58.48	0.15	
D	3.0	11.764	15.606	52.63	0.20	1.00
E	3.0	11.610	15.350	46.78	0.20	1.13
F	3.0	11.455	15.091	41.52	0.25	1.27
F1	3.0	11.299	14.832	36.84	0.25	1.43
F3	3.0	11.146	14.576	32.75	0.25	1.61
G	3.0	10.998	14.330	29.24	0.25	1.80
W1	3.0	10.861	14.101	26.32	0.25	2.00
W2	3.0	10.707	13.845	23.39	0.25	2.25
W3	3.0	10.570	13.617	21.05	0.25	2.50















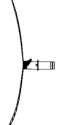



*) see also [2.11]

Figure D.1: S - N data for steel with cathodic protection in seawater (DNVGL 2016).

Appendix E

Natural Frequencies for the Blade Modes of the OWT in the North Sea

Table E.1: Comparison between the measured and the simulated natural frequencies for the first blade modes

	Measured freq. (Hz)	Simulated freq. (Hz)			Simulated modes		
		API p-y curves	FEA p-y curves	Macro- element model	Front view	Side view	Top view
1 st Blade AFP	0.4833	0.524	0.528	0.528			
1 st Blade AFY	0.507	0.544	0.545	0.544			
1 st Blade DT	0.760	0.556	0.562	0.561			
1 st Blade CF	0.803	0.775	0.775	0.774			
1 st Blade AEP	0.910	0.845	0.858	0.858			
1 st Blade AEY	0.957	0.947	0.954	0.954			

AFP = asymmetric flapwise pitch

AFY = asymmetric flapwise yaw

DT = drivetrain torsion

CT = collective flap

AEP = asymmetric edgewise pitch

AEY = asymmetric edgewise yaw
